FACULTÉ DES ÉTUDES SUPÉRIEURES
ET POSTOCTORALES

uOttawa

L'Université canadienne
Canada's university

FACULTY OF GRADUATE AND
POSDOCTORAL STUDIES

Cyril Hnatovsky
AUTEUR DE LA THÈSE / AUTHOR OF THESIS

Ph.D. (Physics)
GRADE / DEGREE

Department of Physics
FACULTÉ, ÉCOLE, DÉPARTEMENT / FACULTY, SCHOOL, DEPARTMENT

Ultra-high spatial resolution diagnostics of femtosecond laser radiation-induced modification morphology in glasses for the fabrication of microfluidic and microphotonic components

TITRE DE LA THÈSE / TITLE OF THESIS

Thomas Brabec
DIRECTEUR (DIRECTRICE) DE LA THÈSE / THESIS SUPERVISOR

Rod Taylor
CO-DIRECTEUR (CO-DIRECTRICE) DE LA THÈSE / THESIS CO-SUPERVISOR

EXAMINATEURS (EXAMINATRICES) DE LA THÈSE / THESIS EXAMINERS

David Asner	Robert Fedosejevs
Stephen Mihailov	Sylvain Raymond

Gary W. Slater
LE DOYEN DE LA FACULTÉ DES ÉTUDES SUPÉRIEURES ET POSTDOCTORALES /
DEAN OF THE FACULTY OF GRADUATE AND POSTDOCORAL STUDIES

Ultra-high spatial resolution diagnostics of femtosecond laser radiation-induced modification morphology in glasses for the fabrication of microfluidic and microphotonic components

by

Cyril Hnatovsky

A thesis presented to the University of Ottawa
in fulfillment of the thesis requirements for the degree of
Doctor of Philosophy in Physics

Ottawa, Ontario
January 16, 2006

Library and
Archives Canada

Published Heritage
Branch

395 Wellington Street
Ottawa ON K1A 0N4
Canada

Bibliothèque et
Archives Canada

Direction du
Patrimoine de l'édition

395, rue Wellington
Ottawa ON K1A 0N4
Canada

Your file Votre référence
ISBN: 978-0-494-15025-2
Our file Notre référence
ISBN: 978-0-494-15025-2

NOTICE:
The author has granted a non-exclusive license allowing Library and Archives Canada to reproduce, publish, archive, preserve, conserve, communicate to the public by telecommunication or on the Internet, loan, distribute and sell theses worldwide, for commercial or non-commercial purposes, in microform, paper, electronic and/or any other formats.

The author retains copyright ownership and moral rights in this thesis. Neither the thesis nor substantial extracts from it may be printed or otherwise reproduced without the author's permission.

AVIS:
L'auteur a accordé une licence non exclusive permettant à la Bibliothèque et Archives Canada de reproduire, publier, archiver, sauvegarder, conserver, transmettre au public par télécommunication ou par l'Internet, prêter, distribuer et vendre des thèses partout dans le monde, à des fins commerciales ou autres, sur support microforme, papier, électronique et/ou autres formats.

L'auteur conserve la propriété du droit d'auteur et des droits moraux qui protège cette thèse. Ni la thèse ni des extraits substantiels de celle-ci ne doivent être imprimés ou autrement reproduits sans son autorisation.

In compliance with the Canadian Privacy Act some supporting forms may have been removed from this thesis.

While these forms may be included in the document page count, their removal does not represent any loss of content from the thesis.

Conformément à la loi canadienne sur la protection de la vie privée, quelques formulaires secondaires ont été enlevés de cette thèse.

Bien que ces formulaires aient inclus dans la pagination, il n'y aura aucun contenu manquant.

Canada

Summary

The light intensity in a focused femtosecond laser pulse can be high enough to initiate non-linear absorption of the radiation in otherwise transparent dielectric media. The highly localized energy deposition into the material results in permanent changes in its chemical and physical properties which can be used in the fabrication of various photonic and microfluidic devices. In this thesis we study the morphology and optical properties of the modification induced by focused femtosecond laser radiation inside fused silica and other inorganic glasses. The characterization of the modified regions is performed using a microreflection refractometry technique and the ultra-high spatial resolution technique of weak selective chemical etching followed by atomic force microscopy (AFM) and scanning electron microscopy (SEM). We demonstrate that the sample irradiation conditions strongly affect the modification morphology. Specifically, for a tight focusing geometry we identify the pulse duration-pulse energy parameter space where three distinct regimes of modification can be achieved. We also address the effects of optical aberrations on the shape, position and the intensity threshold values of the femtosecond laser induced modification. We use the combination of femtosecond laser dielectric modification and selective chemical etching to fabricate high-quality microchannels in fused silica glass. We show a dramatic dependence of the etch rate on the laser polarization and demonstrate that the high differential etch rate inside the modified regions is determined by the presence of polarization-dependent self-ordered periodic nanocracks or disordered nanoporous structures. These nanostructures are much smaller than the wavelength of the femtosecond radiation used for their formation and are the smallest objects ever created by light inside dielectric materials. Exciting potential applications of the nanostructures will be discussed.

Acknowledgements

I am deeply indebted to many people who helped me finish this thesis. In the course of my research work I was surrounded by professionals who kindly shared with me their knowledge and steered me away from many mistakes. My family in the meantime provided a loving and cozy environment for me.

First I would like to thank Rod Taylor, my supervisor and mentor. Rod immediately assessed my strengths and weaknesses and enhanced my productivity to the extent I did not expect from myself. I devoured his time and resources unlimitedly and the close proximity of his office to mine facilitated this process even further. Rod patiently listened to me when I was whining about my problems and guided me in a most efficient way to resolve them. On a daily basis Rod taught me physics and provided sound advice and new ideas. I proudly admit that the amount of supervisor's involvement that I managed to enjoy is usually shared between several students.

I would like to gratefully acknowledge the role of Thomas Brabec in my graduate study. He agreed to be my thesis supervisor and meticulously performed his duty until Rod became an adjunct professor with the University of Ottawa and eventually my primary thesis supervisor. In fact, without Thomas' initial support I would not have been able to start the Ph.D. program at all.

I have been fortunate over the last five years to work in tight collaboration with Paul Corkum's femtosecond laser group at the Steacie Institute for Molecular Sciences. Stimulating discussions with Paul, Rod, David, Eli, Ravi, and Rajeev provided critical input for many experiments described in this thesis. Eli has also been a good friend throughout all my work.

It is very difficult to overstate the contribution of Wayne Boland and Jeff Fraser in the sample preparation and data acquisition process. During the years of my involvement in the femtosecond laser dielectric modification projects Wayne has cut and polished literally hundreds of glass samples and Jeff has recorded thousands of high-quality SEM images which constitute a good half of the artwork in our recent articles.

I thank the National Research Council of Canada and the Institute for Microstructural Sciences in particular for providing me with financial support and for giving me full access to the equipment and other resources. I also thank the University of Ottawa for awarding me an Admission Scholarship which supported all my years of graduate study.

Finally, I would like to thank my two-year old son Sasha for the profound understanding of his father's temporary difficulties and providing us with minimum four hours of sleep every night since the very first day he discovered this wonderful world.

Statement of originality

This is an article-format thesis based on five published articles (ARTICLES I-V) and one submitted manuscript (ARTICLE VI). ARTICLES I-V are direct reprints taken from the journals. The thesis presents mainly experimental work on ultra-high spatial resolution characterization of femtosecond laser modification of glasses, but also includes some simulations and modeling. One notable exception is ARTICLE I where the microreflection technique (reflection refractometry) which we extensively used to characterize the refractive index changes produced by a focused femtosecond laser beam in various glasses was applied to study electron-beam written optical waveguides in germanium doped flame-hydrolysis silica. ARTICLE I was conceived and written by Dr. Garcia-Blanco. The text and data pertaining to the microreflection technique were provided by me.

The experimental study of the femtosecond radiation-induced modification in glasses included two major stages: i) irradiation of the samples and ii) characterization of the modification morphology and the optical properties of the induced changes. The femtosecond writing was done by Dr. Simova, Dr. Bhardwaj and Dr. Rajeev, whereas I performed the characterization of the samples and fabricated the microchannels using chemical etching. The experimental setups used for the diagnostics were designed and built by me with critical suggestions offered by Dr. Taylor (my thesis supervisor). All the data acquisition (except scanning electron microscopy), processing, simulations, and analysis were done by me. The nanoplasmonics model of the nanograting formation (included in ARTICLE VI and **Section 2**) was proposed by my colleagues.

In ARTICLE II I analyzed the refractive index changes in, and the morphology of the femtosecond laser-modified regions using the microreflection technique and the technique of selective chemical etching followed by atomic force microscopy, respectively. ARTICLES III-VI were written by me with the crucial input of my thesis supervisor and the coauthors. The work presented in my thesis is, to the best of my knowledge, new and original.

Contents

Introduction

The laser provides a unique tool for machining a wide variety of materials. The advantages of laser-assisted material processing over other methods stem from the relative ease with which the laser beam can be delivered to and manipulated at the sample. Laser processing is inherently contactless, it does not require sophisticated vacuum equipment and easily adapts to various sample shapes. In general, the technique is based on the conversion of light into heat and is therefore strongly dependant on the dynamics of heat deposition into the medium. By using femtosecond (1 fs = 10^{-15} s) laser pulses the material heating caused by the radiation-matter interaction becomes deterministic, highly localized and efficient. In this regime the heat diffusion from the interaction volume and, consequentially, the heat affected zone surrounding the machined area are significantly reduced allowing high quality microstructuring of the sample. Commercially available laser systems generating powerful sub-picosecond (or femtosecond) pulses have been used to achieve unmatched accuracy (down to 50 nm) in micromachining of various materials [1]. Even though virtually any material can be machined with the same femtosecond laser, the radiation absorption mechanism can be quite different depending on whether the medium to be processed is transparent at the laser wavelength or not. In opaque materials, e.g., metals and narrow bandgap semiconductors, linear absorption will be the dominant mechanism to modify the material. On the other hand, in transparent, wide bandgap dielectrics the radiation absorption is governed by essentially non-linear ionization processes. To achieve extremely high light intensities necessary to initiate multiphoton absorption, the femtosecond radiation has to be focused tightly inside transparent materials. Due to the essentially nonlinear nature of the laser pulse-matter interaction in this case, the material surrounding the focal volume remains unaffected by the light passing through it, nominally allowing structures to be written with sub-micrometer accuracy at any depth in three-dimensions (3-D).

In this thesis we study properties of modification induced by focused femtosecond (fs) laser radiation inside inorganic optical glasses. The main effort has been dedicated to 3-D characterization of the modification morphology in fused silica (synthetic quartz glass) which is one of the most widely used materials in various fs laser-assisted micromachining applications. The previous work in this field has demonstrated that in some glasses (and crystals) fs irradiation induces the production of positive refractive index changes in the modified zones and enables fabrication of optical waveguides and other micro-photonic devices embedded in bulk material [2-8]. Focused fs laser radiation has also been used to either assist [9-11] or directly fabricate microchannels [12-13] in various glassy media. The microchannel fabrication technique based on the fs irradiation of the samples with subsequent selective chemical etching in a water solution of hydrofluoric acid (HF) is the technique explored in the thesis [13]. The ability to fabricate microchannels and micro-photonic elements in 3-D and integrate them in a single block of glass using one writing laser makes femtosecond laser-assisted micromachining a promising alternative technique to the design of micro-total analysis systems (μ-TAS) and biochip devices [14] designed for high-speed and efficient analysis of nano- (and pico-) liter volumes of (bio)-chemical reagents and biological species.

Although the basic physical mechanisms involved in the fs radiation absorption in transparent medium are becoming understood, there is still no clear picture of how the modification is actually produced. Studies of fs laser modified regions inside various glasses have identified different regimes depending on the light intensity at the focus, viz. the production of: i) smooth refractive index changes [2, 15] ii) inhomogeneous modification [15, 16] and iii) micro-voids [17]. This is not a very surprising result, as the non-linear absorption is highly dependent on the light intensity. The intensity itself is a function of the pulse duration and pulse energy, but also depends on how tightly the laser beam is focused in the material, which immediately makes the numerical aperture of the focusing optics a crucial parameter. In addition, the air-sample interface introduces spherical aberration which dramatically alters the peak intensity and the shape of the focal volume depending on the focusing depth and, once again, the numerical aperture. Investigation of the fs laser dielectric modification becomes even more challenging, if one takes into account that the order of the non-linear absorption as well as the theoretical minimum focal spot size in the material are determined by the laser wavelength, another parameter. The radiation intensity at the focus, however, is not the only major parameter affecting the modification process. During my thesis research we have found that the state of the laser beam polarization appears to be one of the key, if not dominant, factors influencing the modification morphology.

The purpose of my research is to establish the link between the laser parameters and other writing conditions and the modification morphology and to define regimes of modification most suitable for 3-D integration of optical waveguides and microchannels into a single block of glass. The presented thesis is based on five published articles (ARTICLES I-V) and one submitted manuscript (ARTICLES VI). We first develop and refine ultra-high spatial resolution diagnostics techniques of selective chemical etching followed by atomic force microscopy (AFM) (resolution ~ 15 nm) and/or scanning electron microscopy (SEM) (resolution ~ 5 nm) to study the morphology of fs radiation modified zones. The article which describes this technique is included in Appendix B. We also use a high resolution technique based on microreflection to characterize refractive index changes in fs laser-irradiated glasses and near-field scanning optical microscopy (NSOM) to characterize the mode structure at the output of fs laser-written waveguides. The detailed description of the microreflection technique is presented in ARTICLE I, where it was applied to map the refractive index profiles of electron beam-written optical waveguides in germanium doped flame-hydrolysis silica. In ARTICLE II this technique has been successfully used to obtain refractive index profiles of the fs radiation-induced modification in synthetic quartz glass (fused silica, SiO_2) and other multicomponent optical glasses and to validate the technique of chemical etching and AFM. ARTICLES III and IV are dedicated to ultra-high resolution studies of the effects of the laser parameters and writing conditions on the morphology and shape of fs radiation induced modification. ARTICLE III describes ultrahigh resolution studies of the photo-induced modification in fused silica produced at various depths by tightly focused femtosecond laser radiation affected by spherical aberration. Even though spherical aberration has been the subject of extensive theoretical and experimental studies, in the fs laser dielectric modification domain we are the first to demonstrate that shapes of the irradiated zones near the threshold for modification can be predicted by taking proper account of spherical aberration caused by the refractive index mismatched air-glass interface. ARTICLE IV investigates the formation of polarization-sensitive nanogratings in the moving fs laser focus inside fused silica and identifies regimes suitable for fabrication of low loss optical waveguides and microchannels. ARTICLES V and VI, reinforced with the previous findings on the modification morphology, demonstrate the capabilities of fs laser micromachining to assist in fabrication of microchannels in glasses. In ARTICLE V we discover a dramatic dependence of the etch rate on the fs laser polarization and establish the existence of a pulse energy threshold at which etching of the laser-modified zones becomes highly polarization selective. In ARTICLE VI we provide a detailed description of the dielectric modification morphology and correlate it with the etch rate of microchannels produced by fs irradiation of fused silica with subsequent etching in hydrofluoric acid. By studying the modification morphology and the dynamics of fluorescent dye penetration into the modified regions in fused silica we show for the first time that the mechanism responsible for the highly selective chemical etching is caused by the formation of polarization-dependent self-ordered nanostructures - nanocracks for linear polarization and nanovoids for circular polarization - inside the fs laser modified zones. We also demonstrate that only certain types of modification morphology, which are determined by the fs laser and writing parameters, ensure the production of millimeter-long microchannels with regular cross-sectional shapes and smooth walls.

This thesis consists of the Introduction (**Sections 1** and **2**), the Main part, and the Conclusion. **Section 1** introduces basic mechanisms affecting femtosecond pulse propagation and non-linear interaction with transparent media. **Section 1** also provides a theory of spherical aberration caused by focusing through a dielectric interface and thus complements ARTICLE III where we present mainly the experimental data and results of simulations. **Section 2** describes different types of fs radiation-induced modification in glasses and overviews the diagnostics techniques we have developed and used for its characterization (selective chemical etching followed by AFM/SEM, microreflection technique (reflection refractometry), and NSOM). **Section 2** also provides additional technical details pertaining to the diagnostics techniques that went beyond the scope of the ARTICLES I-VI. In the Main part, which constitutes the body of the thesis and is comprised of ARTICLES I-VI, we apply the diagnostics techniques to characterize the modified regions in different glasses and elaborate on the tight link between the writing conditions (such as the laser polarization, pulse energy and pulse duration, quality of the laser focus) and the modification morphology. We also establish the regimes of modification that are most suitable for the fabrication of microchannels and waveguides. In the Conclusion we review the results of the thesis research work and discuss possible further experiments.

Section 1. Femtosecond pulse interaction with dielectrics

The modification of pure wide bandgap dielectrics with femtosecond laser pulses is initiated by rapid ionization of the medium. The excitation of the electrons can induce modification in the medium via several mechanisms. The electron plasma produced by nonlinear absorption of the radiation will locally heat the medium by the electron-lattice collision interactions. Local heating means that the extent of the distributed heat source represented by the hot electron plasma will be confined to the volume where the light intensity was sufficient to ionize the medium. The low heat capacity of electrons allows them to be heated to extremely high temperatures ($\gg 10^3$ K) [17] keeping the lattice cold due to the relatively long electron-phonon relaxation time (10^{-12} s) [18]. Eventually after a few picoseconds the lattice will also be heated up and structural changes due to melting and resolidification of the material may develop depending on the amount of energy deposited. Nonlinear absorption can also lead to the formation and accumulation of color centers and other defects whose presence alters the properties of the irradiated medium. A discussion of possible mechanisms of fs laser dielectric modification is postponed to **Section 2**.

In practice the potential of the fs laser dielectric modification technique is determined by the ability to predict and control the fs laser light intensity distribution inside the material both in space and time. On its way from the laser system to the volume inside the material where the modification occurs the pulse is first focused with external optical elements, then refracted at the sample surface and, finally, it nonlinearly interacts with the dielectric medium. Pulse focusing and refraction can be described using the formalism of linear optics and diffraction theory. On the other hand, the light intensity near the focus inside the sample becomes very high and the nonlinear optical response of the medium to the electromagnetic field associated with the pulse has to be taken into account. Inside the sample, an intense focused laser pulse alters optical properties of the medium and ionizes it, which, in turn, affects the space-time intensity distribution in the pulse and therefore its capability to interact with and induce changes in the dielectric. **Section 1** first considers different nonlinear optical mechanisms affecting the ultra-short pulse propagation and then concentrates on the effects causing pulse distortion in the focusing optics and at the sample surface.

Nonlinear refractive index

The light interaction with transparent nonmagnetic medium can be described in terms of the light-induced electric polarization ***P*** and associated with it other macroscopic optical characteristics such as dielectric constant (dielectric permittivity) ε and refractive index n. An incident electromagnetic field ***E*** polarizes the medium and each volume element then becomes a source of secondary waves whose strength is related to ***P***. The secondary waves interfere with each other and with the incident wave thus forming the total electromagnetic field propagating in the medium. A wave equation for the electric field in the medium can be derived from the Maxwell equations, where the source term represented by ***P*** accounts for the influence of the medium on the field [19]

$$\left(\nabla^2 - \frac{1}{c^2}\frac{\partial^2}{\partial t^2}\right)\boldsymbol{E}(\boldsymbol{r},t) = \mu_0 \frac{\partial^2}{\partial t^2}\boldsymbol{P}(\boldsymbol{r},t). \tag{1}$$

In this equation μ_0 is the permeability of free space.

For strong fields, the response of the medium to the propagating field can be expressed by expanding ***P*** in powers of ***E***

$$P_i = \varepsilon_0\left(\chi_{ij}^{(1)}E_j + \chi_{ijk}^{(2)}E_jE_k + \chi_{ijkl}^{(3)}E_jE_kE_l + \cdots\right), \tag{2}$$

where the tensors denoted by $\chi_{ij\ldots n}^{(n)}$ are the optical susceptibilities of the n-th order and E_i are the components of the electric field vector ***E***. This expansion also assumes that the terms of the series become smaller as their number increases. The ratio of two successive terms can be approximated as [20]

$$\left|\frac{\chi_{ij\ldots n+1}^{(n+1)}E_{j\ldots n+1}}{\chi_{ij\ldots n}^{(n)}E_{j\ldots n}}\right| \propto \left|\frac{E}{E_{\mathrm{at}}}\right| \ll 1, \tag{3}$$

which shows that the perturbing field should be much weaker than the characteristic atomic field E_{at} (~10^9 V/cm).

In linear optics only the first term is retained and for not too strong electric fields the terms above the 3-rd order in expression (2) can be discarded. In an isotropic medium, due to the symmetry properties imposed on the system, (e.g., glasses) only diagonal elements $\chi_{ii}^{(1)} \equiv \chi^{(1)}$ are left, all 2-nd order terms vanish $\chi_{ijk}^{(2)} \equiv 0$, and the remaining independent nonzero 3-rd order components $\chi_{iijj}^{(3)}$, $\chi_{ijij}^{(3)}$ and $\chi_{ijji}^{(3)}$ are constrained with a condition $\chi_{iijj}^{(3)} + \chi_{ijij}^{(3)} + \chi_{ijji}^{(3)} = \chi_{iiii}^{(3)} \equiv \chi^{(3)}$ [19]. The off-diagonal 3-rd order terms can be a source of the nonlinearly induced birefringence in isotropic materials. For the simplest case of linearly polarized light expression (2) then reduces to

$$\boldsymbol{P} = \varepsilon_0\left(\chi^{(1)} + \frac{3}{4}\chi^{(3)}|\boldsymbol{E}|^2\right)\boldsymbol{E} = \varepsilon_0\chi(I)\boldsymbol{E}, \tag{4}$$

where the dependence of the susceptibility on the light intensity I is emphasized. Obviously, an intensity dependence is also imposed on both the dielectric permittivity of the medium ε, defined by $\varepsilon = \varepsilon_0(1+\chi)$, and the refractive index n related to ε via $n = (\varepsilon\mu/\varepsilon_0\mu_0)^{1/2}$. For dielectrics, μ is very close to μ_0 and the refractive index can be defined as $n = (\varepsilon/\varepsilon_0)^{1/2}$ or, using (4), as

$$n = \sqrt{1 + \chi^{(1)} + \frac{3}{4}\chi^{(3)}|\boldsymbol{E}|^2} \tag{5}$$

By defining the "linear" refractive index n_0 as $n_0 = \sqrt{1+\chi^{(1)}}$ and taking into account that the field-dependent term is usually small, (4) can be rearranged as

$$n = n_0 + n_2 I, \; n_2 = \frac{3\chi^{(3)}}{4\varepsilon_0 c n_0^2}, \tag{6}$$

where the nonlinear refractive index n_2 is introduced. The intensity dependence of the refractive index (optical Kerr effect) can be caused by different physical mechanisms. In undoped glasses, non-resonant electron excitation processes with characteristic response times on the order of $\sim 10^{-15}$ s provide the main contribution to the nonlinearity in the refractive index, which is typically $n_2 \sim 10^{-16}$-10^{-15} cm^2/W [20]. However, the slower response (Raman response) due to nuclear vibrations excited by the optically induced perturbation of the electronic structure can provide up to 20% of the total nonlinear response of the medium [21]. The characteristic Raman response time is on the order of 10^{-13} s. Smaller n_2 usually correspond to faster response times.

Solving the full vector wave equation (1) in a nonlinear medium is very difficult because of the linear and nonlinear coupling between the components of the electric vector $\boldsymbol{E}$. To simulate the propagation of an intense laser pulse in a non-absorbing medium equation (1) is usually approximated with the nonlinear Schrödinger equation (NLSE) [22]. NLSE describes many aspects of the pulse propagation but is much easier to solve than (1). Strictly speaking, the NLSE accounts only for an instantaneous Kerr nonlinearity, dispersion and diffraction. However, higher order effects such as third order dispersion and non-instantaneous effects such as stimulated Raman scattering (the response time ~100 fs) can also be included into the NLSE [21]. The nonlinear response of the medium affects the spatial and temporal characteristics of the propagating fs pulse in different ways. The spectrum of the initially bandwidth or Fourier limited pulse can substantially broaden and become asymmetric, which in the extreme case of weakly focused and powerful pulses results in the white light continuum generation [23]. The spatial intensity distribution across the pulse can change dramatically and the pulse itself can split both in time [21] and space [24]. Some important effects predicted by the NLSE, viz. self-focusing, self-phase modulation and splitting of fs pulses are briefly described below.

Self-focusing. The inhomogeneity in the refractive index induced by the propagating pulse leads to nonlinear refraction. The field (intensity) over the front of a typical (Gaussian) laser beam is higher on the beam axis, which, provided that n_2 is positive, will produce a refractive index distribution with its maximum also lying in the beam center. The induced graded index lens will deflect off-axis light towards the axis and therefore promote self-focusing of the beam. The diffraction occurring on the induced index inhomogeneity, however, tends to defocus the beam and the regime of propagation will depend on which effect dominates. Numerical calculations performed for laser radiation with a Gaussian spatial profile at a wavelength of λ showed the existence of a critical power P_{cr} [25]

$$P_{\mathrm{cr}} = \frac{3.77\lambda^2}{8\pi n_0 n_2} \tag{7}$$

above which self-focusing will prevail and eventually lead to the beam collapse in the medium within the Rayleigh range (i.e., the beam confocal parameter) for both prefocused and collimated geometries. Experiments have also shown that the power threshold for supercontinuum generation coincides with the critical power for self-focusing, e.g., [26]. Supercontinuum generation is observed with weakly focused fs pulses, whereas otherwise identical but tightly focused pulses can cause material modification without supercontinuum generation. For an externally focused laser beam self-focusing shifts the focus towards the lens from its original position and at powers $P < P_{\mathrm{cr}}/4$ decreases the focused spot size approximately by a factor of $(1\text{-}P/P_{\mathrm{cr}})^{1/2}$, which leads to the intensity enhancement given by $(1\text{-}P/P_{\mathrm{cr}})$ near the focus [25]. When the input power is significantly greater than $P_{\mathrm{cr}}/4$ the more complete numerical solution must be used in order to compute the reduced focal spot size (or enhanced intensity) due to self-focusing. A comparison between the above approximation and the exact numerical solution provided in Ref. [25] can be found in the article by Soileau *et al.* [27]. Although this approximate formula cannot be used for accurate calculations of the intensity enhancement, it correctly predicts the beam collapse at a power of P_{cr}. As the laser focus is approached, however, dispersion effects together with defocusing and absorption caused by the plasma formation due to photoionization (See below) come into play and prevent the beam from the predicted collapse to singularity. Moreover, at the very high intensities occurring near the focus the approximations made in (3) and (4) become inaccurate and higher order nonlinear terms should be considered. In applying formula (7) to pulsed radiation, it is the peak power $P_{\max}$ of the pulse that should be compared with the critical value. $P_{\max}$ is related to the pulse duration τ_{p} (full width at half maximum, FWHM) and pulse energy E_{p} by $P_{\max} = 0.94\ E_{\mathrm{p}}/\tau_{\mathrm{p}}$ for a pulse with a Gaussian spatial and temporal profiles and by $P_{\max} = 0.88\ E_{\mathrm{p}}/\tau_{\mathrm{p}}$ for a pulse with a Gaussian spatial profile and sech^2 temporal profile [28]. In any case, it appears that $P_{\max}$ can be approximated by $E_{\mathrm{p}}/\tau_{\mathrm{p}}$.

In using ultrashort pulses for dielectric modification self-focusing and other nonlinear effects can be reduced[1] by focusing them with high numerical aperture (NA) optics[2] and operating at low peak powers. The above mentioned approach is based on the fact that ionization needed to modify the material is determined by the light intensity, whereas self-focusing is both an intensity- and power-dependent phenomenon. Tight focusing of low pulse energy pulses allows one to reach the material modification threshold intensities[3] I_{th}

---

[1] At this point it should be emphasized that the widely accepted negative role of self-focusing in fs laser material modification is determined by the difficulty to control this essentially nonlinear phenomenon rather than by some inherent features associated with it which would adversely affect the modification process.

[2] In microscopy the numerical aperture, NA, is defined as the product $n\sin(\theta)$, where θ is the semi-angle of the cone of rays from the axial object point which is intercepted by the front lens of the objective and n is the refractive index of the medium (e.g., immersion fluid) of the object space [30]. In using objectives to focus light, θ defines the maximum angle between the marginal rays leaving the objective and the optical axis. In focusing in air with $n = 1$ ('dry focusing' as opposed to focusing in immersion liquids with $n > 1$) $\mathrm{NA} = \sin(\theta)$.

[3] The pulse peak intensity $I_{\max}$ is related to the pulse peak power $P_{\max}$ by $I_{\max} = P_{\max}/S_{\mathrm{eff}}$, where S_{eff} is the effective minimum cross-sectional area of the focal spot. The radial intensity distribution of the fs laser beam incident on the focusing objective can be approximated by a Gaussian intensity profile $I(r) \propto \mathrm{e}^{-\frac{2r^2}{w^2}}$, where w denotes the radius at which the intensity falls to $1/\mathrm{e}^2$ of its peak or axial value. The focusing objective aperture inevitably truncates the incident beam, which affects the intensity distribution in the focus. In calculations it is helpful to introduce the truncation ratio $T = w/r_{\mathrm{ob}}$, where r_{ob} is the beam-limiting aperture radius. It can be

while keeping the power essentially below P_{cr} where self-focusing can be neglected [29]. For example, for fused silica $I_{th} \approx 1.5 \times 10^{13}$ W/cm^2 at a wavelength of 0.8 μm can be achieved at a pulse duration of $\tau_p = 100$ fs and a pulse energy of only $E_p \approx 55$ nJ in using a NA = 0.45 focusing objective (one of the NA's used in the experiments in ARTICLE VI), which keeps the peak power in the pulse ($P_{max} \approx 0.55$ MW) almost an order of magnitude below the critical power for self-focusing $P_{cr} \approx 4.3$ MW [34]. The situation is dramatically changed in focusing with low-NA optics. For NA = 0.1 and $\tau_p = 100$ fs, the threshold intensity can be achieved at a peak power of $P_{max} \approx 11$ MW, which exceeds P_{cr}. We will show later in ARTICLES IV, V and VI, where we extensively use a NA = 0.65 objective, that the most interesting and practical regimes of modification in fused silica are observed at 50 nJ < E_p < 400 nJ and $\tau_p \approx 100$ fs, i.e., even for the most energetic pulses P_{max} is below P_{cr}. In order to study how self-focusing affects the shape and size of the modified regions we analyzed the modification in fused silica produced at varying pulse durations 40 fs < τ_p < 500 fs while E_p as well as all other experimental parameters were kept at fixed values. We operated at pulse energies allowing us to be well below the critical power P_{cr} with long pulses (500 fs) and exceed P_{cr} with very short (40 fs) pulses. The technique of selective chemical etching followed by AFM revealed that the modified regions in the yz-cross-sections[4] are only ~10-

---

shown [31,32] that the radial intensity distribution at the focal plane, I_f, of a truncated Gaussian beam is given by $I_f(r_f) \propto \left[\int_0^1 e^{-\frac{\rho^2}{T^2}} \mathbf{J}_0(\pi\rho r_f)\rho d\rho\right]^2$, where $\rho = r/r_{ob}$ is the normalized aperture coordinate, $r_f = \frac{2\mathrm{NA}}{\lambda\sqrt{1-\mathrm{NA}^2}}\xi$ is the normalized focal coordinate (ξ is the radial distance from the optical axis in the observation plane), λ is the wavelength in the medium, and $\mathbf{J}_0$ is a Bessel function of the fist kind of the zero order. If the objective truncates the beam at the 1/e^2-level, i.e., $T = 1$, the minimum achievable focal spot diameter at the 1/e^2-level is approximated by $d_{min} = 2w_0 \approx \lambda/\mathrm{NA}$. At this level ≈ 86% of the pulse energy is confined within the focal spot size. Therefore, one may adopt the 1/e^2-level criterion for the focal intensity to define S_{eff} as $S_{eff} = \pi w_0^2$. It is also possible to approximate the essentially non-uniform focal intensity distribution by a uniform "top hat" distribution with the same peak intensity and energy confinement, which results in a two times smaller S_{eff} [33]. Obviously, I_{max}, as well as the threshold intensity I_{th}, depends on the definition of S_{eff}. In our calculations we use the $S_{eff} = \pi w_0^2$ definition. On the other hand, e.g., Schaffer *et al.* [34] adopt the "top hat" definition resulting in a two times higher I_{th}.

Several different techniques can be used to determine the intensity threshold I_{th} for bulk modification in transparent materials, e.g., Ref. [34]. In order to measure I_{th} we used i) optical microscopy (in the bright illumination mode) and ii) the combined technique of selective chemical etching and AFM on cut and polished samples. The threshold is defined as the minimum intensity producing an optical and/or topographic signature, respectively.

[4] The z-axis is aligned along the pulse propagation direction and the y-axis is perpendicular to the writing direction which coincides with the x-axis. In ARTICLE VI we describe the writing geometries and explain in detail how the irradiated samples are prepared for the characterization.

20% longer and narrower in the strong self-focusing regime than in the case when essentially sub-critical powers were used.

Self-phase modulation (SPM). The intensity dependence imposed by strong fields on the refractive index also makes it vary in time. The extremely fast response time of the refractive index change in glass also allows it to follow the variations in the pulse intensity almost instantaneously. In this case, a refractive index modulation follows the traveling pulse. The maximum change occurs in the center of the pulse and then it gradually decreases towards the pulse leading and trailing edges thus mapping the intensity distribution along the propagation direction. The confinement of the pulse inside such an inhomogeneity of the refractive index leads to a phase change along the pulse (self-phase modulation, SPM) resulting in a significant broadening of the pulse spectrum. An expression for the phase variation in time $\partial\varphi/\partial t$ [20]

$$\frac{\partial\varphi}{\partial t} = \omega - \frac{n_2 \omega z}{c}\frac{dI(t)}{dt}, \tag{8}$$

where ω is the pulse carrier frequency, shows that the instantaneous frequency (i.e., phase time derivative) becomes lower at the leading edge of the pulse ($dI/dt > 0$) and higher at its trailing edge ($dI/dt < 0$) and the magnitude of this effect grows with the propagation length in the medium, z. SPM leads to pulse spectral broadening, which, due to the group velocity dispersion (GVD)[5], causes pulse spreading in space and decreases its peak intensity (and power). This, in turn, weakens the intensity-dependent self-focusing effect.

Pulse splitting. Self-focusing sharpens a propagating pulse both in space (and time) concentrating the off-axis energy near the pulse peak. Increasing the peak intensity intensifies SPM and therefore promotes the generation of new spectral components in the pulse. The pulse envelope, due to GVD, will start reshaping with the maximum transformations occurring in the most modulated part of the signal, viz. in the center of the pulse where intensity is highest. GVD tends to redistribute the energy from the center towards the pulse leading and trailing edges, which eventually leads to pulse splitting [21]. This effect also reduces the peak intensity in the pulse and therefore counteracts self-focusing.

---

[5] The group velocity dispersion is usually defined as the derivative of v_g with respect to the wavelength, i.e., $dv_g/d\lambda$.

In spite of the complexity of the effects associated with the induced nonlinearity in the medium, Luther *et al.* [35] have shown that the solutions of the NLSE in normally dispersive media (which is the case for many optical glasses for $\lambda < 1300$ nm) describing the propagation of a Gaussian fs pulse are determined by only two parameters: i) the ratio of the diffraction length L_{DF} to the dispersion length[6] L_{DS}, $\eta = L_{\mathrm{DF}}/2L_{\mathrm{DS}}$ measuring the strength of the dispersion relative to the diffraction and ii) the ratio of the peak input pulse power P to the critical power P_{cr}, $p = P/P_{\mathrm{cr}}$. The pulse evolution is determined by the relation between the nonlinear dispersion length scale z_{NLGVD} [35]

$$z_{\mathrm{NLGVD}}(p,\eta) \approx 0.5L_{\mathrm{DF}}\left\{\frac{\left[3.38+5.2(p^2-1)\right]^{1/2}-1.84}{15\eta p}\right\}^{1/2}$$

and the self-focusing length scale z_{SF} [25]

$$z_{\mathrm{SF}}(p) \approx \frac{0.183L_{\mathrm{DF}}}{\left[(p^{1/2}-0.852)^2-0.0219\right]^{1/2}}.$$

In Ref.[34] the authors also introduce a threshold power $P_{\mathrm{th}} = p_{\mathrm{th}}P_{\mathrm{cr}}$ at which $z_{\mathrm{NLGVD}} = z_{\mathrm{SF}}$. For p's below the threshold value p_{th} the nonlinear effects are weak and only slightly affect the pulse propagation. As p approaches and exceeds the threshold value the nonlinear response of the medium becomes critical in defining the evolution of a fs pulse. For example, the model predicts pulse splitting occurring at or before the focus of the pulse and pulse filamentation for p's well above p_{th}. Simulations performed by Luther *et al.* [35] show that for $\eta \ll 1$ (i.e., diffraction dominated regime of high-NA focusing) p_{th} is close to unity, but increases with η and at $\eta \approx 1$ it equals ≈ 4. Therefore, for very weakly focused fs pulses propagating in dispersive media the self-focusing threshold power is significantly higher than for continuous radiation (or non-dispersive media). On the other hand, for tightly focused pulses operation below the critical power P_{cr} is essential to avoid difficult to control

---

[6] The dispersion length is defined as $L_{\mathrm{DS}} = \tau_{\mathrm{G}}^2 \big/ 2|k''|$ [20], where k'' is $k'' = \frac{\lambda}{2\pi c^2}\left(\lambda^2 \frac{d^2 n}{d\lambda^2}\right)$ [20]and τ_{G} for a Gaussian pulse is related to the pulse duration τ_{p} FWHM as $1.177\tau_{\mathrm{G}} = \tau_{\mathrm{p}}$. Bandwidth limited Gaussian pulses double their length after propagation of $\approx 1.662\ L_{\mathrm{DS}}$ [20]. The diffraction length is $L_{\mathrm{DF}} = n\pi w_0^2 \big/ \lambda$, where n is the refractive index of the medium, w_0 is the laser beam waist, and λ is the pulse central wavelength. For fused silica at $\lambda = 800$ nm, $d^2n/d\lambda^2 = 0.40 \times 10^{-1}$ [μm^{-2}] [20] and the dispersion length of a 100 fs pulse is ≈ 4.8 cm. The diffraction length of a tightly focused beam ($w_0 \sim 0.5$ μm) is a much smaller quantity on the order of microns. Therefore, $L_{\mathrm{DS}} \gg L_{\mathrm{DF}}$ and $\eta \ll 1$.

effects caused by self-focusing. However, in using high-NA optics (See below) the effects associated with the electron plasma formation dominate over self-focusing and diminish its role in determining the shape and size of the modified regions.

Electron plasma generation

Multiphoton ionization. In a defect-free wide bandgap dielectric, where single photon (or linear) absorption cannot directly promote electrons from the valence to the conduction band, nonlinear absorption comes into play. In this case, simultaneous absorption of multiple photons must occur to ionize the material. The minimum number of photons m to achieve this is determined by the relation $m\hbar\omega > E_g$, where E_g is of the energy bandgap of the dielectric and $\hbar\omega$ is the photon energy expressed in terms of the angular laser frequency ω. In amorphous media there is no well defined bandgap structure due to the absence of long-range order in the material and in this case an effective bandgap (also denoted by E_g) correlated with their absorption edge [36, 37] can be defined. Even though there are no well-defined bands for glasses, the calculated density of states can still identify the valence band maximum and the conduction band minimum [38]. Ionizing radiation, particle irradiation or optical excitation (e.g., fs laser irradiation) can generate vacancies and interstitials in originally 'pure' material and the presence of such induced defects can shift the absorption edge of the glass, e.g., Ref. [39]. In silicate glasses E_g ranges from approximately 3.5 eV (multicomponent glasses) to 7.5-8.2 eV (UV-grade synthetic quartz glass (SiO_2)). The multiphoton ionization rate is determined by $\sigma_m I^m$, where σ_m is the cross-section of m-photon absorption[7] (absorption coefficient) and I is the radiation intensity. The absorption coefficient of a multiphoton process (e.g., at least 5 photons at the laser wavelength of 800 nm need to be absorbed for SiO_2) is usually a small number and the fs laser beam has to be focused tightly to obtain the needed light intensities.

The multiphoton ionization can also be localized to sub-diffraction volumes [1, 40]. This can be illustrated by the following simple analysis . For a Gaussian TEM_{00} laser beam (an ideal situation), the lateral intensity distribution in the laser focus is defined by $I = I_0$exp[-

---

[7] The intensity I (or energy flow) of an electromagnetic wave is the power (in energy/sec) transmitted through a unit area (e.g., cm^2) oriented perpendicular to (normal to) the propagation direction of the wave, and the ionization rate (the probability per unit time) has the units of sec^{-1}. Then, the m-photon cross-section has the units $[\sigma_m] = \mathrm{cm}^{2m}\mathrm{sec}^{m-1}$, which reduces to the usual units of cm^2 for linear absorption (m = 1).

$2(r/w_0)^2]$, where r is the radial coordinate and w_0 is diffraction-limited focal spot radius at the $1/e^2$-intensity level. The essentially nonlinear dependence of the m-photon ionization rate on the intensity ($\sim I^m$) will tend to confine the absorption process to a lateral size given by $\exp[-2(r\sqrt{m}/w_0)^2]$, which is by a factor of $\sqrt{m}$ less than one would expect in the case of linear absorption.

Tunneling ionization. The superposition of the nucleus' Coulomb field and the laser radiation electric field produces an oscillating potential well confining the electrons. For very strong fields the potential barrier during the oscillation period can be suppressed enough to allow the electrons to tunnel through it and escape the atom. The tunneling ionization rate is proportional to $\exp[-2\ (2m^*E_g^3)^{1/2}/3ehE]$, where E is the strength of the applied electric field (i.e., the laser field) and m^* and e are respectively the effective mass and charge of an electron. This expression is nothing else than the probability of extracting an electron from a potential well of a depth E_g with a constant electric field E [41]. The contribution of tunneling ionization to the electron plasma production is expected to become significant at intensities $I > 10^{14}$ W/cm^2 attainable with very short and energetic laser pulses.

Both multiphoton ionization and tunneling ionization have been considered using one theoretical model by *Keldysh* [42], where he calculated the transition probability of an electron from the initial unperturbed state to the final state perturbed by the external field. Keldysh also introduced the adiabaticity parameter (known as the Keldysh parameter), γ, determining the transition between the two ionization mechanisms. The Keldysh parameter in solids can be defined as $\omega(2m^*E_g)^{1/2}/eE$ or $(m^*cn\varepsilon_0\ E_g/I)^{1/2}\omega/e$ [34] in terms of the amplitude of the laser electric field E or laser radiation intensity I. In these expressions c is the velocity of light, n is the refractive index of the material, and ε_0 is the permittivity of free space. The Keldysh parameter, in a semi-classical treatment of tunneling through the potential barrier in an oscillating field, can be interpreted as the ratio of the reduced tunneling time, τ_{tun}, and the period of the laser field oscillation, τ_{osc}, i.e., $\gamma = \tau_{\text{tun}}/\tau_{\text{osc}}$ [43]. When the Keldysh parameter is much larger ($\gamma \gg 1$) or smaller ($\gamma \ll 1$) than unity, the electron plasma is solely formed by multiphoton ionization or tunneling ionization, respectively. The intermediate case ($\gamma \sim 1$), which is most difficult for theoretical analysis, is considered as a combination of both ionization mechanisms. For fused silica, the modification threshold light intensity of $I_{\text{th}} \approx 1.5 \times 10^{13}$ W/cm^2 at $\lambda = 0.8$ μm yields $\gamma \approx 2.5$ corresponding to the intermediate regime.

Avalance ionization and hole-assisted ionization. Electrons generated in the conduction band in the leading edge of the pulse by photoionization start absorbing radiation through scattering of phonons (free carrier absorption or inverse Bremsstrahlung) as the rest of the pulse travels through the ionized material. When the energy of an electron in the conduction band exceeds the energy bandgap of the material, it can collisionally ionize a bound electron in the valence band. After this interaction two electrons near the conduction band minimum are produced. This process can repeat itself many times, provided that the laser pulse is intense and long enough, which will result in an exponential growth of the electrons in the conduction band or an electron avalanche. The dynamics of electron density (denoted by N) growth caused solely by avalanche ionization is described by a differential equation $dN/dt = \beta(I)N$, where the avalanche ionization rate, $\beta(I)$, according to different models can depend on the light intensity either linearly [44] or as a square root of it [45, 46]. To account for the production of free electrons by, e.g., multiphoton ionization the above rate equation is modified as follows $dN/dt = \beta(I)N + \sigma_{\text{m}} I^m \rho_{\text{at}}$, where ρ_{at} is the background atom density. The electron population growth in dielectrics is also affected by other processes occurring on a femtosecond time scale. Recombination of free carriers with a characteristic time τ_{r} (for fused silica $\tau_{\text{r}} \approx 150$ fs) can be included in the previous rate equation as: $dN/dt = \beta(I)N + \sigma_{\text{m}} I^m \rho_{\text{at}} - N/\tau_{\text{r}}$ [47].

At very short pulses (< 50 fs) providing no time for the traditional avalanche to fully develop, two other physical mechanisms which exponentially accelerate ionization become important [48, 49]. The first mechanism is collision-assisted multiphoton excitation where the energy to promote an electron from the valence to conduction band is supplied by both the laser radiation and an electron in the conduction band whose energy is less than E_g. This free electron can collisionally excite the electron from the valence band to a virtual state from which it will be excited to the conduction band by taking the rest of the needed energy from the laser photons. The other assisting mechanism is hole-assisted multiphoton absorption. In this case, the ionization rate of an atom neighboring an ion (hole) is significantly (exponentially) increased as the atom experiences the combined electric field of the ion and the incident light. Newly created ions will continue this trend in an avalanche manner. The latter mechanism also does not require any heating of the electrons in the conduction band.

To model pulse propagation in the regime of plasma formation additional terms can be phenomenologically included in the NLSE to account for the plasma absorption, plasma defocusing and the absorption due to photoionization [47, 50]. In this case the modified NLSE is solved together with the rate equation for the electron density N. In general, the produced electron plasma counteracts self-focusing and arrests the catastrophic collapse of the laser beam to a singularity. At a point near the laser focus where the intensity is sufficient to ionize the medium nonlinear absorption clamps the applied maximum intensity in the material close to the ionization threshold intensity I_i (for glasses $I_\mathrm{i} \approx 10^{13}$ W/cm^2) [51]. This reduces the positive intensity-dependent refractive index change on the axis and significantly weakens the self-focusing effect even for the initial peak powers well above P_cr. On the other hand, in the presence of free electrons the real part of the refractive index of a dielectric medium is reduced according to [52]

$$n \approx n_0 - \frac{N}{2n_0 N_\mathrm{c}} \; ; \; N_\mathrm{c} = \frac{\omega^2 \varepsilon_0 m^*}{e^2} , \tag{9}$$

where N_c is the critical plasma density ($N_\mathrm{c} \approx 2 \text{ x } 10^{21}$ cm^{-3} at $\lambda = 0.8$ μm) and N is the electron plasma density. The plasma will be generated faster and the electron density is expected to be highest at the beam axis where light intensity is maximum. In this case, the refractive index is smallest on the beam axis and increases outwards to reach its unperturbed value of n_0 where the medium is not ionized. Therefore, the produced plasma will defocus light acting as a diverging lens. By combining expressions (6) and (9) a refractive index change δn caused by both the optical Kerr effect and plasma defocusing can be obtained:

$$\delta n \approx n_2 I - \frac{N}{2n_0 N_\mathrm{c}} .$$

At $N \sim 10^{17}$-10^{18} cm^{-3} the plasma and nonlinear contributions to the refractive index change cancel each other.

Besides suppressing self-focusing, the plasma produced by photoionization and avalanche ionization also attenuates the laser pulse due to absorption, reflection and scattering. As the plasma density grows, the absorption becomes stronger and a significant fraction of the pulse energy can be dissipated in the plasma formation region. The absorption depth d (i.e. depth at which the energy density falls to 1/e of the initial value) is given by (e.g., [53])

$$d \approx \frac{cn_0(1+\omega^2\Gamma^2)}{\omega_p^2\Gamma}, \quad \omega_p^2 = N_c e^2/\varepsilon_0 m^*$$

where Γ is the decay (or relaxation) time on the order of femtoseconds for metals. When the plasma density reaches its critical value N_c light propagation in the medium becomes impossible due to very strong absorption, but even at one tenth of the critical density[8] the absorption depth at $\lambda = 0.8$ μm is only about 10 μm [28].

Focusing of femtosecond pulses

Distortion of femtosecond pulses in lenses. Tight focusing of femtosecond pulses necessary to initiate nonlinear light absorption in transparent media is usually achieved with lenses (objectives) or mirrors. However, focusing of ultrashort laser pulses using even a single lens (singlet) can lead to a significant pulse broadening and, therefore, reduction of the pulse intensity in the focus. Two effects are responsible for this. First, the pulse front, defined as the surface where the peak intensity is achieved, propagates in the lens with group velocity, whereas the phase front moves with phase velocity, i.e., the pulse front lags behind the phase front. This delay varies across the lens aperture depending on the optical path in the lens medium. For a converging lens, the delay is minimal for the marginal rays and is maximal for the paraxial rays[9], which allows the marginal rays to reach the focus first and the paraxial rays last. Such a delay or propagation time difference (PTD) observed at the laser focus can be interpreted as a pulse broadening (see Fig 1). The second mechanism of pulse broadening is caused by the group velocity dispersion (GVD) in the lens material. In his pioneering paper dealing with these effects Bor [54] showed that the temporal delay $\Delta T(r)$ between the pulse front and the phase front is given by

---

[8] A typical electron density required to cause modification in fused silica [47].

[9] The term paraxial means "near the axis", which implies that the inclination of paraxial rays to the optical axis is small. In paraxial optics, rays in an optical system are traced using an approximation where the sines of the inclination angles can be replaced by the angles themselves, i.e. sin(θ) ≈ θ (See Fig. 1). Marginal rays reach the focus from the edge of the lens aperture [30].

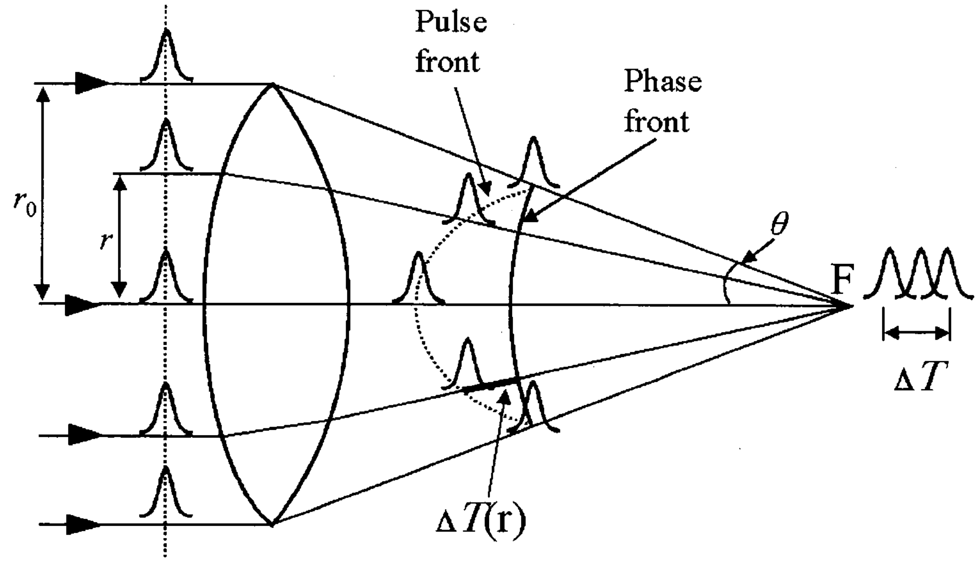

Fig.1. Pulse broadening caused by the beam-radius-dependent pulse propagation time difference in a single lens.

$$\Delta T(r) = \frac{r_0^2 - r^2}{2cf}\left(\frac{-\lambda}{n-1}\frac{dn}{d\lambda}\right) = \frac{r_0^2 - r^2}{2c}\lambda\frac{d}{d\lambda}\left(\frac{1}{f}\right), \tag{10}$$

where f is the focal length of a singlet and λ is the wavelength in vacuum. For $r = 0$, corresponding to the maximal delay, expression (10) reduces to [54]

$$\Delta T_{\max} = \frac{r_0^2}{2cf}\left(\frac{-\lambda}{n-1}\frac{dn}{d\lambda}\right) = \frac{r_0^2}{2c}\lambda\frac{d}{d\lambda}\left(\frac{1}{f}\right) = -\frac{\lambda}{2c}\tan^2(\theta)\frac{df}{d\lambda} \approx -\frac{\lambda}{2c}\theta^2\frac{df}{d\lambda}, \tag{11}$$

where θ is the angle between the marginal and axial ray (shown in Fig. 1).

Beside the temporal broadening of the pulse given by (11), the pulse is also subject to a spatial broadening due to chromatic aberration in the lens which makes different spectral components associated with a short pulse to intercept the optical axis at different locations. The chromatic spread of the focus Δf of a bandwidth limited Gaussian pulse can be estimated as [20]:

$$\Delta f = -\frac{f}{(n-1)}\frac{dn}{d\lambda}\Delta\lambda = -\frac{f\lambda^2}{c(n-1)}\frac{0.441}{\tau_p}\frac{dn}{d\lambda} \tag{12}$$

where $\Delta\lambda$ is the pulse spectral bandwidth and τ_p is the pulse duration (FWHM) related to each other by $\Delta\lambda = 0.441\lambda^2/ c\tau_p$ [20].

Temporal pulse broadening in a singlet caused by GVD is given by [54]

$$\Delta T_{\mathrm{GVD}}(r) = \frac{\lambda}{c}\frac{d^2 n}{d\lambda^2}\frac{r_0^2 - r^2}{2}\left(\frac{n-1}{f}\right)\Delta\lambda \tag{13}$$

According to (13), the delay varies across the lens aperture and attains its maximum value on the optical axis ($r = 0$) where the optical path for the rays is longest. It can also be seen from (10), (12) and (13) that the temporal broadening caused by PTD is determined solely by the focusing lens, whereas the GVD temporal broadening and the PTD spatial broadening depend both on the laser pulse and the lens. The given formulae are derived in the geometrical optics approximation neglecting spherical aberration in lenses and therefore their use, strictly speaking, can provide only an estimate of the effects. Analysis based on the diffraction theory in the presence of spherical aberration can be found elsewhere [55, 56].

The magnitude of the space-time pulse distortion in a lens due to PTD can be appreciable, e.g., focusing of 50 fs pulses with a central wavelength $\lambda = 800$ nm in a laser beam 10 mm in diameter ($r_0 = 5$ mm) with a $f = 25$ mm lens made of BK7 [10] will result, according to (11) and (12), in $\Delta T_{\max} \approx \tau_p$ and $\Delta f = 20$ µm ($\approx$ 25 % of the full width of the unaberrated axial intensity distribution given by $\approx 4\lambda/\theta^2$). On the other hand, using (13) for the same conditions gives a temporal GVD broadening of less than a femtosecond, which can be neglected.

To minimize the PTD effect, the main contributor to the pulse distortion, complex lens systems have to be used. The focal length of an ideal achromatized objective does not depend on the wavelength, $df/d\lambda \equiv 0$, and the space-time broadening given by (11) and (12) vanishes (provided that the objective is also corrected for spherical aberration, which is usually valid for achromatized objectives). In this case, the delay between the pulse front and the phase front becomes constant across the objective aperture and the pulse temporal broadening is caused only by the GVD, which contribution is now also constant for a given objective. The magnitude of the GVD-induced broadening, however, can become appreciable since high-quality objectives (especially high-NA or specialty objectives) consist of many lens elements some of which are made of highly dispersive glass. The total thickness of the optical glass in such optics can be ~2-3 cm, i.e., 20-30 times more than in the single lens considered in the previous example. In our experiments we always use achromatized microscope objectives (achromats) and the fs pulse temporal broadening due

---

[10] For BK7 optical glass at $\lambda = 800$ nm $dn/d\lambda = -2.0 \times 10^{-2}$ [µm^{-1}] and $d^2n/d\lambda^2 = 0.50 \times 10^{-1}$ [µm^{-2}] [20].

to the GVD in the microscope objectives (and other optical components) is compensated by pre-chirping the laser pulse in the compressor. Without such compensation the GVD temporal pulse broadening in some objectives (e.g., Nikon achromat, NA = 0.45, extra long working distance objective used in ARTICLE VI) can be as high as 100 fs.

Another solution is to use chromatic aberration-free reflecting optics (mirrors) or diffractive-optics elements to focus pulses. For tight focusing, mirrors should be aspheric (parabolic) to compensate for spherical aberration which can also be a source of a very significant pulse spreading both in time and space. It also should be noted that, in general case, only off-axis mirrors or on-axis two-element reflecting objectives (Schwarzchild objective) are practical, because otherwise the laser beam is inevitably intercepted (and altered) by the sample on its way to the mirror.

Spherical aberration effect. Distortion of femtosecond pulses at the air-sample interface. Before entering the sample, a fs laser pulse, as well as any other electromagnetic disturbance, is refracted at the sample surface which is considered in the analysis that follows as an interface between materials of mismatched refractive indices. The magnitude of the index mismatch is maximal for dry focusing (air-sample interface) and is significantly minimized in the case of immersion focusing when the refractive index of the immersion fluid is chosen to be as close as possible to that of the sample. The effects associated with focusing through a dielectric interface are described in the framework of the 'classical' diffraction theory and are frequently underestimated or neglected mainly because the interaction of femtosecond pulses with medium is considered a purely nonlinear phenomenon. Although the dielectric modification is indeed caused by nonlinear ionization processes, these processes themselves are governed by the light intensity distribution in the interaction volume, which, at least in the case of high numerical aperture focusing, appears to be dominated by the effects associated with the presence of a refractive index step in the path of the pulse. During the research presented in this thesis (ARTICLE III) we have demonstrated for the first time that spherical aberration due to a planar air-silica interface accounts for the shapes and positions of the modified zones and determines the variation of the threshold pulse energy for dielectric modification as a function of the focusing depth.

When focusing occurs through a refractive index mismatched interface an aberration (spherical aberration) distorting the wavefront of the converging spherical wave is introduced. This aberration causes significant spreading of the intensity distribution along the beam propagation direction near the focus. To model the intensity distribution near the focus Török *et al.* [57] developed an elegant theory based on the vectorial generalization of the Debye integral for the case of the diffraction of a converging spherical wave propagating through a planar dielectric interface. This theory was subsequently extended to the case of a stratified medium [58]. In the Debye theory the electromagnetic field in the focal region is approximated as a superposition of plane waves with the propagation vectors $\boldsymbol{k}$ confined within the geometrical cone with it base determined by the lens aperture and the vertex coinciding with the focus (e.g., [59]). Other theoretical approaches addressing the same problem give very similar results [60].

Strictly speaking, the Török theory considers monochromatic radiation. In our simulations presented below (Fig. 3) the Debye integral was calculated only for the central wavelength (λ = 800 nm) of the fs laser radiation. The effect of spectral broadening on the focused intensity distribution becomes noticeable only for very short (<10 fs) laser pulses. However, even in this extreme case the changes touch only the fine structure of the intensity distribution, whereas the main features remain essentially intact [61, 62].

The focusing geometry is presented in Fig. 2 where a plane x-polarized monochromatic electromagnetic wave is first focused without aberrations (i.e., after the lens the wavefront is spherical) and then refracted at the planar dielectric interface separating media with the refractive indices n_1 and n_2 ($n_1 < n_2$). The propagation vector $\boldsymbol{k}$ of the plane wave as well as the optical axis of the focusing objective are assumed to be perpendicular to the interface. The origin of the coordinate system O is where the focus is located in the absence of the dielectric interface (i.e., $n_1 = n_2$). The interface intercepts the optical axis at a distance F from O. The position O', which denotes the position of the paraxial focus (i.e., the focus produced by the central zone of the focusing lens), is located at a distance $D \approx (n_2/n_1)F$ from the interface.

According to the Debye approximation, each point on the converging wave front is a source of plane waves which upon the refraction at the interface change their propagation directions. The electromagnetic field distribution in the medium described by n_2 can be found by integrating all the partial plane waves with the allowed propagation vectors $\boldsymbol{k}$.

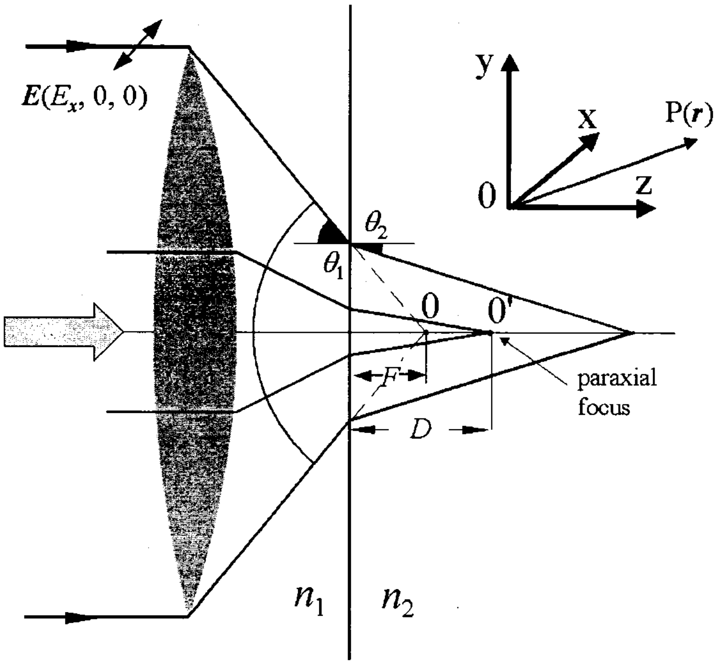

Fig. 2. Focusing of an electromagnetic wave through a planar dielectric interface.

Török *et al.* [57] showed that the electric field ***E***(***r***) at an observation point P(***r***) is given by

$$\boldsymbol{E}(\boldsymbol{r}) = \mathrm{C}\{[\mathrm{I}_0 + \cos(2\varphi)\mathrm{I}_2]\boldsymbol{e}_\mathrm{x} + \sin(2\varphi)\mathrm{I}_2\boldsymbol{e}_\mathrm{y} + 2i\cos(\varphi)\mathrm{I}_1\boldsymbol{e}_\mathrm{z}\} \quad , \tag{14}$$

where

$$\begin{aligned}
\mathrm{I}_0 &= \int_0^{\theta_{1\max}} \mathrm{A}(\theta_1)\sin(\theta_1)\left[\mathrm{t_s}(\theta_1) + \mathrm{t_p}(\theta_1)\cos(\theta_2)\right]\exp\{-i[k_0\boldsymbol{\Phi}(\theta_1) + k_2\cos(\theta_2)z]\}\,\mathbf{J}_0[k_1\sin(\theta_1)r]\,d\theta_1 \\
\mathrm{I}_1 &= \int_0^{\theta_{1\max}} \mathrm{A}(\theta_1)\sin(\theta_1)\left[\mathrm{t_p}(\theta_1)\sin(\theta_2)\right]\exp\{-i[k_0\boldsymbol{\Phi}(\theta_1) + k_2\cos(\theta_2)z]\}\,\mathbf{J}_1[k_1\sin(\theta_1)r]\,d\theta_1 \qquad \text{(14a)} \\
\mathrm{I}_2 &= \int_0^{\theta_{1\max}} \mathrm{A}(\theta_1)\sin(\theta_1)\left[\mathrm{t_s}(\theta_1) - \mathrm{t_p}(\theta_1)\cos(\theta_2)\right]\exp\{-i[k_0\boldsymbol{\Phi}(\theta_1) + k_2\cos(\theta_2)z]\}\,\mathbf{J}_2[k_1\sin(\theta_1)r]\,d\theta_1
\end{aligned}$$

r, *φ* and *z* are polar coordinates of the observation point P(***r***) and $\boldsymbol{e}_\mathrm{x}$, $\boldsymbol{e}_\mathrm{y}$ and $\boldsymbol{e}_\mathrm{z}$ are unit vectors in the x, y and z direction, respectively. Interestingly, the wave initially polarized along the x-direction after focusing and refraction produces the field distribution with non-zero E_y and E_z components. The explanation of the depolarizing effect can be found elsewhere (e.g., [62, 63]).[11] In (14a) $\theta_{1\max}$ is maximum angle between the marginal rays and the optical axis in the

---

[11] Boivin and Wolf [64] using the Debye approximation show that in the case of unaberrated focusing of a plane x-polaized monochromatic wave in air E_z is zero at the focus itself and in the azimuthal plane $\varphi = \pi/2$.

first medium, θ_1 and θ_2 are the angles of incidence and refraction at the interface, respectively (See Fig. 2), k_0, k_1 and k_2 are the wave numbers in vacuum, medium with n_1 and medium with n_2, respectively, $\mathbf{J}_0$, $\mathbf{J}_1$, and $\mathbf{J}_2$ are Bessel functions of the fist kind of the zero, first and second order, $A(\theta_1)$ is the apodization function (for an objective satisfying the Abbe sine condition $A(\theta_1) = \cos^{1/2}(\theta_1)$ [62]), t_p and t_s are the Fresnel transmission coefficients for an electromagnetic wave with the electric vector parallel and perpendicular to the plane of incidence [30], respectively, and, finally, $\mathbf{\Phi}(\theta_1)$ is the phase function given by

$$\mathbf{\Phi}(\theta_1) = -F[n_1\cos(\theta_1) - n_2\cos(\theta_2)]$$

In a general case, the intensity distribution $I(\boldsymbol{r})$ in the second medium, according to (14), becomes

$$I(\boldsymbol{r}) \sim \boldsymbol{E}^2(\boldsymbol{r}) = \mathrm{C}_1\left[\left|\mathrm{I}_0\right|^2 + 4\cos^2(\varphi)\left|\mathrm{I}_1\right|^2 + \left|\mathrm{I}_2\right|^2 + 2\cos(2\varphi)\mathrm{Re}(\mathrm{I}_0\,\mathrm{I}_2^*)\right], \tag{15}$$

where C_1 denotes a normalization constant. Taking into account that for $r = 0$ only $\mathbf{J}_0 \neq 0$ (viz., $\mathbf{J}_0(0) = 1$), for the axial intensity $I(\mathrm{z})$ expression (15) reduces to

$$I(\boldsymbol{r}) \sim \mathrm{C}_1\left|\mathrm{I}_0\right|^2 \tag{16}$$

Fig. 3 demonstrates two examples of calculated intensity distributions in the yz-section ($\varphi = \pi/2$) of the focal volume inside fused silica. Simulations were performed for x-polarized radiation at $\lambda = 800$ nm (central wavelength of a Ti:sapphire femtosecond laser system). The refractive index of fused silica at $\lambda = 800$ nm is $n_2 = 1.453$. Fig. 3(a) corresponds to focusing through an air-silica interface ($n_1 = 1$) 350 μm subsurface using an objective lens with the

---

The E_z-component has maxima along $\varphi = 0$ with the largest one occurring at approximately half a wavelength from the axis where it can be ≈ 28 % of the maximum value which the transverse component E_x attains at the focus (Boivin and Wolf performed their calculations for NA ≈ 0.7 corresponding to the maximum focusing angle of $\pi/4$). However, taking into account that the material modification process with focused fs pulses is determined by the light intensity $I \propto |E|^2$ (i.e., $|E_x|^2 \sim 10|E_z|^2$) and occurs mainly on the axis, the contribution of E_z compared with that originating from the dominant component E_x can be neglected at intensities close to the material modification threshold intensity I_{th}. In focusing through a dielectric interface it can be shown that $\mathrm{I}_0 > \mathrm{I}_1 > \mathrm{I}_2$ [62] and the contribution of the depolarizing E_z and E_y-components which are determined by I_1 and I_2, respectively, is also small and can be neglected unless the modification is performed at the high intensities of $I \sim 10\, I_{\mathrm{th}}$. During the experiments presented in ARTICLE III we operated at low intensities close to I_{th} when the depolarization is expected to be negligibly small.

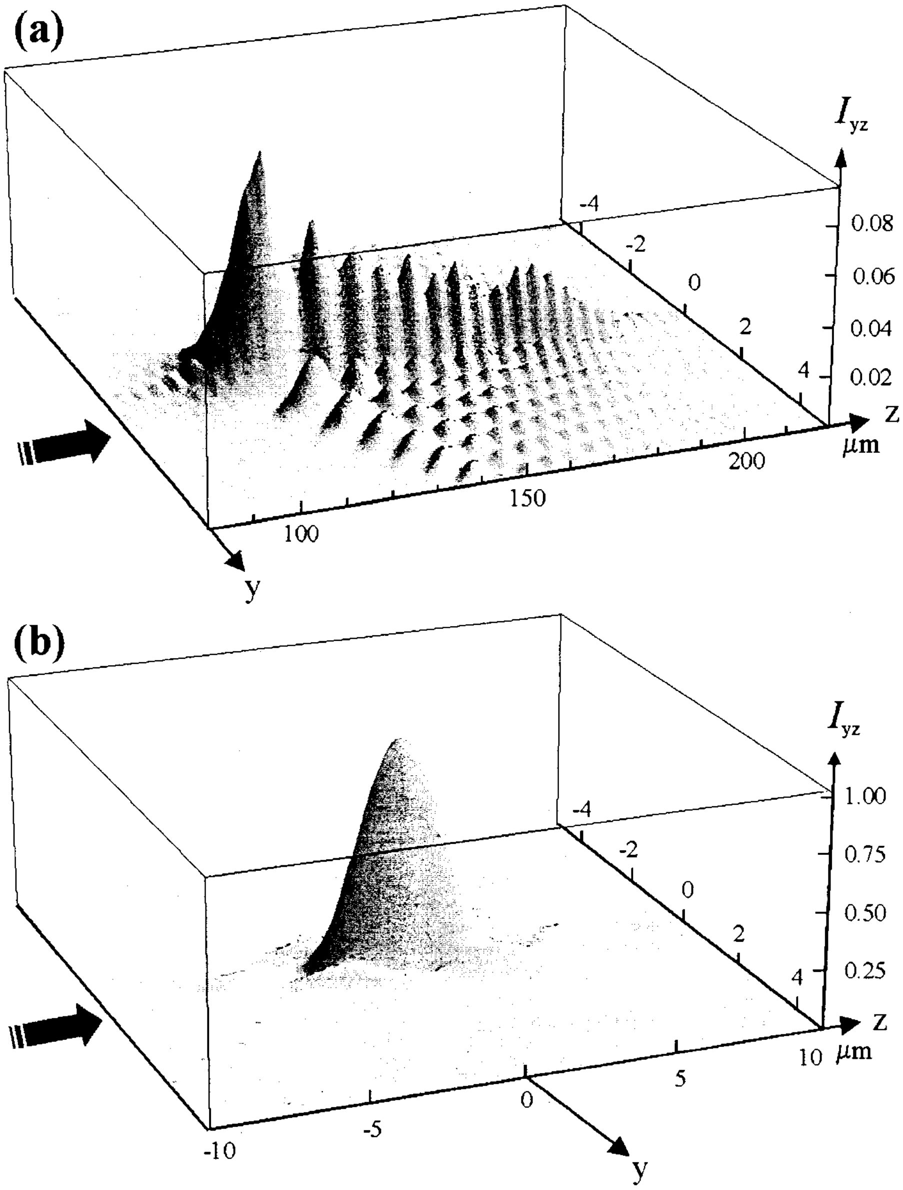

Fig.3. Normalized calculated intensity distributions in the focal volume inside a fused silica sample (a) affected by spherical aberration caused by focusing 350 µm subsurface through the air-silica interface and (b) without aberrations. In both cases simulations were done for a NA = 0.75 aberration-free microscope objective. The arrows indicate the light propagation direction. The shown intensity distributions are symmetric with respect the optical axis coinciding with the z-axis.

numerical aperture NA = 0.75.[12] In Fig. 3(b) the intensity distribution is modeled under the assumption that the wave front in the second medium is spherical, i.e., it corresponds to the perfect compensation of the interface induced aberration. In both cases the rays in the second

---

[12] Using our definitions, NA = $\sin(\theta_{1\max})$, where $\theta_{1\max}$ is the upper integration limit in 14(a).

medium are confined within the same cone of angles given by arcsin($0.75/n_2$). The focusing depth is identified with the paraxial focus in the second medium D (See Fig. 2), which also approximately gives the position of the main maximum with respect to the interface [65]. As D increases, the following trends in the axial intensity distributions are observed: i) a dramatic drop in the magnitude of the main maximum, ii) relative growth of the secondary maxima with a gradual increase of the separation between the main and second maxima, and iii) spreading of the distribution along the beam propagation over distances exceeding many times the unaberrated intensity distribution approximated by $4n_2\lambda/\mathrm{NA}^2$ (base or full width)[13] [30], where λ is the wavelength in vacuum and NA denotes the numerical aperture of a dry objective. In ARTICLE III we calculate the drop in the peak intensity with depth for objectives with different NA's and show that focusing pulses with high NA optics is restricted to a few tens of microns under the surface unless the laser power is raised dramatically in compensation. In Fig. 3 the severity of the spatial distortion is apparent even for a moderate writing depth of 350 μm, where the intensity distribution spreads from the unaberrated value of ≈ 8.5 μm (Fig. 3(a)) to more than 110 μm (Fig. 3(b)).

In focusing fs pulses with high-NA objectives (NA > 0.5) spherical aberration plays a double role. It dramatically reduces the peak intensity in the pulse and therefore weakens the undesirable, difficult to control nonlinear effects. On the other hand, spherical aberration severely distorts the intensity distribution in the focus causing the formation of multiple modified regions, which coincide with the intensity maxima along the pulse propagation direction (See Fig. 3(a)). We also note that it is difficult to arrest this process because even if dense electron plasma is formed near the first intensity maximum it cannot efficiently absorb the pulse energy moved away from the optical axis and thus prevent multiple-spot irradiation in the focal region. In ARTICLE III we demonstrate the formation of multiple modified regions in the aberrated laser focus and also show how to avoid this effect.

---

[13] The intensity distribution along the z-axis is approximated by a function $[\sin(\zeta)/\zeta]^2$, where $\zeta = \frac{\pi \sin^2(\theta_{\max})}{2\lambda_m} z$, and $\theta_{\max}$ and λ_m denote respectively the maximum angle between the marginal rays and the optical axis and the wavelength in the light propagation medium (i.e., $\lambda_m = \lambda/n_2$, where n_2 is the refractive index of the medium and λ is the wavelength in vacuum). The first zero of the intensity on the axis is determined by $\zeta = \pm\,\pi$. Using this condition, the base (or full) width of the axial intensity distribution can be written as $\Delta_{z0} = \frac{4\lambda_m}{\sin^2(\theta_{\max})}$.

Although accurate modeling of the intensity distribution in the second medium can be achieved only by using the rigorous diffraction theory, the basic effects of focusing through a dielectric interface can be predicted by geometrical optics. This approach allows one to assess the magnitude of the longitudinal intensity spreading without performing laborious numerical simulations. Fig. 2 shows that the marginal rays intercept the optical axis further from the interface than the paraxial rays, which means that the interface introduces spherical aberration. Using the geometrical optics approach (See Appendix A), the magnitude of this longitudinal spreading Δ_z caused by spherical aberration is given by a simple expression

$$\Delta_z = D\left\{\sqrt{\frac{1-\left[\sin(\theta_{1\max})n_1/n_2\right]^2}{1-\sin^2(\theta_{1\max})}}-1\right\} = D\left[\sqrt{\frac{1-(\mathrm{NA}/n_2)^2}{1-(\mathrm{NA}/n_1)^2}}-1\right], \tag{17}$$

where NA = $n_1\sin(\theta_{\max})$. For $n_2 = 1.453$, $n_1 = 1$, NA = 0.75, and $D = 350$ μm formula (17) yields $\Delta_z \approx 110$ μm, which is in a very good agreement with the corresponding value of 108 μm given by the modeling based on the diffraction theory (Fig. 3(a)).

Spherical aberration introduced by the interface also changes the temporal behavior of a pulse in the focal region. The electromagnetic disturbance associated with a pulse first reaches the paraxial focus and after a time delay ΔT approximated by (See Appendix A)

$$\Delta T = \frac{D}{c}\frac{n_2^2-n_1^2}{n_2}\left[\frac{1}{\cos(\theta_{1\max})}-1\right] = \frac{D}{c}\frac{n_2^2-n_1^2}{n_2}\left\{\frac{1}{\left[1-(\mathrm{NA}/n_1)^2\right]^{1/2}}-1\right\} \tag{18}$$

it arrives at the marginal focus. This delay, however, is not a temporal pulse broadening *per se* as the pulse arrival at different points in space is considered. Formula (18) after substitution of the numbers that were used earlier to estimate the longitudinal spreading Δ_z yields a very significant ΔT of 450 fs.

Discussion

As it was mentioned earlier, fs laser modification of transparent dielectric materials is a highly nonlinear process driven by light absorption and ionization of the medium. The key parameter determining the probability and localization of ionization and the modification itself is the laser light intensity. Multiphoton ionization together with tunneling ionization provide seed electrons in the conduction band and then avalanche ionization accelerated by collision- and hole-assisted excitation processes exponentially increases the electron population. The produced electron plasma strongly absorbs electromagnetic radiation and the pulse energy is dissipated in the plasma formation region. Although the relative contributions of photoionization and avalanche ionization to the electron plasma formation vary with the pulse duration, it is important that the seed electrons are mainly provided by photoionization processes rather than by excitation from impurities and defects, which is typical of long, low intensity laser pulses. This makes fs laser dielectric modifications a deterministic, self-initiated process with the modification threshold determined by the bandgap energy of the material. The intensity required to ionize (and modify) the medium with short pulses is achieved at low pulse energies and therefore the amount of energy that is deposited into the medium and eventually converted into heat is also low. The heat affected zone where cracks and other thermally induced defects can form is therefore dramatically reduced, so that the extents of modification can be localized on a sub-micrometer scale. The deterministic nature of, and minimum collateral damage associated with fs radiation-induced modification make fs lasers a unique tool for micromachining.

Previous studies have shown that modification produced in transparent media strongly depends on whether the focusing of femtosecond pulses is achieved using high- or low-NA objectives (e.g., [28] and references therein). To achieve the material modification threshold intensity in a weak focusing geometry the peak pulse power should be high and nonlinear effects can dominate the laser pulse propagation. A dynamic balance between self-focusing and photoionization usually leads to a filamentary (self-trapped) propagation accompanied with a significant spectral broadening of the pulse (white light-continuum generation). In this regime highly elongated modification which can stretch many hundreds of microns along the pulse propagation direction is produced [66, 67].

The majority of applications, however, require a localization of the modified zones on a micrometer and sub-micrometer scale (e.g., optical data storage) and the ability to arrange them in 3-D rather than along one direction. This can be achieved using tightly focused pulses at low peak powers (i.e., below P_{cr}) when self-focusing effects are small or can be neglected and the dimensions of the modified regions are related to the size of the focal volume given by diffraction theory. As we already mentioned, the nonlinear dependence of the multi-photon ionization rate on the intensity promotes the confinement of the electron plasma formation region and the resultant modification to sub-diffraction-limited volumes. Although high-NA focusing theoretically provides such a capability, in practice other aspects of the pulse focusing become critical. Even if the focusing objective is perfect (corrected for all types of optical aberrations) and the temporal pulse broadening in it (which can be significant) is totally compensated by pre-chirping the pulse in the laser system, spherical aberration introduced by the sample-surrounding medium interface will strongly affect the spatial and temporal characteristics of the pulse in the medium. The axial spreading of the intensity distribution, which increases with increasing the focusing depth and the refractive index mismatch at the interface, results in the formation of multiple, axially stretched modified regions. Although writing with conventional dry high NA optics at depths exceeding several hundred microns becomes impractical due to the mentioned severe drop in the peak intensity and intensity spreading, we show in ARTICLE III that specially designed objectives can be successfully used to write diffraction limited structures deep into the material.

Section 2. Study of femtosecond laser-induced modification in glass

Different regimes of fs radiation-induced modification in fused silica glass

As it was mentioned earlier, the use of fs-lasers radiation to modify transparent dielectrics (glasses) is based on its ability to induce localized changes to the refractive index of the medium in 3-D which allows one to fabricate various passive microphotonic components such as waveguides [2], couplers [3], high-density optical storage [4], gratings [5], and fiber Bragg gratings [6] as well as active devices such as laser amplifiers [7, 8]. It has also been demonstrated that fs-laser modified regions can etch selectively with respect to the unmodified surrounding material and thus form nanostructures and microfluidic channels [12, 13].

Although various potential applications of fs-laser induced modification have been demonstrated and discussed in numerous reports, much work has yet to be done to understand basic mechanisms responsible for the photo-induced physical and chemical transformations occurring in bulk material at the atomic level. The understanding of possible origins of the fs modification is complicated by the fact that the properties and morphology of the modified regions are very strongly affected by both the material composition and the irradiation conditions. The work presented in this thesis is primarily on the ultra-high spatial resolution imaging and characterization of structural changes occurring in glassy media during fs irradiation rather than on the study of mechanisms leading to these changes. Since this thesis concentrates on the study and applications of the modification in fused silica, the discussion of the characterization techniques as well as possible mechanisms underlying fs laser-induced physicochemical changes is mainly dedicated to this material.

Previous research has shown that three distinct types of modification can be identified for fused silica depending on the laser intensity: i) homogeneous modification associated with a smooth positive refractive index change (e.g., ‘type I damage’ in Ref. [15]), ii) sub-wavelength nanogratings (linear laser light polarization) [68] and disordered nanostructures (circular polarization) (ARTICLE VI), and iii) disruptive modification (voids, microexplosions) at high light intensities [4, 17] and ARTICLE IV. The intensity threshold for each type of modification also strongly depends on the combination of the pulse duration and pulse energy (ARTICLE IV) as well as on the focusing geometry (the NA of the focusing optics and focusing depth). For example, for a low-NA focusing (NA = 0.2) we did not observe the regime of nanograting formation within the pulse energy-pulse duration parameter space that we used in ARTICLE IV with a 0.65 NA focusing objective. This argument makes the quantitative analysis meaningful only if certain writing parameters are fixed (e.g., in ARTICLE IV the NA and focusing depth were kept constant). Each type of modification will be considered separately.

RegimeI:Homogeneous modification. This type of modification in fused silica is associated with a smooth positive refractive index change and finds its application in the fabrication of waveguiding and grating components. The homogeneous index change (typically $\Delta n \sim 5 \times 10^{-3}$), which can be achieved with high-NA focusing geometry (NA > 0.4) only within a narrow pulse energy-pulse duration operating window close to the material modification threshold (See ARTICLE IV), is necessary to minimize scattering losses in the waveguides.

Several mechanisms have been proposed to account for the observed small index change. Even at low laser intensities due to the highly localized heating of the medium the temperature can reach the glass-liquid transition point. Rapid cooling and resolidification of the molten material occurring within a few microseconds after the pulse will lead to an increase of the fictive temperature T_f in the modified region compared to the surrounding unmodified material [70].[14] For silica glass in the region of 1000-1500°C an increase of T_f leads to an increase in the density and the refractive index since these parameters are linearly related to each other. It has also been found that higher T_f lead to smaller Si-O-Si bond angles and strained Si-O bonds which are more chemically reactive than those inside the unstrained unmodified material. In between 1500 and 2000°C the density drops as T_f grows, however this drop occurs slower than the increase observed at lower fictive temperatures and the density over the whole temperature range of 1000-2000°C appears to be higher than below 1000°C [71]. Raman spectroscopy of fs-laser modified silica indicates an increase of

---

[14] The structure which is frozen in the glass during the liquid-solid transformation persists at all lower temperatures as the viscosity of the liquid rapidly increases with decreasing temperature, and atomic rearrangement slows down dramatically. Thus, a glass has a configurational or fictive temperature T_f that may differ from its actual temperature. The fictive temperature is the temperature at which the glass structure would be in the equilibrium if suddenly brought to that temperature from its given state. It describes the structure of a glass as it relates to the cooling rate (thermal history). A fast-cooled (quenched) glass has a higher fictive temperature than a slowly cooled glass. In industry, in order to avoid the generation of mechanical stress in glass it is cooled down from the melt slowly, i.e. the fictive temperature of a silica glass sample is expected to be lower than that inside the melted and quenched fs-laser irradiated regions.

3- and 4-fold ring structures[15] indicative of an overall decrease in the bond angle and densification of the material [70].

The refractive index change can also be caused by the formation of color centers (defects consisting of interstitials and vacancies) in the irradiated regions inside initially perfect dielectrics. The presence of these light absorbing species in a dielectric is equivalent to the introduction of the imaginary part into the refractive index. The real and imaginary parts of the complex refractive index are related through the Kramers-Krönig relations allowing one to determine the full complex refractive index as a function of wavelength from an absorption spectrum of the material. Because of the high electron density produced by the intense fs-laser radiation there can be sufficient number of defects produced to change the real part of the refractive index via the Kramers-Krönig mechanism. Electron spin resonance and photoluminescence data obtained in modified fused silica and borosilicate glasses showed an increase in the concentration of the E' centers (paramagnetic positively charged oxygen vacancies: $\equiv\mathrm{Si}\bullet\mathrm{Si}\equiv$, absorption band at 5.8 eV; or neutral dangling Si bonds, $\equiv\mathrm{Si}\bullet$), non-bridging oxygen hole centers (NBOHC: dangling oxygen bonds, $\equiv\mathrm{S}{-}\mathrm{O}\bullet$, absorption band at 4.6 eV), oxygen deficient centers (ODC: neutral oxygen vacancies, $\equiv\mathrm{Si}{-}\mathrm{Si}\equiv$, absorption band at 5.1 eV), peroxy radicals (POR: $\equiv\mathrm{S}{-}\mathrm{O}{-}\mathrm{O}\bullet$, absorption bands at 2.3 and 4.8 eV), and other unidentified defects with broad absorption bands [5, 74]. Color center formation occurs at intensities as low as $I \sim 10^{12}$ W/cm^2 and has no sharp onset intensity. This phenomenon has been observed in optical borosilicate crown glasses, high purity alkali silicate glasses and in fused silica [75, 76]. Annealing of the material above ~150°C causes the color centers to disappear, whereas the induced refractive index change shows a significant decrease only at much higher temperatures of ~400-600°C depending on the material. As the annealing temperature is increased the color-center signal also decreases faster than the induced refractive index change, which makes it unlikely that the index change is solely due to the color-center formation [76].

---

[15] Various theoretical models supported by experimental techniques (X-ray diffraction, nuclear magnetic resonance, infrared, and Raman spectroscopy) suggest that the structure of a-SiO_2 (amorphous or fused silica) is a network of SiO_4 tetrahedra containing irregular rings of order m, where m is the number of Si atoms in the ring [72]. The m-order ring also includes m O atoms. The most common ring in a-SiO_2 is with $m = 6$. The Si-O-Si bond angles have wide distribution with a peak at most probable value of 152°, whereas the O-Si-O angle is more narrowly distributed around the tetrahedral value of $\approx 109.5°$ [73].

There is also a possibility that, by analogy with ultraviolet (UV) light-induced modification [77], a non-thermal mechanism is responsible for the structural changes in fused silica (and other glasses) caused by fs irradiation. It was found, that fused silica undergoes densification or compaction after being exposed to UV radiation, which at high irradiation doses can lead to a significant increase in the refractive index. The densification in this case is attributed to the reduction in the average *m*-number occurring by directly breaking and rearranging the bonds. The process of compaction cannot go beyond the formation of 2-membered rings [72].

The presence of network modifiers in multicomponent glasses makes the understanding of the modification process even more difficult as the migration of network modifiers leading to a variation in the chemical composition across the fs-irradiated region can also lead to the changes in the refractive index.

Regime II: Sub-wavelength nanogratings and disordered nanostructures. Previous research has shown that in fused silica above a certain laser intensity level in the focus a second type of modification consisting of birefringent ('type II damage') [15], anisotropic scattering [69] zones is produced. It has also been shown that this type of modification is still present after annealing at high temperatures > 1100°C [78] as compared to ~ 600-900°C sufficient to erase the homogeneous modification that was described earlier. The formation of modulation of the refractive index with a sub-wavelength periodicity has been suggested as an explanation to the observed anisotropy [69]. The existence of periodic structures, further referred to as nanogratings, which are always oriented perpendicular to the laser polarization, was first confirmed by Shimotsuma *et al.* [68] in a fixed focus, when a fused silica sample was irradiated by 150 fs, 800 nm laser pulses 100 μm subsurface. The nanograting lines were characterized using backscattering SEM and Auger electron spectroscopy in 2-D after polishing down the sample to the level of the modified zones. In an independent effort to study this type of modification at a nanometer scale, we have recently performed a complete 3-D study of the modified regions produced under different irradiation conditions by scanning the laser focus through the sample and found that these polarization-dependent nanograting lines are in fact nanoplanes and maintain their periodicity over the entire writing range (ARTICLES IV, V, VI and Ref. [79]). The very fact that grating-like structures can be optically formed inside the diffraction limited focal volume requires a major investigation of both the basic concepts of fs laser dielectric modification and possible applications of the technique. The study of this type of modification constitutes the core of this thesis and therefore will be presented in more detail than other types of modification.

To explain the formation of self-organized nanogratings, Shimotsuma *et al.* proposed a model based on the interference between the electric field of an electron plasma wave inside the ionized volume and the incident light field. This interference imposes a periodic modulation on the electron plasma density causing a corresponding periodic modification in the material. The electron plasma wave is a longitudinal wave and for a 1-D plasma, in the presence of the driving field, it is launched at an angle to the direction of propagation of light. For coupling between the plasma wave and the incident light field, momentum has to be conserved. The momentum of the plasma wave, and consequently the grating period, depend on the density N_e and temperature T_e of the excited electrons. Since both these parameters are functions of the energy deposited in the focal volume, Shimotsuma *et al.* [68] predict that the grating period changes with the pulse energy and number of shots. Although the interference-based approach is intuitive in explaining the formation of regular structures, this model uses unrealistically high plasma temperatures (> 10^7K or 1300 eV) and densities (> 95% of the critical density N_{cr}) to explain the experimental observations. Kilovolt electron energies are usually associated with X-ray radiation from surface plasmas generated by 10^{18} W/cm^2 laser pulses, in contrast to the intensities of under 10^{14} W/cm^2 operative in dielectric modification. The near-critical N_e assumed by Shimotsuma *et al.* [68] is very restrictive since light will not penetrate the plasma once the critical density is exceeded. On the other hand, according to Shimotsuma *et al.* [68], lower N_e will lead to even higher T_e to reproduce the experimentally observed spacing. Further, knowing the volume of the modified region from our 3-D measurements we estimate that a minimum E_p of 10 μJ is required to achieve electron temperatures of $\approx 10^7$ K at near the critical plasma density of $\approx 2 \times 10^{21}$ cm^{-3}. This simple energy balance assumes that all of the laser pulse energy is deposited in the modified zone and in the electron plasma. In contrast, we have found that the threshold for nanostructure formation is typically only 100-200 nJ. It also is not obvious from the interference model how the order is maintained when the focus is scanned along the sample. On the contrary, one would expect that the structures formed due to interference between light and plasma waves are washed out since plasma waves are bound in each focal spot and are independent from spot to spot. However, the long-range order apparent in our results (ARTICLES IV, V, VI and Ref. [79]) implies that the structures formed in one focal spot have a control over the modification induced in the neighboring spot.

We have developed an alternative model based on nanoplasmonic theory to account for the observed trends in the nanograting formation [79]. According to our model, the nanograting evolution is a three-step process, which takes place over many laser shots, including i) inhomogeneous dielectric breakdown and formation of nanoplasmas, ii) modification of the material on the nanoscale to create a 'memory' of previous nanoplasma formation and growth of the modified regions into nanoplanes, and iii) self-organization of the nanoplanes.

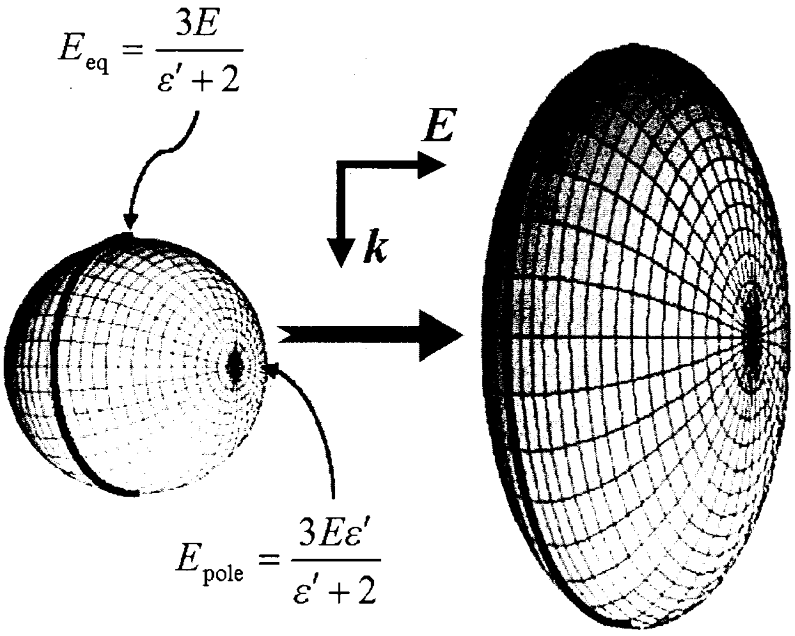

Fig. 4. A schematic diagram adopted from Ref. [79] showing how the local fields around a nanoplasma promote its growth into a nanoplane. ***k*** denotes the direction of propagation of the laser beam and ***E*** is the electric field in the medium associated with the fs laser pulse. E_{eq} and E_{pole} are the local fields found at the equator and poles of the sphere, respectively. ε' is the ratio of the permittivity of the nanoplasma sphere to the surrounding dielectric medium. When $\varepsilon' < 1$ (i.e., when the plasma density is less than the critical density) field enhancement occurs around the equator (shown as a strip) and a spherical nanoplasma evolves into a nanoplane.

Dielectric breakdown can be inhomogeneous for several reasons. The high non-linearity of the process may result in instabilities that lead to an intrinsic inhomogeneity, color centers and defects may act as nucleation centers and hole-enhanced ionization may also play a role [48]. All of the above can lead to the production of localized nanoplasmas in the material. The nanoplasmas are underdense during most of the time of their interaction with the incident laser pulse. The electric field inside an underdense plasma exceeds the laser field, which further enhances the local nature of the breakdown. The boundary conditions require that the electric field around the equator of an underdense spherical nanoplasma with the polar axis aligned along the laser polarization is enhanced as compared with the pole regions where the electric field is suppressed (Fig. 4). Thus, underdense nanoplasmas must grow into sheets oriented perpendicular to the laser polarization. Even when the plasma density increases, since the nanoplasmas will have a density gradient, their outer boundary remains always underdense, ensuring that they grow into nanoplanes.

The process of nanoplane growth occurs over many laser shots leading to alteration of the material. This implies a memory of the cumulative effect of previous shots that we relate to a lowering of the multiphoton ionization threshold in material that has been previously ionized. In the early stages of material modification these changes might be the result of the creation of defects. In the later stages the material structure itself can be significantly altered on the nanoscale and may even become a planar nanocrack (i.e., a very narrow ~10 nm wide slot). The ionization and recombination processes are expected to be especially efficient at a nanocrack [80].

The self-organization of the nanoplasmas is postulated to be a result of their semi-metallic properties (i.e., obtained in the later stages of nanoplasma development when the plasma electron density approaches the critical density) which affect the field propagation in a way similar to planar metallic waveguides. Growth of the planes will be favored if they support modes whose field distribution reinforces their own growth or where the field is enhanced by a suitably placed neighbor. The spacing is solely determined by the mode structure and therefore scales linearly with the wavelength independent of the laser pulse energy, as indeed was confirmed in our experiments which showed that the average period of the nanogratings produced at λ = 800 nm is two times larger than in the case when the wavelength of the writing laser beam was decreased to λ = 400 nm by frequency doubling

[79] (Shimotsuma *et al.* predict a non-linear wavelength dependence [68]). For the lowest order optical mode structure, the nanoplasmonics model predicts a minimum nanograting period of $\lambda/2n$, where n is the index of refraction of the medium. The bulk value of n (i.e., for fused silica $n = 1.453$ at $\lambda = 800$ nm) can be used if plasma formation and material modification predominately occurs at the transient quasi-metallic grating planes. Our model prediction for the minimum nanoplane spacing in fused silica is therefore 275 nm, which is in reasonable agreement with an average value for the experimentally observed spacing of 250 ± 20 nm (measured in the xy-plane using thousands of grating planes).

With a moving focal volume and laser electric field $\boldsymbol{E}$ parallel to the writing direction $\boldsymbol{S}$, the mode structure in the previous spot determines where the nanoplanes would grow in the newly exposed region. In the case when $\boldsymbol{E}$ is perpendicular to $\boldsymbol{S}$, order is imposed on new material via the field distribution at the boundaries of the nanoplanes. Thus self-ordered periodic nanoplanes can be produced when the sample is moved. In the case of circular polarization we expect the nanoplasmas to develop into prolate ellipsoids with their long axis aligned with the beam propagation vector $\boldsymbol{k}$. This is because the field is only continually enhanced at boundary points close to this axis under circular polarization. Our experimental results largely show disordered structures consistent with there being no mechanism to impose long-range order.

Regime III: Disruptive modification (microvoids/microexplosions in bulk material). When high energy femtosecond laser pulses are focused with very high-NA (liquid immersion focusing, NA = 1.2-1.4) objectives the radiation absorption is confined to a volume with dimensions as small as 1 μm^3 [17]. In this regime the fs radiation propagates inside the material at intensities $I > 10^{14}$ W/cm^2. The material within a tiny interaction region is almost instantaneously (in a few ps) heated up to temperatures ~10^5K and the pressure caused by the sharp rise in temperature in a constant volume can reach enormous numbers on the order of hundreds of GPa. Under such conditions the very hot electron-ion plasma explosively expands out of the interaction region into the surrounding cold medium, which leads to the formation of a voxel (volume element) of rarefied material (or a void in the extreme case) enveloped with a shell of densified material [17]. The sub-micrometer size combined with a high refractive index contrast of microexplosions make this type of modification very attractive for high density 3-D optical data storage. Although the regime of microexplosions can also be achieved using lower NA's at increased laser powers, the resulting larger extent of the modification will compromise its use in such a demanding application. In ARTICLES IV and VI we demonstrate that relatively long pulses ($\tau_p \geq 200$ fs) at pulse energies of ~ 500 nJ focused with a NA = 0.65 objective also produce extensive disruptive modification (microvoids) in the top portion of the modified regions (Regime III in ARTICLE IV). In the Conclusion we discuss the importance of this type of modification for microfluidics.

Diagnostics techniques

Numerous techniques have been used by researchers to characterize fs radiation induced modification in optical glasses. Of all techniques traditional optical microscopy is the easiest to implement and, consequentially, is the most commonly used. This inherently diffraction limited technique, however, mainly visualizes the modified regions with a spatial resolution of ≥ 300 nm and provides only limited information on the morphological changes occurring in the material. X-ray diffraction, nuclear magnetic resonance, electron spin resonance, Raman, infrared and fluorescence spectroscopy do reveal structural changes in the material at the atomic level but due to a poor spatial resolution this information is essentially averaged over many modified regions. Ultra-high spatial resolution (~10 nm) techniques, used to study sub-micrometer features of the modification morphology, include AFM, SEM (secondary and backscattered electron imaging), Auger electron spectroscopy on cleaved or polished samples and AFM or SEM on chemically pre-etched surfaces. Among these techniques backscattered electron imaging and Auger spectroscopy are also sensitive to the chemical composition or density of the material on the surface.

In this thesis we study the modification in various glasses using a microreflection optical technique, AFM and SEM on polished and etched surfaces and SEM on cleaved surfaces. Whereas AFM and SEM studies of fs laser modified regions on cleaved and polished surfaces have been performed by other authors, to the best of our knowledge, we are the first to apply the technique of weak selective chemical etching followed by AFM to characterize fs radiation-induced glass modification. We are also unaware of any reports related to the use of a microreflection technique in the fs modification domain. We first reported on the use of both the etching-AFM and microreflection based techniques for fs modification diagnostics in Ref. [81] which can be found in Appendix B of the thesis. A detailed description of sample preparation and implementation of the etching-AFM/SEM technique is provided in ARTICLE VI. To characterize the electromagnetic field distribution (mode structure) at the output of fs laser-written waveguides we used near-field scanning optical microscopy (NSOM) in the light collection mode with custom made chemically etched metallized probes [82, 83]. Three of the mentioned techniques, viz. etching-AFM, microreflection and NSOM, were implemented using a scanning probe microscope Digital Instruments Inc. Dimension^{TM} 3000. In order to achieve full flexibility in performing measurements, the SPM head of the microscope containing the piezoelectric scanner has been modified to allow operation in any orientation (typically horizontal) as opposed to the original fixed vertical deployment [84].

Technique of selective chemical etching and AFM/SEM. In 1994 Zhong and Innis showed that the technique of selective chemical etching followed by AFM can be used to deduce refractive index profiles in optical fibers [85]. They demonstrated that in a water solution of HF the doped core of a germanosilicate fiber etches selectively relative to the cladding and that the etch rate of the core linearly depends on the dopant concentration. Since the refractive index of the core also linearly depends on the dopant concentration, by measuring the topographic profile of the etched depression in the core region it is possible to deduce the relative core-cladding refractive index change. AFM allows one to measure topography with a 10-20 nm lateral resolution and a sub-nanometer height resolution and therefore very accurately map refractive index profiles of fibers.

The potential of the technique of selective chemical etching followed by AFM to study fs radiation-induced modification in glasses is also based on a difference in chemical properties between the modified and unmodified material. When an irradiated sample is immersed into an aqueous solution of hydrofluoric acid, the modified regions etch at a different rate than the unmodified material. This translates the structural changes occurring in the material into a topographic profile which can be measured using AFM or SEM with a nanometer resolution. There is another very important aspect of acid etching in revealing the modification morphology. During sample preparation, which usually includes cutting and polishing, the sample surface becomes covered with a very thin (~10 nm) polishing-induced layer of processed material which masks the fine features, e.g., nanogratings, inside the modified regions. Without removing this layer via weak etching neither AFM nor SEM would provide any meaningful information on the morphology. The AFM and SEM techniques are complimentary. SEM increases contrast of abrupt deep topographic changes but is almost insensitive to smooth relief on a nanometer scale which is easily mapped by AFM. On the other hand, analysis of AFM images becomes difficult due to loss of contrast when smooth topographic background masks very narrow and deep (> 50 nm) features (e.g., polarization-dependent periodic nanostructures studied in ARTICLES IV, V and VI) whose actual depth is underestimated in this AFM-probe limited regime.

In fused silica the decrease in the bond angles inside the modification can make the oxygen atoms more chemically active in reactions with acids due to the deformation of their valence electron configuration. In the regime of smooth modification in fused silica the etch rate of modified regions is found to be faster than that of the surrounding material. The etch rate in this glass is also approximately in a linear relationship with the induced positive refractive index change (Appendix B). The linear dependence between etch depth and index may, however, applies only to fused silica. The refractive index modification exhibits a strong dependence on the glass composition and can be positive, negative or nonuniform while the etch rate in all those cases is faster in the modified regions than in the unmodified material (See ARTICLE II). Even though there is generally no correlation between the index change and the etch rate in the modified regions, the technique very accurately maps their morphology, shape and size, which can provide crucial information regarding potential applications of the material, as reported in ARTICLES IV, V and VI.

Microreflection technique (reflection refractometry). The development of high spatial resolution refractive index profilometry is tightly linked with the use of optical fibers in telecommunications. Among several optical techniques developed to map the refractive index across optical fibers the refracted near-field method (RNF) is a unanimous leader as it can detect index variations on the order of $\Delta n \sim 10^{-5}$-10^{-4} and also provides a high spatial lateral resolution of $\approx 1.22\lambda/2\mathrm{NA}$ determined by the diffraction limit of light [86]. The RNF technique has also been applied for studies of the fs radiation-induced refractive index changes in various glasses (e.g., Ref. [76] and ARTICLE II). There is, however, another high resolution technique based on microreflection [87] which is much easier to implement in the case of relatively large and irregular glass samples (cubes, slabs, cylinders) typically used in fs modification experiments. In both RNF and microreflection techniques the fs-modified regions are illuminated by a focused probe laser beam and the difference in the techniques is simply determined by the collection mode of the signal originating from the refractive index inhomogeneity associated with the modification: in RNF geometry the refracted signal is analyzed, whereas the microreflection uses the reflected component of the probing light. The main argument against using the microreflection geometry in high spatial resolution studies is related to the theoretical model of the normal incidence approximation [87]. This approximation is based on the assumption that the sample is illuminated at a normal incidence with a probe laser beam (i.e., focusing is achieved with low-NA objectives) and therefore a simple expression for the surface reflectivity $\mathscr{R} = [(n-1)/(n+1)]^2$can be used [30]. In this expression n denotes the refractive index of the sample probed with the laser beam and the refractive index of the ambient air is assumed to be 1. However, in order to increase spatial resolution the laser beam has to be focused tightly with high-NA objectives, which implies the use of rays with a large spread of angles of incidence to probe the refractive index changes. Since the reflection coefficients given by the Fresnel formulae show angular dependence [30], which becomes especially pronounced for large angles of incidence, the analysis based on the normal incidence approximation becomes inaccurate and the theoretical model underlying the microreflection technique should be modified to address this issue [88]. Below we will show that i) the normal incidence approximation in fact gives accurate results for NA's up to 0.6 and ii) in general, a correction factor can be introduced to account for the contribution of the angled rays.

A schematic of the basic microreflection setup used in our experiments is shown in Fig. 5. The sample is mounted on a high-accuracy xyz-piezo scanner which moves under the fixed focus of the probe laser beam. The optical axis of the focusing objective is normal to the sample surface. The reflected signal $R(x,y)$ ($\approx 4\%$ of the incident light) is redirected with a beam splitter (BS) towards the detector and recorded as function of the sample position (x,y), as described in ARTICLE I. The refractive index of the unmodified material n_0 is assumed to be known and the refractive index change caused by fs irradiation is denoted by Δn. The diagram also shows the presence of a polishing-induced surface layer with the refractive index of $n_0+\delta n$ and thickness of h. The effects of this layer on the reflected signal will be considered later. For microreflection it is also imperative to have excellent index

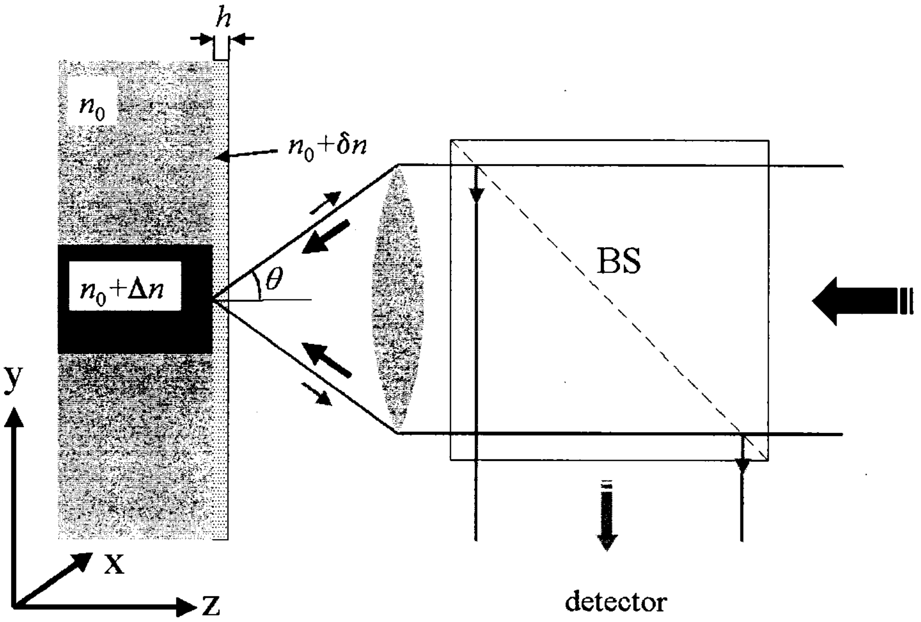

Fig. 5. Microreflection experimental setup showing presence of a polishing-induced surface layer.

matching at the exit surface of the waveguide since any reflected signal from this surface will be guided back to the front surface where it can compete with the signal reflected from the front surface. In our experiments the back surfaces of the samples are roughened and terminated in a specialty epoxy with the refractive index very close (to within 0.0005) to that of fused silica at the probe laser wavelength.

The reflected power from the surface of the sample is directly related to the refractive index of the sample. The microreflection technique allows one to measure the reference reflected signal R_0 from the unmodified material with n_0 and a change in the reflected signal ΔR from R_0 caused by the induced refractive index variation Δn. The following points should also be emphasized: i) focusing with any NA can be used for the measurements depending on the required spatial resolution, however both measured reflected signals R_0 and ΔR depend on the used NA and ii) the deduced magnitude Δn of the refractive index variation depends on the approximation/model used to interpret the microreflection data, i.e., the actually measured R_0 and ΔR.

The model used in the normal incidence approximation [87] establishes a simple relationship between the reference reflected signal R_0, a change in the reflected signal ΔR, and a small $\Delta n \ll n_0$ causing this change

$$\Delta n(\mathrm{x},\mathrm{y}) \approx \left[\frac{n_0^2 - 1}{4}\right]\frac{\Delta R(\mathrm{x},\mathrm{y})}{R_0}, \tag{19}$$

which makes the calculation of Δn a straightforward procedure.

In the case of strongly focused beams Novotny *et al.* [89] have shown that in general case (i.e., for any NA) the electric field of initially x-polarized plane wave with the amplitude E_0 after focusing on the sample surface, reflection and recollimation (i.e., the field at the detector; see Fig. 5) is given by

$$\boldsymbol{E}_{\mathrm{det}} = -E_0\{[\cos^2(\varphi)\mathrm{r_p}(\theta) - \sin^2(\varphi)\mathrm{r_s}(\theta)]\boldsymbol{e}_\mathrm{x} + \tfrac{1}{2}\sin(2\varphi)[\mathrm{r_p}(\theta) + \mathrm{r_s}(\theta)]\}\boldsymbol{e}_\mathrm{y} \tag{20}$$

where θ is the angle of incidence, φ is the azimuthal angle in the xy-plane, $\mathrm{r_p}$ and $\mathrm{r_s}$ are the Fresnel reflection coefficients for an electromagnetic wave with the electric vector parallel and perpendicular to the plane of incidence, respectively [30], and $\boldsymbol{e}_\mathrm{x}$ and $\boldsymbol{e}_\mathrm{y}$ are unit vectors in the x- and y-direction, respectively. For normal incidence, (i.e., $\theta = 0$) $\mathrm{r_p} = -\mathrm{r_s}$ and $\boldsymbol{E}_{\mathrm{det}} = -E_0\boldsymbol{e}_\mathrm{x}$, which is, except for the minus, identical to the input field. Again, as in the case of (14), the focusing objective depolarizes light. The total power of the reflected light at the detector (i.e., the reflected signal R(x, y)) is given by an integral

$$R \propto \int_0^{\theta_{\max}} \sin(\theta)d\theta \int_0^{2\pi} \left|\boldsymbol{E}_{\mathrm{det}}(\varphi,\theta)\right|^2 d\varphi \tag{21}$$

where $\theta_{\max}$ = arcsin(NA). It can also be seen from (21) that in the considered general case a simple analytical relationship (viz., formula (19) between R_0 and ΔR-signals and Δn does not exist any more and a more involved procedure, which is outlined below, has to be used in order to deduce the magnitude of the refractive index change based on the reflected signals.

Fig. 6 shows the results of simulations based on (19) and (21) for fused silica. The refractive index of fused silica used in the simulations is taken n_0 = 1.457, which corresponds to microreflection measurements at λ = 632.8 nm (the red wavelength of the HeNe-laser). In Fig. 6(a) the refractive index change caused by fs irradiation is fixed at a typical value for this material of Δn = 0.005 (See Appendix B and ARTICLE II) and the NA of the focusing objective is varied, whereas in Fig. 6(b) Δn is varied and the calculated $\Delta R/R_0$-ratios are plotted for different fixed values of NA. Fig 6(a) demonstrates that for NA < 0.5 the difference between the calculated $\Delta R/R_0$-ratios given by the normal incidence

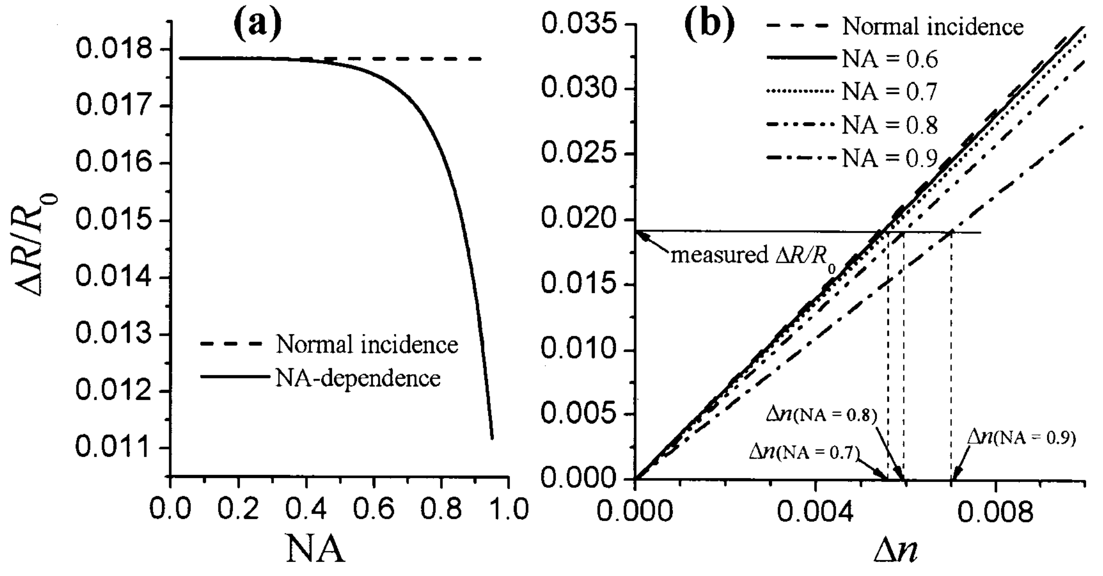

Fig. 6. Microreflection measurements using the normal incidence approximation and the model accounting for the dependence of the reflectance on the angle of incidence. (a) calculated reflectivity change induced by an index inhomogeneity with $\Delta n = 0.005$ in using focusing objectives with varying NA's. (b) calibration curves plotted for NA = 0.6, 0.7, 0.8, and 0.9 for a range of Δn corresponding to the observed refractive index changes in fused silica ($0 < \Delta n < 0.01$).

approximation (19) and the rigorous theory of microreflection (21) is very small. With an increase in NA the $\Delta R/R_0$-ratio drops but even for 0.8 NA focusing it is still within 10% of the normal incidence value. For very high numerical apertures in the range of $0.8 < \text{NA} < 0.95$ the use of the normal incidence approximation in interpreting the data results in a serious underestimation of the induced Δn (~ 25%). The NA-dependence of the $\Delta R/R_0$-ratio can be accounted for by simply using the calibration introduced in Fig. 6(b). Since the numerical aperture as well as the unmodified n_0 are known parameters[16], Δn can be deduced from the measured $\Delta R/R_0$-ratio using a procedure shown in the graph. Such calibration curves can be built for any material, any numerical aperture and for any range of Δn.

Another effect that may lead to inaccurate measurements of the induced Δn is due to the presence of a surface layer produced by polishing (Fig. 5). Early studies of this effect by Lord Rayleigh showed that the reflectance of polished fused silica and other glasses was changed by the optical polishing procedure [90]. In using immersion fluids index-matched to

---

[16] The back aperture of the focusing objective has to be essentially overfilled with the probe laser beam (which is assumed to be a Gaussian TEM_{00} mode) to avoid an apparent reduction in NA due to a decrease of the beam intensity from the axis towards its periphery.

the bulk material he found that the reflection amplitude of the outer surface of the polishing-induced layer was significantly higher than that of its inner surface, which implied a refractive index variation from n = 1.46 to 1.60 across the layer. The thickness of the layer ($\approx$ 30 nm) was determined by etching the polished surface in weak hydrofluoric acid followed by interferometric measurements. More recent measurements of the refractive index distribution normal to the polished surface of fused silica were performed using ellipsometry accompanied with gradually thinning the layer by acid etching [91]. The samples were lapped with several abrasives (emery followed by cerium oxide) having successively smaller mean grain sizes. The results showed that the refractive index initially drops in the first 5 nm very quickly from a surface value of $\approx$ 1.74 to $\approx$ 1.48 and then slowly reduces to the bulk value over a significant depth of almost 200 nm. Although there is no consensus on the surface layer formation mechanism, it is a well known fact that both thickness and refractive index of the layer are strongly affected by the polishing procedure (dry, wet, chemical-mechanical, flame polishing, etc.) [90].

The effect of the presence of a dielectric film on the reflected signal can be estimated using the following model. The reflectivity $\mathfrak{R}$ at normal incidence for a homogeneous dielectric film with a refractive index of $n = n_0 + \delta n$, i.e., surface layer, on the surface of a flat glass substrate with a refractive index n_0 ($\delta n \ll n_0$) is approximated by [92]

$$\mathfrak{R}(n_0, \delta n) \approx \left(\frac{n_0 - 1}{n_0 + 1}\right)^2 \left(1 + \frac{4}{n_0^2 - 1}\delta n\right) - \frac{4(n_0 - 1)\delta n}{(n_0 + 1)^3}\cos\left(\frac{4\pi}{\lambda} n_0 h\right) \tag{22}$$

where h is the film thickness and λ is the wavelength of the probe beam (See Fig. 5). Calculations show that when a sample is covered with a polishing-induced surface layer with $\delta n > 0$, the $\Delta R/R_0$-ratio given by

$$\Delta R/R_0 \propto \frac{\mathfrak{R}(n_0 + \Delta n, \delta n) - \mathfrak{R}(n_0, \delta n)}{\mathfrak{R}(n_0, \delta n)}$$

will be lower than that without such a layer. For example, if a fused silica sample is covered with a 30 nm-thick layer with $n = n_0 + \delta n = 1.6$, the $\Delta R/R_0$-ratio corresponding to a refractive index change of $\Delta n = 0.005$ measured at $\lambda = 632.8$ nm will be $\approx$ 85% of the value measured without the layer.

In our experiments we wet-polished samples to a high optical quality to avoid scratches, which produce complex diffraction patterns masking the true reflected signal. AFM measurements performed on polished and etched samples show that even after a very short etching (< 20s) in 0.5% HF the modified regions are already revealed. This implies that the thickness of the surface layer based on its estimated etch rate is less than 10 nm and therefore should not significantly affect our microreflection measurements. This layer can also be completely removed by pre-etching the sample without causing significant variations in topography over the selectively etched modified regions. Even though a 10% error in determining the refractive index on polished samples is still possible, this error will affect the absolute value of the measured refractive index rather than the actual index profile of the modified region.

Near-field scanning optical microscopy (NSOM). Very briefly, NSOM is an optical technique allowing one to achieve ultra-high optical resolution exceeding many times the resolution which is usually referred to in conventional microscopy and as the diffraction limit of light (i.e., $\approx 1.22\lambda/2NA$). There are three main modes of operation of NSOM: illumination, collection and reflection [93]. In our experiments we operated in the collection mode where an optical probe is positioned at a very short distance from the sample (i.e., the output of the waveguide) and the light coupled into the optical waveguide is collected through a sub-micrometer (typically ~100 nm) aperture at the tip of the probe(Fig. 7(a)). The collection mode can also be used to measure the intensity distribution in the focal volume of objectives and lenses (Fig. 7(b)) to assess the effects of sample induced spherical aberration and the degree of aberration compensation achievable with specialty objectives designed for these purposes. The optical superresolution of NSOM is attained because the light collection area is determined by the size of the aperture (tens of nanometers), rather than the wavelength (hundreds of nanometers) and the light is collected only from the region immediately below the aperture, i.e., it is within the near field where it is not diffraction limited.

The NSOM probes were fabricated from GeO_2-doped optical fibers (core diameter typically 4-8 μm, cladding diameter 125 μm) using a multi-step process [82] including i) bending of the fibers in an electric spark-discharge apparatus to allow their accommodation into a special holder compatible with the microscope SPM head, ii) a two-step selective chemical etching of the fibers in solutions comprised of HF and ammonium

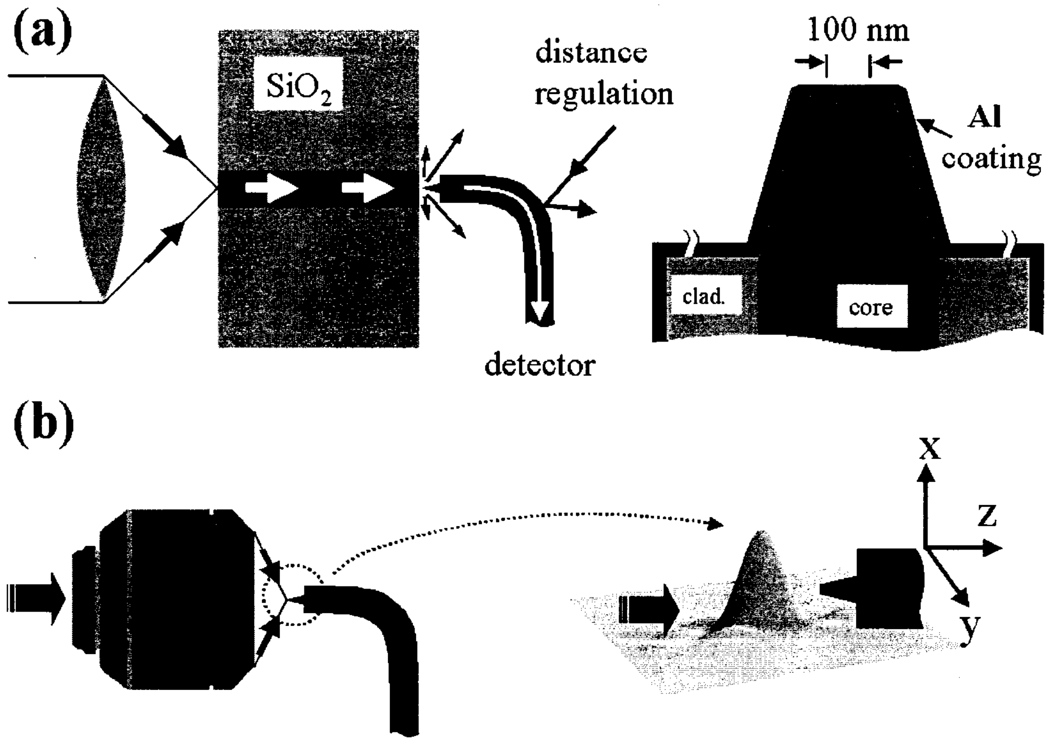

Fig. 7. Schematic diagram of a NSOM setup in the light collection mode to probe the intensity distribution (a) at the output of a fs laser-written optical waveguide in a fused silica glass sample (SiO$_2$) and (b) in the focal volume of a high-NA objective.

fluoride (NH_4F), iii) coating of the etched fibers with ~100–150 nm of aluminum, and iv) cutting off the probe tip with a focused ion beam to define the aperture. In Ref. [83] we demonstrate that these double-etched probes offer a number of advantages, viz. two orders of magnitude higher transmission, well-defined circular aperture, and durability, compared to commercially available pulled probes which are usually used by researchers. A cross-sectional view of a typical NSOM probe is shown in Fig. 7(a). The probe-sample distance regulation in performing scans on polished silica samples containing fs laser-written waveguides is based upon light deflection from the Al-coated, highly reflecting surface of a bent probe (Fig. 7(a)). The beam of a semiconductor diode laser built into the SPM head is directed downward to the top surface of the probe, where it is reflected and sent to a quadrant detector. When a NSOM probe follows topographic variations at the surface the reflected signal changes and the differential signal between the detector elements provides a feedback to the piezoelectric transducers moving the probe holder in the z-direction. During the intensity distribution scans in the foci of microscope objectives the distance regulation laser is switched off and the z-motion of the SPM head is provided by a stepper motor with a step resolution of 140 nm. Scanning along the x- and y-directions in both cases is achieved with the piezoelectric transducers.

Examples of the intensity distributions at different wavelengths at the output of a fs laser-written waveguide in fused silica obtained with NSOM are shown in Fig. 8. The mode structure of the waveguide is determined by the elongated shape of the modified region in the y-direction (See, e.g., Fig. 4 in Appendix B and Fig. 2(a) in ARTICLE VI). It is also seen that a multimode operation of the waveguide is allowed at $\lambda = 633$ nm, whereas only a single mode can be supported at a longer wavelength of $\lambda = 1550$ nm. The advantage of using NSOM to study the mode structure of waveguides is that this technique maps the intensity distribution with a very high spatial resolution (in this case $\approx$ 150 nm) directly at their outputs. Other techniques including far field measurements and the use of high-NA objectives to image the intensity distribution lack such a resolution and may be difficult to interpret. In the first case the fine mode structure will be masked by the diffraction effects developed in the far field and in the latter case the observed intensity pattern should be deconvolved with the point spread function of the imaging objective, which, in general case, has also to be measured.

Another very powerful application of NSOM in the collection mode is related to 3-D characterization of the electromagnetic fields in the focal region of high-NA objectives [94]. Other techniques proposed for these purposes including the use of CCD cameras, photosensitive films, and the knife edge, cannot achieve the resolution (which can easily be as good as 50 nm) and easiness of implementation provided by NSOM. A notable exception is another high resolution ($\approx$ 100 nm) technique based on analyzing the scattering from small conducting particles [95] or tips [96], which, however, is nothing else but apertureless NSOM [97]. Since scanning of the laser focus is performed in free space (i.e., it is not in contact with any surface) the scan rate of the NSOM probe can be high and a xy-section of the focal volume is obtained in 5-10 s. By moving the SPM head in the z-direction with a stepper motor the whole 3-D intensity distribution can be retrieved. This allows one to characterize the focal volume in a simple and direct manner and assess the actual

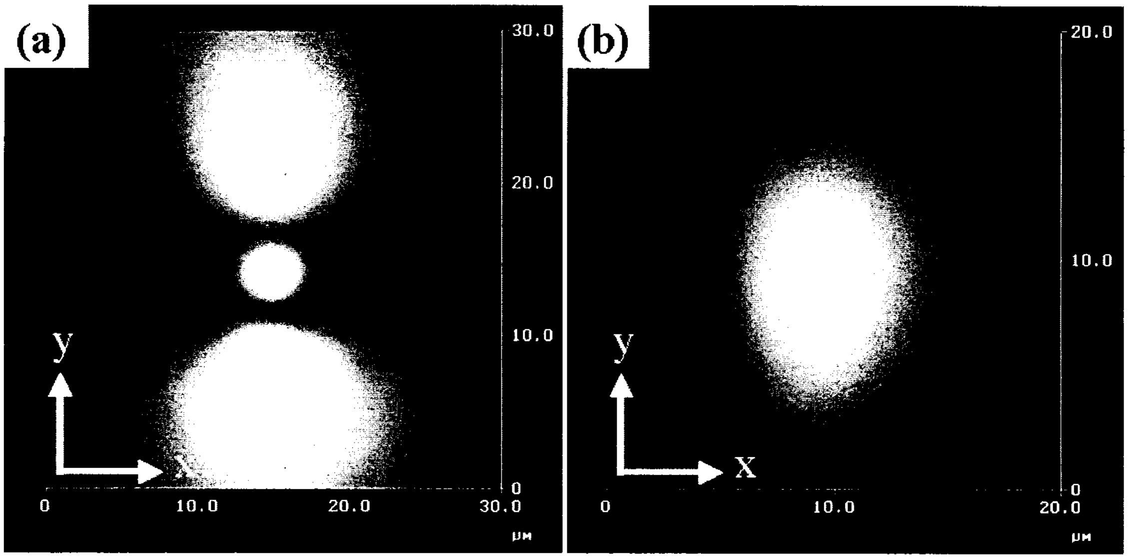

Fig. 8. NSOM image of the intensity distribution (mode structure) (a) at $\lambda = 633$ nm and (b) at $\lambda = 1550$ nm at the output of a fs laser transversely written waveguide in fused silica. The lateral resolution is determined by the NSOM probe aperture diameter, which is ≈ 150 nm for both (a) and (b).

performance of sophisticated high-NA objectives. The use of the NSOM technique becomes especially useful when focusing is performed in the presence of aberrations determined by the individual or cumulative contributions from the laser beam, the focusing optics itself, and the sample.

Fig. 9 demonstrates the potential of NSOM to study the effects of aberrated focusing with a long working distance (up to 2.2 mm) specialty microscope objective (Zeiss LD Plan Neofluar®, 63x, NA = 0.75) allowing variable coverglass correction (up to 1.5 mm). In this experiment a HeNe-laser beam at $\lambda = 632.8$ nm was spatially filtered, collimated, expanded and focused through a 1.475 mm-thick fused silica etalon (Suprasil® 2 Grade A from Heraeus, $n_0 = 1.457$ at $\lambda = 632.8$ nm). The diameter of the expanded beam was ≈ 4 times wider than the entrance aperture of the objective. These samples have also been used in the studies presented in ARTICLES III, IV, V, and VI. As it was mentioned earlier in **Section 1**, the Debye integral describing the diffraction of a converging spherical wave propagating through a planar dielectric interface can be generalized for a stratified (i.e., consisting of flat parallel layers) medium, which in this case is represented by a layer of fused silica interfaced

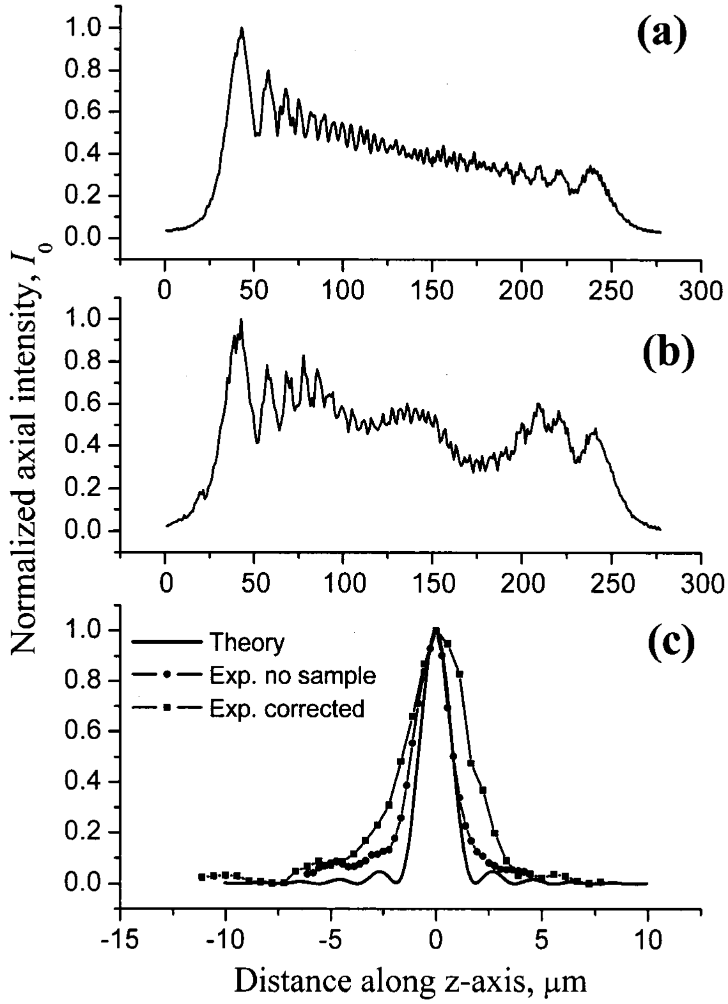

Fig. 9. Comparison of (a) calculated and (b) measured axial intensity distributions in focusing through a fused silica etalon. (c) assessment of the degree of correction provided by a by Zeiss LD Plan Neofluar®, 63x, NA = 0.75 objective.

with air from both sides. Fig. 9(a) shows the aberrated axial intensity distribution I_0 calculated for the above input parameters using the theory presented in Ref. [58] and Fig. 9(b) demonstrates the aberrated axial intensity (i.e., no compensation by the objective)measured using a NSOM probe with the aperture ≈ 100 nm in diameter. Fig. 9(c) shows calculated unaberrated intensity in the limiting case of an infinitely thin fused silica pelicle ("theory") together with the measured I_0 corresponding to the focusing in air when the sample is removed and the correction is set for no compensation, i.e., 0 sample thickness

("Exp. no sample"), and focusing through the 1.475 mm thick sample with the correction set to compensate for spherical aberration introduced by the sample ("Exp. corrected").

Several conclusions can be drawn based on the data presented in Fig. 9. There is a good agreement between the generalized theory of Török and Varga [58] and experiment, which allows one to reliably predict intensity distributions *inside* samples when the laser radiation is focused through a single sample-air (immersion fluid) refractive index mismatched interface. As a matter of fact, it is the simplest special case of this theory. Although there have been no doubts about the validity of the theory proposed by Török and Varga, to the best of our knowledge, we are the first to perform ultra-high resolution studies of the intensity distribution in the focal volume in the presence of spherical aberration introduced by a dielectric interface. We believe, that the deviation of the experimental data from thetheoretical prediction is caused by the residual aberrations introduced by the objective itself. Fig. 9(c) shows, e.g., that the "real" intensity distribution measured in the absence of the sample, which represents the optimum performance of this objective, is slightly asymmetric and about 15% broader than that predicted by the theory. In the case of corrected focusing through the sample, the axial FWHM of the distribution is almost two times greater than for the focusing in air, but is still incommensurately narrower than the uncompensated distribution (See Fig. 9(b)). At the central wavelength of the Ti-Sapphire fs laser system ($\lambda \approx$ 800 nm) the compensation of the objective is expected to deteriorate as it is optimized for the operation in visible light (450-700 nm). We are currently setting up experiments to perform NSOM studies of focused Ti-Sapphire fs laser beams, which will allow us to i) assess how the quality of the fs laser beam and objectives affects the intensity distributions in the focus and ii) investigate the possibility of shaping the focal volume by inserting phase-amplitude masks in the beam.

Discussion

The pronounced dependence of the modification on the laser parameters and the material requires diagnostics techniques enabling characterization of both the morphology and physicochemical properties of the induced structural changes. These changes generally occur on a microscopic scale but in the regime of nanograting formation their extent can be less than 10 nm (e.g., typical width of the planar nanocracks forming nanogratings). This immediately implies that the diagnostic tools should provide a spatial resolution adequate to visualize and characterize extremely fine features. There is no single technique which would allow one to meet the ultra-high resolution criterium and simultaneously provide information on the optical, physical and chemical properties of the modified regions. However, a combination of different diagnostic methods can be successfully employed to complement each other. In this thesis the modification morphology is studied using the etching-AFM/SEM techniques (resolutions ~ 15 nm/ 5 nm, respectively), the refractive index changes are characterized by the microreflection technique (resolution ~ 400 nm), and the actual performance of the fs laser-written waveguides is assessed using NSOM (resolution ~50-100 nm). In the Main section of the thesis we demonstrate that these techniques have allowed us to establish the link between the writing conditions and the morphological transformations occurring in different glasses.

APPLIED PHYSICS LETTERS VOLUME 85, NUMBER 8 23 AUGUST 2004

Microreflectivity characterization of the two-dimensional refractive index distribution of electron-beam-written optical waveguides in germanium-doped flame-hydrolysis silica

S. García Blanco[a] and J. S. Aitchison
Department of Electrical and Computer Engineering, University of Toronto, Toronto, M5S 3G4, Canada
C. Hnatovsky and R. S. Taylor
Institute for Microstructural Sciences, National Research Council, Ottawa, K1A 0R6, Canada

(Received 3 March 2004; accepted 21 June 2004)

In this letter, we report on the detailed refractive index distribution of optical waveguides induced by electron-beam irradiation of Ge-doped flame hydrolysis silica and its variation with dose. The characterization was performed using microreflectivity measurements. © *2004 American Institute of Physics*. [DOI: 10.1063/1.1784541]

Planar silica is extensively used for the production of integrated optical circuits for communications systems and more recently for optical bio-sensing applications.[1] However, the production of these circuits involves a number of process steps, including optical lithography, reactive ion etching, and overgrowth. The etching step, which introduces surface roughness, needs to be accurately controlled to ensure vertical sidewalls and is time consuming. In recent years there has been a growing interest in alternate methods for the fabrication of waveguides in silica, based on irradiation with UV lasers,[2] high energy ions,[3] and focused electron beams.[4] These processes cause a change in the structure of the silica, which in turn, leads to a change in the refractive index. By controlling the exposure, the beam size, and position it is possible to directly write waveguides and optical circuit elements.

The refractive index change induced by irradiation of a slab waveguide with 50 keV electrons has been previously characterized by analysing the effective refractive indices of the different propagation modes supported by the structure (m-lines technique).[5] However, for accurate design of optical circuits, knowledge of the two-dimensional distribution of the index of refraction of the waveguide is important. This is particularly true for large area planar lightwave circuits, which rely on precise control of the phase of the optical mode.

Different techniques have been used to characterize the refractive index distribution of the core of optical fibers and waveguides,[6] such as near-field profiling (i.e., refracted near-field method and bound near-field method), far-field profiling, interferometry, and reflection. More recently, techniques offering a higher spatial resolution, such as selective etching followed by scanning with an atomic force microscope[7] and NSOM (near-field scanning optical microscopy)[8] have been receiving interest. In this letter, a microreflectivity technique,[9] with a spatial resolution of ~400 nm, was used in order to characterize the two-dimensional refractive index distribution of optical waveguides written in germanium-doped silica by irradiation with an energetic electron beam and its variation with irradiation dose.

The samples consisted of a silica layer, co-doped with germanium and boron, deposited by flame-hydrolysis deposition (FHD)[10] on a silicon substrate which had 15 μm of thermal oxide previously grown on it. The thickness of the FHD silica layer was measured to be ~5 μm by selectively etching part of the layer in concentrated (40%) hydrofluoric acid (HF) followed by surface profilometry. The results were consistent with those obtained by optical microscopy with dia-illumination. The average germanium content of the layers was 7 wt % as measured by energy dispersive x-ray analysis (EDX). To avoid charge accumulation during the irradiation, a 30-nm -thick layer of NiCr was evaporated on top of the FHD silica substrates and subsequently removed by wet-etching. Electron-beam irradiation was performed using a 400-nm-diam electron beam, with an acceleration energy of 50 keV, a current of 100 nA and doses ranging from 0.01 to 1 C cm^{-2}. Waveguides with a nominal width of 10 μm were written using these conditions. Prior to the microreflectivity measurements, the end-facets of the sample were carefully polished to a high optical quality in order to minimize the influence of artifacts on the measurements. If the end-facets of the sample present topography, care must be taken in the interpretation of the measured data. In the present case, a step smaller than 20 nm was observed by an atomic-force microscope between the FHD silica layer and the thermal oxide. This topography is attributed to the unavoidable differential etch rate of the two layers during the chemical-mechanical polishing. However, artifacts are not expected to be significant for step heights below 50 nm. This was verified by wet-etching the end-facet of a SMF-28 fiber. The germanium-doped core etches faster than the cladding. Microreflectivity measurements were performed after each etching step. Only for height differences of more than 50 nm between core and cladding did the microreflectivity measurements show any artifacts. The refractive index values of the top 500 nm of the FHD layer may exhibit a small artifact, due to the large index step between the air and the material. The output facet of each waveguide was terminated by scratching it and depositing a bead of epoxy in order to minimize any reflected feedback to the front surface.

The setup used for the microreflectivity measurements is shown in Fig. 1(a). The beam from a Power Technology Inc. laser diode with a maximum power of 15 mW and a wavelength centered at 635 nm was coupled into a 30 m length of

---

[a] Electronic mail: sgblanco@ieee.org

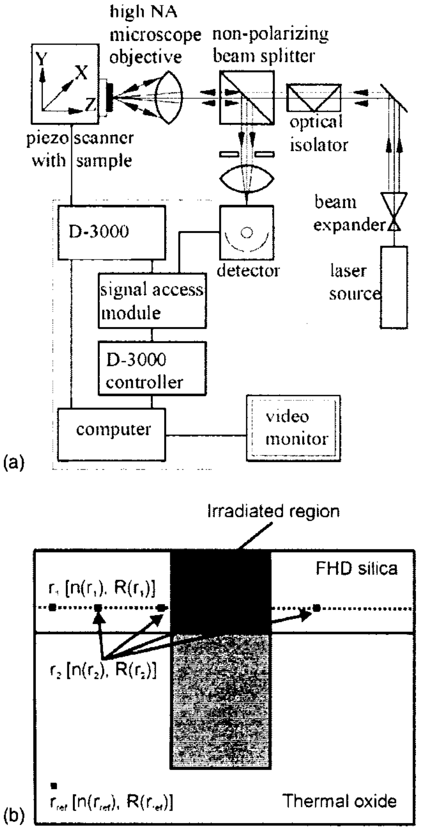

FIG. 1. (a) Microreflectivity experimental setup; (b) reference points taken for the measurements.

a single model (at λ=633 nm, HeNe) optical fiber. The output of this fiber was expanded and collimated using a 10× microscope objective with a numerical aperture (NA) of 0.25. The fiber played a role of a spatial filter to improve the spatial characteristics of the diode laser beam. Any feedback to the laser was removed by means of an optical isolator (a polarizer combined with a λ/4-waveplate). The laser beam was focused on the sample surface with a Carl Zeiss 50×, NA=0.8 microscope objective. The power of the incident beam after the focusing lens was adjusted to ~1 mW using a neutral density filter placed immediately after the isolator. The sample was mounted on a *XYZ*-piezo scanner (the scanning head of a Digital Instruments Dimension-3000 atomic force microscrope). The piezo-scanner has an typical accuracy of 1% of the maximum selected scan size and 16 bit electronic resolution on all axes. The light reflected from the end-facet of the sample was redirected with a nonpolarizing cube beam-splitter onto the detector (model 818-UV) of the Newport 1830-C optical power meter. The sample was oriented in a special holder in such a way that the diameter of the collimated reflected beam was constant during the scan. This ensured that the sample surface was kept at the same position with respect to the focus. The Fresnel equations for normal incidence reflection from a surface relate the refractive index of the materials present at the interface with the reflectivity, as

$$R(r)=\left(\frac{n_0-n(r)}{n_0+n(r)}\right)^2=\left(\frac{1-n(r)}{1+n(r)}\right)^2, \qquad (1)$$

where n_0 is the refractive index of the incidence medium, in this case air ($n_0=1$) and $n(r)$ is the refractive index at the measurement position r. From Eq. (1) it can be derived:

$$\Delta n=\frac{n(r)^2-1}{4}\frac{\Delta R}{R(r)}, \qquad (2)$$

where $n(r)$ and $R(r)$ are the refractive index and reflectivity at the position r and Δn and ΔR are the increments of refractive index and reflectivity from the reference point r. If we call the reference position r_{ref}, the refractive index at a different position r' can be calculated as

$$n(r')-n(r_{\mathrm{ref}})=\frac{n(r_{\mathrm{ref}})^2-1}{4}\frac{R(r')-R(r_{\mathrm{ref}})}{R(r_{\mathrm{ref}})}. \qquad (3)$$

The reference point has to be chosen so that the refractive index for that point is known. In the present case, we have taken as reference the thermal oxide, for which the value of refractive index at 633 nm is 1.4582. Using Eq. (3), the refractive index difference between two positions, r_1 and r_2, on a single cross section along the FHD layer can be calculated as:

$$\Delta n=n(r_2)-n(r_1)=\frac{1}{4}(n(r_{\mathrm{ref}})^2-1)\frac{R(r_2)-R(r_1)}{R(r_{\mathrm{ref}})}, \qquad (4)$$

where the different parameters are indicated in Fig. 1(b). A more rigorous theory of micro-reflection[11] takes into account the cone of light rays incident onto the sample surface and not just normal incident rays. For a measured $\Delta R/R$ the normal incidence calculation underestimates the Δn for numerical apertures in excess of ≈0.75. The focusing lens used in the experiments has a NA=0.8 just exceeding this value, however the laser beam underfilled the entrance pupil of the lens thus decreasing its effective NA. A commercially available SMF-28 telecom fiber, from Corning Inc., with a known core-cladding refractive index step ($\Delta n=0.0053$ at 633 nm) was used to check whether the normal incidence approximation was enough or whether rigorous approaches were necessary in the data analysis. The micro-reflection data obtained at 635 nm on a number of SMF-28 fiber samples using the normal incidence approximation gave an averaged Δn of 0.0052±0.002. This number is in a good agreement with the manufacturer's data and so there is no need to introduce a high NA-related correction factor.

Figure 2(a) shows the refractive index distribution across the end-facets of two waveguides (nominal width 10 μm) written with doses of 0.1 C cm^{-2} (top) and 1 C cm^{-2} (bottom). For the smaller dose, 0.1 C cm^{-2}, the shape of the waveguide clearly resembles the way the electrons are predicted to deposit their energy inside the material. This can be seen in Fig. 2(b), which shows the energy deposition inside the material calculated by Monte Carlo simulations performed on silica material doped with an average germanium content of 7 wt %. As the dose increases the index of refraction profile becomes more complex exhibiting higher refractive index regions surrounding the volume where the electrons were thought to have deposited most of their energy. This results in significant widening of the written waveguides with respect to their nominal width. The effect of the irradiation is also found in the thermal oxide area.

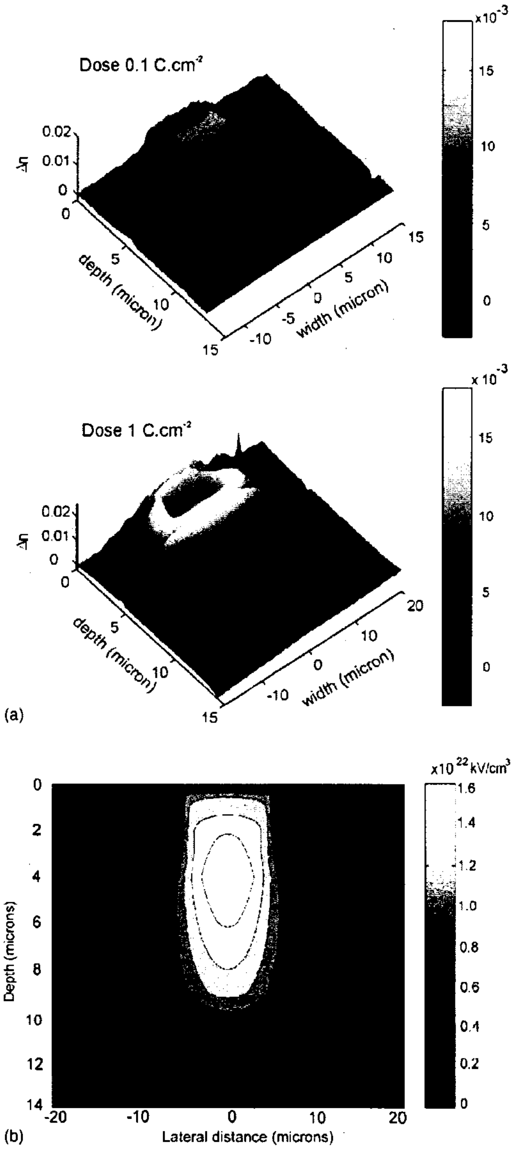

FIG. 2. (a) Refractive index profiles induced by electron-beam irradiation of Ge-doped FHD silica after a dose of 0.1 C cm^{-2} (top) and 1 C cm^{-2} (bottom) measured by microreflectivity. The nominal width of the waveguides is 10 μm and the acceleration voltage used was 50 keV, (b) Monte Carlo simulation of the energy deposited into Ge-doped silica by a 50 keV electron beam with dose 0.1 C cm^{-2}.

although smaller than in the FHD silica layer, due to the lesser amount of energy deposited by the electrons at that depth and the different sensitivity of this material.

The reason for the complicated distribution of the index of refraction profiles and their variation with electron dose is not fully understood. From Fig. 2(a) it can be clearly seen that two features are present. Even for small doses, 0.1 C cm^{-2}, the refractive index change extends further than the width irradiated on the surface, producing a widening of the waveguides. This effect was observed by Leick *et al.*[12] for waveguides fabricated with UV irradiation. They measured an increase in the width of the waveguides with applied dose to double the size of the focused laser spot size. Similar broadening was observed using NSOM to measure the width of UV-written optical waveguides[8] and after irradiation with a focused proton beam.[13] However, due to the different nature of those irradiations, the reasons for the widening of the waveguides in each case might be due to different mechanisms, such as local heating, scattering of the radiation inside the material or stress. In the case of electron beam irradiation, the dominant contribution seems to be scattering of the electrons as they enter the material. The second feature present in the waveguides is the ring-like zones of index modification which at higher dosage result in two regions of higher index of refraction surrounding the irradiated area. This effect could possibly be attributed to the stresses originating between the irradiated and nonirradiated regions due to compaction of the structure. Another reason could be migration of germanium outside the region where most of the energy was deposited. Figure 2(b) also shows an increase of the refractive index towards the surface for the 1 C cm^{-2} waveguide. A densification region near the surface was reported before for the same material and dosage[4] and can be attributed to the nature of the Ge-doped FHD silica, which presents lower density and germanium content near the surface. Further in-depth studies of the structural changes across the cross section of the waveguides by confocal micro-Raman spectroscopy and birefringence measurements with polarized light microscopy, together with elasticity simulations of the compaction mechanisms, are being carried out.

In summary, a microreflectivity technique was used to obtain high resolution (≈400 nm) refractive index profiles of optical waveguides fabricated by electron-beam irradiation of germanium-doped FHD silica. The analysis of the collected data show that (1) the regions of refractive index modification are wider than the irradiated areas for all dosage, (2) for the higher dosages (0.5 and 1 C cm^{-2}) the refractive index profiles show a complex ring-like structure.

The authors would like to thank NSERC for support through the research network on agile all-photonic networks and the Nanoelectronics Research Center of the Electronics and Electrical Engineering of the University of Glasgow for access to the beamwriter.

[1] J. M. Ruano, V. Benoit, J. S. Aitchison, and J. M. Cooper, Anal. Chem. **72**, 1093 (2000).
[2] G. D. Maxwell and B. J. Ainslie, Electron. Lett. **31**, 95 (1995).
[3] S. García-Blanco, A. J. Kellock, J. E. E. Baglin, A. Glidle, J. M. Cooper, J. S. Aitchison, and R. M. Delarue, Nucl. Instrum. Methods Phys. Res. B **206**, 440 (2003).
[4] S. Garcia-Blanco, A. Glidle, J. H. Davies, J. S. Aitchison, and J. M. Cooper, Appl. Phys. Lett. **79**, 2889 (2001).
[5] A-S. Jacqueline, S. Garcia-Blanco, B. Poumellec, and J. S. Aitchison, J. Non-Cryst. Solids **322**, 284 (2003).
[6] W. J. Stewart, IEEE J. Quantum Electron. **QE18**, 1451 (1982).
[7] R. S. Taylor, C. Hnatovsky, E. Simova, D. M. Rayner, M. Mechandale, V. R. Bhardwaj, and P. B. Corkum, Opt. Express **11**, 775 (2003).
[8] M. Svalgaard, S. Madsen, J. M. Hvam, and M. Kristensen, IEEE Photonics Technol. Lett. **10**, 848 (1998).
[9] M. Ikeda, M. Tateda, and H. Yoshikiyo, Appl. Opt. **14**, 814 (1975).
[10] P. V. S. Marques, J. R. Bonar, A. M. P. Leite, and J. S. Aitchison, IEEE J. Sel. Top. Quantum Electron. **8**, 1316 (2002).
[11] H. Wang, Optik (Stuttgart) **102**, 36 (1996).
[12] L. Leick, A. Harpoth, and M. Svalgaard, Appl. Opt. **41**, 4325 (2002).
[13] M. L. Von Vibra, A. Roberts, P. Mulvaney, and S. T. Huntington, J. Appl. Phys. **87**, 8429 (2000).

JOURNAL OF APPLIED PHYSICS 97, 083102 (2005)

Femtosecond laser-induced refractive index modification in multicomponent glasses

V. R. Bhardwaj, E. Simova,[a)] P. B. Corkum, and D. M. Rayner
Steacie Institute for Molecular Sciences, National Research Council, 100 Sussex Drive, Ottawa, Ontario, K1A 0R6, Canada

C. Hnatovsky
Department of Physics, University of Ottawa, Louis Pasteur, Ottawa, Ontario, K1N 6N5, Canada

R. S. Taylor
Institute for Microstructural Sciences, National Research Council, 1200 Montreal Road, Ottawa, Ontario, K1A 0R6, Canada

B. Schreder, M. Kluge, and J. Zimmer
SCHOTT AG, Corporate Research and Technology Development, D-5512 Mainz, Germany

(Received 29 October 2004; accepted 27 January 2005; published online 4 April 2005)

We present a comprehensive study on femtosecond laser-induced refractive index modification in a wide variety of multicomponent glasses grouped as borosilicate, aluminum–silicate, and heavy-metal oxide glasses along with lanthanum–borate and sodium–phosphate glasses. By using high-spatial resolution refractive index profiling techniques, we demonstrate that under a wide range of writing conditions the refractive index modification in multicomponent glasses can be positive, negative, or nonuniform, and exhibits a strong dependence on the glass composition. With the exception of some aluminum–silicate glasses all other glasses exhibited a negative/nonuniform index change. We also demonstrate direct writing of waveguides in photosensitive Foturan® glass with a femtosecond laser without initiating crystallization by thermal treatment. Upon ceramization of lithium–aluminum–silicate glasses such as Foturan®, Zerodur®, and Robax® we observe switching of laser-induced refractive index change from being positive to negative. The measured transmission losses in the waveguides at 1550 nm agree with the index profile measurements in alkali-free aluminum–silicate glasses. *© 2005 American Institute of Physics.*
[DOI: 10.1063/1.1876578]

I. INTRODUCTION

Femtosecond lasers, with their ability to deposit energy in materials with spatial and temporal precision, are increasingly finding applications in the areas of microfabrication, laser surgery, photonics, integrated optics, biomedical imaging, and nanotechnology.[1–7] Current research in modification of dielectric properties inside bulk transparent materials such as glasses with a femtosecond laser is driven by its ability to directly fabricate three-dimensional photonic devices and nanostructures.[4,7,8]

The laser-glass interaction proceeds through a nonlinear multiphoton process providing high-spatial resolution and three-dimensional access while ultrashort pulse duration ensures the process is deterministic with minimal thermal damage to the surrounding material.[9] Localized changes to the refractive index of glass can be induced leading to the fabrication of waveguides, the basic building blocks of any photonic device,[3] high-density three-dimensional optical storage,[8] and nanostructures.[7]

Passive devices such as splitters, couplers, interferometers, and gratings along with waveguides in amplifying medium have been fabricated reviving the interest in glass integrated optics. Also, the laser-modified region in glass can undergo selective chemical etching forming nanostructures and microfluidic channels.[7,10] Therefore, dielectric modification by a femtosecond laser is emerging as an alternate technique to fabricate the three-dimensional (3D) optical chips and micrototal analysis systems.

Glass has a high optical damage threshold associated with the large material band gap, making it an attractive material in photonic and biophotonic applications. Fused silica is the most widely used material in which waveguides, nanostructures, and microfluidic channels have been fabricated.[3,7,10] However, multicomponent glasses are indispensable to fabricate active integrated devices since their network structure can be easily altered to accommodate molecules that provide the desired active and nonlinear properties. They are also important in biophotonics where photonic devices are incorporated along with microfluidic channels.

Femtosecond laser-induced localized refractive index modification has been demonstrated in a wide variety of optical glasses [such as Ge-doped silica, borosilicate, borate, phosphate, fluorophosphates, fluoride, chalcogenide, soda–lime, and fluorozirconate (Refs. 4 and 11–15)] under different experimental conditions. The possibility of writing active devices has also been demonstrated in Er–Yb and Nd-doped silicate glasses.[16,17] The magnitude of the refractive index modification in most of these glasses has been estimated in-

---

[a)] Electronic mail: eli.simova@nrc.ca

directly from numerical aperture (NA) measurements and near- and far-field pattern analyses.[12] In very few cases refractive index profiles of the waveguides were measured using either a microellipsometer[3] or a refractive near-field technique.[4,15]

Also, selective etching of the laser-modified region in few glasses has been investigated. Photosensitive glass Foturan® is one such glass which was studied extensively leading to fabrication of embedded micro-optical components and microchannels.[5,18] However, a detailed study on refractive index modification in a wide variety of multicomponent glasses has not been conducted to assess their suitability for photonic applications.

We present a comprehensive study on femtosecond laser modification of refractive index in a wide variety of multicomponent glasses from SCHOTT AG. They are grouped into four categories: borosilicate (BK7, lithium–borosilicate, and D263), aluminum–silicate [8261 alkali–aluminum silicate, and lithium–aluminum–silicate (LAS) glasses and their ceramics], heavy-metal oxide glasses (lead–silicate SF57 and bismuth–silicate), and other optical glasses (IOG-1 and lanthanum–borate).

Using high-spatial resolution techniques such as microreflectivity,[19] refractive near field (RNF), and chemical etching/atomic force microscopy[20] (AFM) we measure the refractive index profiles of the laser-modified regions. We report negative (or nonuniform) refractive index changes in all glasses except for some aluminum–silicate glasses where waveguiding is possible. Below we highlight the important results:

- We observe a uniform negative index change in borosilicate glass BK7 in the low-energy regime.
- We can directly induce index changes in Foturan® glass without any thermal annealing.
- Index change is positive in LAS glasses whereas their respective ceramics show a negative index change.
- Weak index change in lanthanum–borate glass is due to color-center formation. Index profile in sodium–phosphate glass is nonuniform with negative index change in the center followed by positive side lobes.
- Glasses containing high alkali and heavy-metal content do not show selective etching of the laser-modified regions. Selective etching is independent of the sign of laser-induced index change.

In Sec. II, we present a brief description of conditions under which waveguides were fabricated along with different characterization techniques. Experimental results are presented in Sec. III followed by a discussion in Sec. IV on the possible mechanisms responsible for the observed index changes in multicomponent glasses.

II. EXPERIMENT

In two sets of experiments, different regeneratively amplified Ti:sapphire femtosecond lasers were used for waveguide fabrication with the central wavelength at 800 nm. In the first set, we use a variable repetition rate laser (10–100 kHz) producing ultrashort pulses that are 50 fs in duration and 2.4 μJ in energy. The pulse energy is varied with a variable neutral density filter before a spatial filter. The laser beam is focused 350 μm below the sample surface with a 40 × (NA=0.65) microscope objective. The structures are fabricated in transverse geometry by translating the sample perpendicular to the propagation direction of the laser beam with variable translation speeds from 10 to 200 μm/s and light polarization along the translation direction.

Since the waveguide cross sections are highly elliptical in transverse geometry, a long focal length (40 cm) cylindrical lens is used in front of the microscope objective at angles of 5°, 10°, and 15° with respect to the translation direction to vary the waveguide cross sections.[4] The multicomponent glasses that were investigated under these conditions are SCHOTT's BK7, lithium–borosilicate, 8261 aluminum–silicate, alkali aluminum–silicate, SF57 lead-silicate, IOG-1 sodium–phosphate, and lanthanum–borate glasses.

In the second set of experiments, we use a 1-kHz repetition rate laser producing 80 fs pulses with a laser output power between 35 and 65 mW. A semitransparent mirror (R60/T40) splits the incoming beam and a power meter constantly monitors the laser power of the transmitted beam. The power of the reflected beam is reduced by a combination of neutral density filters. A microscope Zeiss Achroplan 20 × (NA=0.45) objective then focuses the beam into the sample at a depth of about 250 μm. A two-dimensional motion controller enables the writing of straight waveguides and bent structures. In order to find the optimum energy for waveguide writing, sets with varying writing velocities (65, 125, 250, 500, and 1000 μm/s) and varying laser power were written into each glass. For most glasses, an acceptable range for the velocity was found to be 125–250 μm/s.

The multicomponent glasses that were investigated under these conditions are SCHOTT's LAS glasses such as Zerodur®, Robax®, and Foturan® and their respective glass ceramics along with BK7 and D263 borosilicate, IOG-1 sodium–phosphate, SF57 lead–silicate, and bismuth–silicate glasses. Two of the LAS glasses were also structured with different wavelengths, 620 nm (1–5.5 μJ at sample) and 960 nm (7–12.5 μJ at sample) that lie near the two-photon or three-photon absorption of cerium. These wavelengths were produced by doubling the tunable output of an Optical parametric amplifier pumped by a Ti–sapphire laser. The pulse duration is 150 fs and the beam is focused into the sample with a 50 × (NA=0.75) microscope objective.

Characterization of the fabricated waveguide structures is carried out with a conventional microscope, microreflectivity,[19] RNF technique, combined selective etching and AFM,[20] and transmission loss measurement. For the microreflectivity and the selective etching/AFM, the glass blocks are cut into two pieces perpendicular to the translation direction and the inside surfaces are polished and characterized. The obtained index profiles are independent of the cut location. A detailed description of the experimental setup and validation of the microreflectivity technique is presented elsewhere.[19] The microreflectivity technique allows detection of positive and negative refractive index profiles with a spatial resolution of 400 at 633 nm and a low limit in the order of $\Delta n \sim 0.0005$.

After the microreflectivity measurements, the glass samples are etched in 1% hydrofluoric acid (HF) solution typically for 6 min. The etched surfaces are then scanned with AFM to reveal the topography in the modification regions, which indicates the fine structure and uniformity of the refractive index change. The technique of selective chemical etching followed by scanning with AFM, proposed and validated for fused silica,[20] offers a higher spatial resolution of 20 nm. Transmission loss measurements are carried out at 633 and 1550 nm. Light is coupled to the sample by a single-mode tapered fiber and a multimode fiber collects the exiting light onto a detector with no index matching oil on the sample facets.

III. RESULTS

To highlight the important experimental observations obtained under a wide range of writing conditions, we assort the multicomponent glasses into four main groups: (a) borosilicate (BK7 and lithium–borosilicate and D263), (b) aluminum–silicate (8261, alkali–aluminum–silicate, and LAS glasses and their ceramics), (c) heavy-metal oxide glasses (lead–silicate SF57 and bismuth–silicate), and (d) other optical glasses (IOG-1 and lanthanum–borate).

A. Borosilicate glasses

They are optical grade glasses that provide excellent transmission through visible to near-infrared spectra and are a good alternative to fused silica. We report the femtosecond laser-induced refractive index modifications in BK7, lithium borosilicate and D263 glasses investigated with microreflectivity, RNF, and chemical etching/AFM techniques.

In BK7, the modification was induced by both high and low repetition rate femtosecond lasers. Figure 1 shows typical two-dimensional scans of refractive index profiles of the waveguides in BK7 obtained by microreflectivity and chemical etching/AFM techniques. The uniform dark area revealed by microreflectivity measurements at 633 nm, Fig. 1(a), corresponds to a negative refractive index change. The magnitude of the negative refractive index change in BK7 is $\Delta n \sim 0.004 \pm 0.0001$ averaged over many samples within the waveguide cross section, as shown in Fig. 1(b).

The chemical etching/AFM technique [Fig. 1(c)] has a better spatial resolution than the optical technique and reveals a 25% modulation in etch depth with a period of ~500 nm. This modulation, which was also observed in fused silica, could provide an additional loss mechanism in the written waveguides. The origin of this modulation is under investigation and will be the subject of another paper. Although this technique has high-spatial resolution and the etch depth could be correlated to the magnitude of index change,[20] it cannot reveal the sign of the index change.

The uniform negative refractive index change in BK7 is achieved under specific writing conditions. When the dosage (defined as energy deposited per unit volume) is increased an island of unmodified regions appears within the center of the waveguide cross section. At even higher dosages the refractive index becomes nonuniform with islands of positive index change. The negative index change is also confirmed by the experiments with lower repetition rate laser. Here, the microscope images and RNF both showed a waveguide profile that has a negative Δn in the center and positive, weakly guiding side lobes. The relative position and intensity of the side lobes varied with pulse energy.

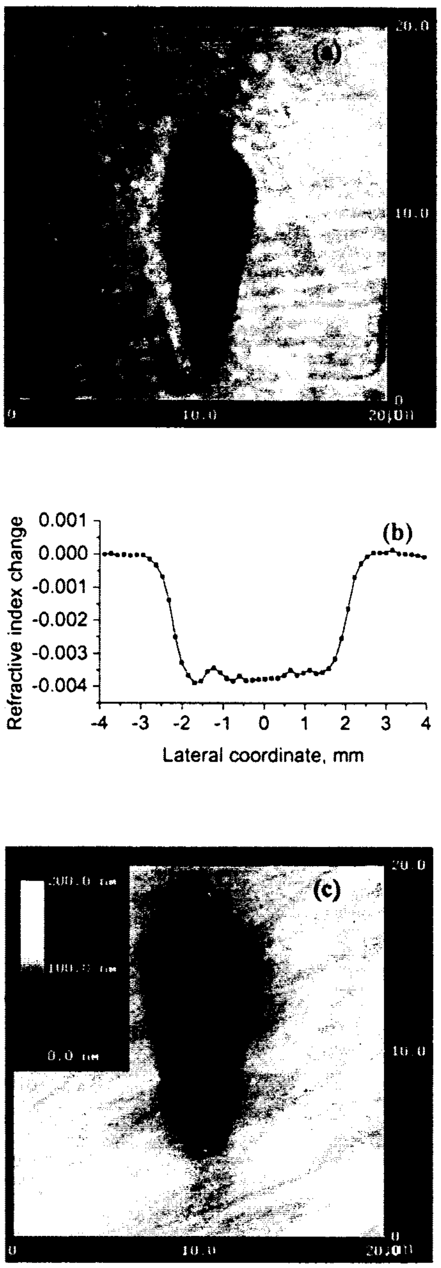

FIG. 1. 2D scans ($20 \times 20\ \mu m^2$) of the modified area in BK7 glass: (a) microreflectivity, (b) measured refractive index profile averaged over 20 scan lines, and (c) chemical etching/AFM technique. The writing conditions are 250 mW, 100-kHz repetition rate, 100-μm/s translation speed, and 5° angle of the cylindrical lens.

The negative refractive index change in BK7 is in contrast with the results obtained in other borosilicate glasses by various research groups. Waveguiding in borosilicate Corning glass 7890 (Ref. 4) and 0211 (Ref. 11) has been shown with a refractive index modification of $\Delta n \sim 0.0045$ estimated by using RNF technique and NA measurement and $\Delta n \sim 0.0003$ from beam divergence.[17] Also, in another Corning boron-doped silicate glass, the NA measurement estimated a refractive index change of $\Delta n \sim 0.002-0.005$ for different writing parameters.[14]

In lithium–borosilicate glass, which additionally contained aluminum and zinc oxide, the high repetition laser was used to induce refractive index modification. The microreflectivity data from the structures always show a weak nonuniform negative index change $\Delta n \sim -0.0003 \pm 0.0002$ under a wide range of writing conditions. This glass could not be investigated by chemical etching/AFM technique, as it does not show selective etching. This is because relatively higher alkali content in such glasses renders them to have less chemical stability than alkali-free glasses. The lowest measured losses are 10 dB/cm at 633 nm for a writing angle of 15° of the cylindrical lens, independent of the translation speed.

D263 is a general-purpose borosilicate glass made from high-purity raw materials and is very resistant to chemical attack with low alkali mobility. It is designed for thin glass and microsheet applications such as electroluminescent displays, liquid-crystal displays (LCDs), solar cells, charge-coupled device (CCD) lenses, and diagnostic slide substrates. Waveguides were fabricated with low repetition rate femtosecond laser and their analysis with RNF technique revealed negative index change.

B. Aluminum–silicate glasses

1. Alkali-free and alkali containing glasses

Schott glass 8261 is an alkali-free aluminum–silicate glass containing alkali earth metals such as magnesium, calcium, strontium, and barium. Because of its high heat and chemical resistance along with low coefficient of thermal expansion and absence of alkali metals it finds tremendous applications in electronic and display industry as an ideal substrate for thin-film transistors and active matrix LCD.

Figure 2(a) shows the refractive index profile of a waveguide structure in glass 8261 obtained with microreflectivity. The structures were fabricated with the high repetition rate femtosecond laser using a cylindrical lens at 6° writing angle. Glass 8261 shows a uniform positive refractive index change of $\Delta n \sim +0.003 \pm 0.0002$ under the specific writing conditions (the parameters are 24 and 240 mW in power, 10 and 100 kHz in repetition rate, respectively, and 100 and 200 μm/s in translation speed).

The measured transmission losses of the waveguides in 8261 decrease with increasing dosage. The lowest loss (4.0 dB/cm) waveguides in 8261 are obtained at high dosage, 10–25-μm/s translation speed and at 10° and 15° writing angle of the cylindrical lens. Slightly lower losses (by 0.3 dB/cm) are measured for laser polarization parallel to the translation direction compared to the perpendicular polarization.

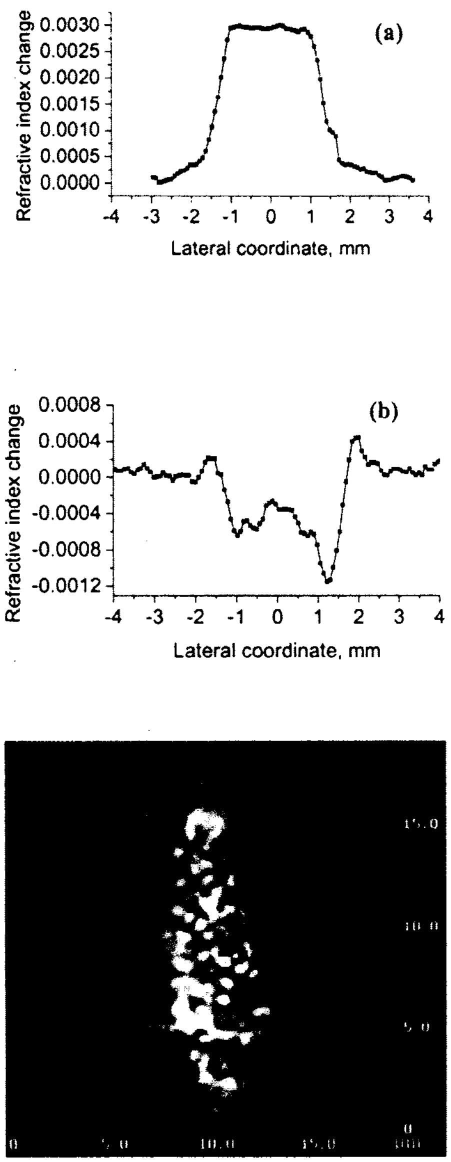

FIG. 2. Measured refractive index profile averaged over 20 scan lines in (a) aluminum–silicate glass 8261, (b) alkali–aluminum–silicate glass, and (c) 2D microreflectivity scan of modified area in alkali–aluminum–silicate glass. Laser parameters are 50 fs and 100 KHz.

Replacing alkali earths and boron in 8261 glass with sodium and lithium results in alkali–aluminum–silicate glass which exhibits higher coefficient of thermal expansion and lower chemical stability. The laser-induced modification in alkali–aluminum–silicate glass exhibits nonuniform refractive index change, with islands of positive $\Delta n \sim 0.0004$ at the edges, and negative $\Delta n \sim -0.0012 \pm 0.0002$ in the center, as shown in Fig. 2(b). Typical microreflectivity two-dimensional (2D) scan for this case of nonuniform refractive

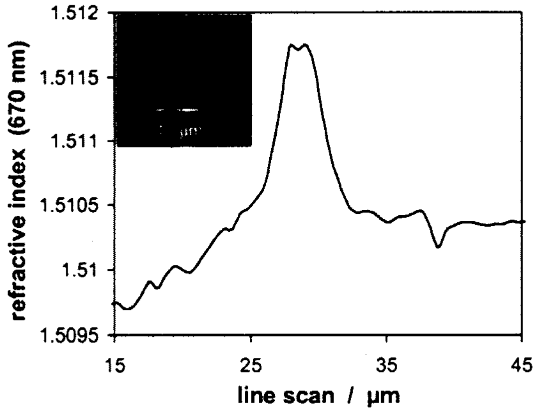

FIG. 3. Measured RNF scan of a waveguide in Foturan®. Inset shows microscope image of the waveguide. Laser parameters are 80 fs and 1 KHz.

index modification is shown in Fig. 2(c), where the dark (bright) areas correspond to negative (positive) refractive index changes.

Therefore, as a result of this exchange not only the thermal and chemical properties of the glass deteriorate, but also the refractive index change Δn switches from being positive to nonuniform. The selective etching of the modified areas is not pronounced in alkali–aluminum–silicate glass due to poor chemical stability. High losses are measured in alkali–aluminum–silicate glass, which suggest that no waveguiding occurs under these writing conditions, as evident from the microreflectivity data in Figs. 2(b) and 2(c).

2. LAS glasses and glass ceramics

LAS glasses are interesting because they can be partially crystallized in a well-controlled manner leading to transparent glass ceramics that provide a combination of properties that otherwise cannot be achieved. One such property of LAS glass ceramics is their low/zero coefficient of expansion. Using the 1-kHz repetition rate femtosecond laser we investigated laser-induced refractive index modification in Foturan®, Zerodur®, and Robax® before and after ceramization (heat treating). We show that positive refractive index changes of up to 1.5×10^{-3} can be generated in these glasses while the induced index changes are negative upon their ceramization.

Foturan® is a photosensitive glass that can be structured with light for a variety of applications in micro-optic and biotechnologies. 3D embedded structures such as micro-optical components, microfluidic channels, buried gratings, and waveguides have been fabricated.[5,18,21,22] The standard structuring process involves photo-oxidation of Ce^{3+} and reduction of Ag^{+} to the metallic state upon exposure to UV/IR light.[21] A subsequent two-step thermal treatment leads to agglomeration of the silver atoms, which then act as crystallization seeds for segregation of crystalline phase of Li–metasilicate. Presence of embedded metallic nanoparticles in a dielectric medium changes the refractive index.

Figure 3 shows that it is possible to directly fabricate buried waveguides with a femtosecond laser without any thermal treatment. Refractive index profile of the waveguide is shown along with a microscope image of the waveguide structure in the inset. In contrast, with the experiments with UV lasers,[23] no discoloration of the samples was observed. These results indicate that a different mechanism is responsible for femtosecond structuring. Some of the possible mechanisms are discussed later.

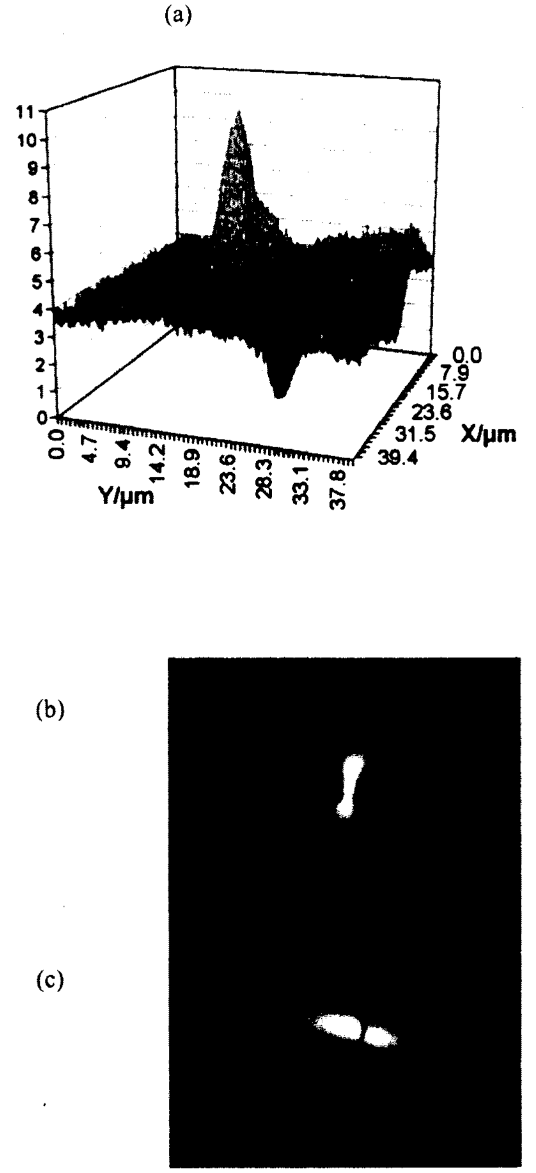

FIG. 4. (a) Measured 3D-RNF scan (relative values) in glassy Robax®, (b) microscope images of a waveguide cross section in glassy, and (c) ceramized Robax®. Laser parameters are 80 fs and 1 KHz.

Similar results were obtained for Zerodur® and Robax® glasses, however the achievable positive index change is an order of magnitude smaller than in Foturan®. Figures 4(a) and 4(b) show a 3D RNF scan and microscope image of the waveguide cross section, respectively, in glassy Robax® in-

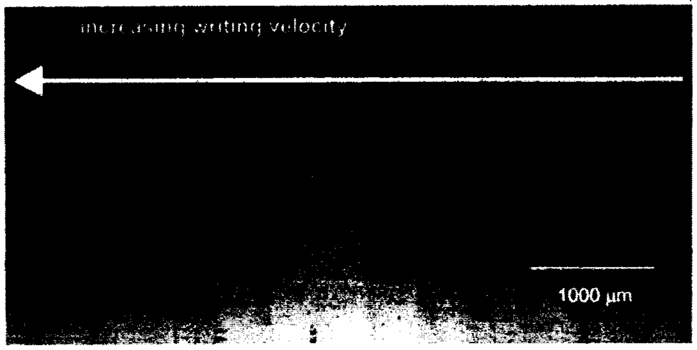

FIG. 5. Microscope image of waveguide cross sections in bismuth silicate glass at different writing speeds. Laser parameters are 80 fs and 1 kHz.

dicating a positive refractive index change. Upon ceramization of Robax®, the laser-induced refractive index change is negative. Figure 4(c) shows the microscope image of a waveguide cross section with negative index change in the center with positive side lobes in Robax® ceramic.

C. Heavy-metal oxide glasses

These glasses possess large nonresonant nonlinear refractive indices making them ideal materials for photonics applications like all-optical switching devices.[24] They contain ~70–80 wt % of heavy-metal cations like Pb and Bi which are not just network modifiers but actually play a role as network formers. The large nonlinear refractive index of these glasses is attributed to the hyperpolarizability of the constituent metal ions. We investigated laser-induced dielectric modification of lead–silicate SF57 and bismuth–silicate glasses with 100- and 1-kHz femtosecond laser systems, respectively. In lead–silicate glass SF57, microreflectivity measurements showed a uniform negative refractive index change of $\Delta n < -0.003 \pm 0.0002$ under the chosen writing conditions. However, due to poor chemical stability this glass tends to form surface films due to polishing and handling, which could have affected the measurement. The measured waveguide losses are 9 dB/cm at 633 nm, independent of translation speed. Also, the modified areas showed low etching selectivity for AFM measurements. Experiments with lower repetition rate also showed negative index change at low intensities. At higher laser intensities we observed destruction rather than the formation of smooth structures.

In bismuth–silicate glass not only the laser-induced index changes are negative, but also cracks and double core structures are formed for increased writing velocities >200 μm/s, as shown in Fig. 5.

D. Other glasses

1. Lanthanum–borate glass

This glass and the systems derived from it have a very high refractive index and can be host materials for optically active rare-earth ions. The femtosecond laser-induced refractive index modification in this glass is very weak. Figure 6(a) shows the optical microscope image of the cross section of the modified structure in the plane of the beam direction (perpendicular to the translation direction). As seen from the figure, the modification follows the laser beam waist all the way from the top surface. In comparison, in other glasses that are studied the modification is limited to the focal volume. The difference is most likely due to a color-center formation via a low-order interaction with the laser light. The color-center formation is indicated by bleaching after annealing at the moderately low temperature of 140 °C [Fig. 6(b)]. Others have reported that Raman spectra in borate glass suggest crystalline formation around the focal spot under certain irradiation conditions.[25]

2. SCHOTT IOG-1

This glass is a sodium–aluminum–phosphate glass developed for use in fabrication of active waveguide structures by ion exchange. It can be doped with optically active rare-earth ions such as erbium and ytterbium leading to the development of monolithic waveguide laser.[26] Microreflectivity

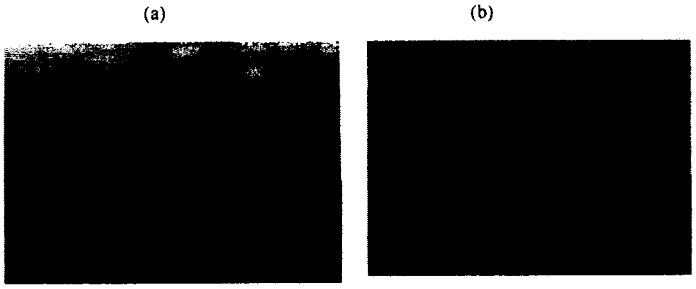

FIG. 6. Color centers in lanthanum–borate glass upon irradiation with 50 fs, 100-KHz femtosecond laser observed under microscope (a) before and (b) after annealing at 140 °C.

measurements on femtosecond laser-modified structures indicate a nonuniform index change. The accuracy of this measurement would have been affected by polish-induced topography (up to 35 nm, increasing with decreasing translation speed and independent of the writing angle) that was observed with AFM. Also, selective etching is not observed in the modified areas even after hours of etching. The measured losses are 12 dB/cm under the chosen writing conditions conforms to the microreflectivity measurements. Indeed, these results and the results of structuring with 1 kHz support the ones published in Ref. 27, where waveguides fabricated in IOG-1 glass showed a negative index change in the center and waveguiding in the outer regions possibly due to stress. Additionally, structuring the fluorophosphate glass LG 810 with a 1-kHz laser also produced negative index changes.

IV. DISCUSSION

The mechanisms of femtosecond laser-induced refractive index changes in glasses are not clear. However, it is known that the interaction proceeds through a nonlinear, multiphoton absorption of energy only in the focal volume of the laser beam. This is because most glasses do not absorb near-infrared light (800 nm) through a linear single-photon process. Upon absorption of laser energy, free electrons are produced by multiphoton ionization of the glass matrix. This is a deterministic process and eliminates the need for presence of impurities or other defects in glass to produce the seed electrons. The short pulse duration ensures that there is no time for coupling of electron energy to the surrounding lattice resulting in a localized energy deposition and plasma formation.[9]

In fused silica, the refractive index changes in low pulse energy regime can be attributed to the structural rearrangement of glass upon laser irradiation.[28,29] The structural network typically consists of a predominantly large number of five- and six-fold ring structures.[29] Micro-Raman spectroscopy of the laser-irradiated region revealed that some of the bonds are broken and subsequent structural rearrangement results in an increased number of three-and four-fold ring structures.[29] This is accompanied by a decrease in a Si–O–Si bond angle leading to the densification of glass. When the pulse energy is high, a different mechanism sets in. After the formation of localized plasma, a microexplosion occurs due to high pressures caused by an increase in temperature in a confined volume of the material. This results in shock waves that are responsible for the localized modification of glass forming a void or less dense material surrounded by densified material.[30]

The presence of network modifiers in multicomponent glasses makes it more difficult to understand the mechanisms of laser-induced dielectric modification. There is no single mechanism that can explain the observed results in multicomponent glasses. Microexplosion within the material could be one such mechanism that can lead to reduction of density and thus a negative index change in the center of the modified region, often with positive side lobes due to stress. The negative index change has been observed in fused silica and was attributed to laser-induced birefringence.[31,32] However, the microexplosion mechanism cannot be generally extended to aluminum–silicate glass such as 8261 where positive index change was observed. It also fails to explain the uniform negative index change observed in BK7.

Migration of network modifiers in multicomponent glasses could also lead to the changes in refractive index. Alkali migration is well understood in the context of an ion-exchange process that has been extensively used to fabricate waveguides in glass.[33] In the ion-exchange process, highly mobile sodium ions are exchanged with monovalent alkali ions such as Li^+, Cs^+, K^+ or Tl^+, and Ag^+ yielding a positive change in the refractive index. In alkali containing aluminum–silicate glasses, it is possible for the alkali ions to migrate from a laser-irradiated region to the surrounding areas. For example, migration of smaller lithium ions can lead to reduction in density and hence refractive index, while migration of highly polarizable silver ions also reduces the refractive index.

Migration of lithium ions might explain the drastic change in the refractive index from being positive to negative in alkali-free (8261) and alkali containing aluminum–silicate glasses. However, we observe a positive refractive index change in LAS glasses such as Foturan®, Zerodur®, and Robax®. In these glasses silver ions can play a significant role in the refractive index modification process. To test the migration mechanism we irradiated an ion-exchanged aluminosilicate glass where 20 wt % of sodium has been completely exchanged with silver. As silver is very mobile, the observed index change in this glass should be dominated by ion migration. As expected we observed a negative index change in such a glass. This is contrary to what has been observed in LAS glasses suggesting that ion migration is not the mechanism of refractive index modification.

LAS glasses are unstable upon thermal treatment, so besides density changes and ion migration, segregation of microcrystallites, such as high quartz solid solution or Li–metasilicate, could be involved in the modification mechanism. As high quartz solid solution is denser than the residual glass, the mechanism of laser-induced refractive index modification in LAS-type glasses and glass ceramics (polycrystalline solids prepared by controlled heat treatment of glasses resulting in nucleation and crystallization of various crystalline phases) could be local ceramization or destruction of the crystallites, respectively. The results of Foturan® corroborate this model as Li–metasilicate also has a higher refractive index than the surrounding material.

Foturan® has been specially developed for photostructuring with UV light in which a redox reaction between Ag^+ and Ce^{3+} ions ($Ag^+ + Ce^{3+} \rightarrow Ag + Ce^{4+}$) forms metallic particles in the irradiated areas. After heat treatment, crystallization occurs as a result of metal colloids.[34,35] In the case of femtosecond laser structuring where the light wavelength is nonresonant with glass absorption it has been shown that photoreduction of silver is possible even in the absence of Ce^{3+} and that Ce^{3+} ions do not take part in the photoreaction.[34,35] However, heat treatment is essential for crystallization that leads to an increase in refractive index.

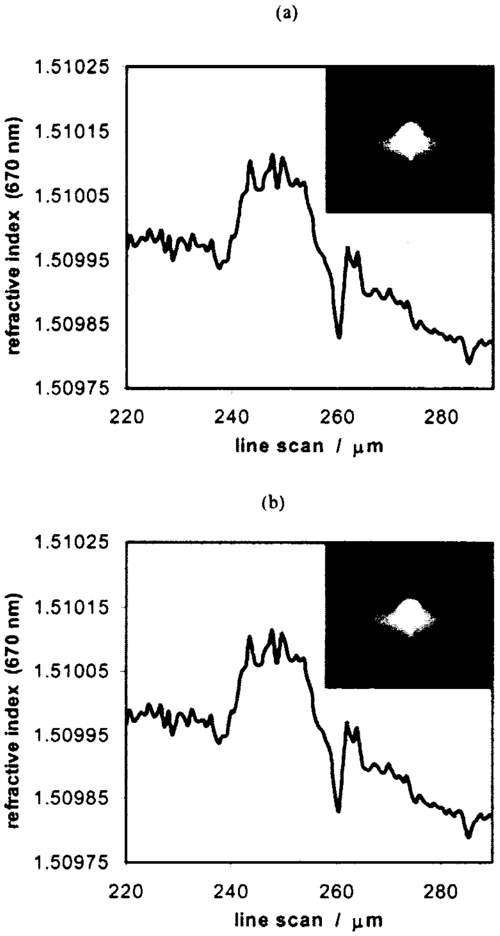

FIG. 7. Measured RNF scan of a waveguide in Foturan® variations with (a) reduced SiO_2 content and (b) free of silver. Insets show microscope images of the waveguide cross sections.

Contrary to this, in our experiments we observed a positive femtosecond laser-induced refractive change without any thermal annealing.

To gain insight into the index modification mechanism, various Foturan®-type glasses have been prepared, containing no Ag^+, no Ce^{3+}, or none of both ions as well as a melt with the SiO_2 content reduced by about 15% (by increasing the Al_2O_3 and B_2O_3 content). Figure 7 shows two exemplary RNF line scans of the end faces of femtosecond-written waveguides in Foturan®-type remelts with reduced SiO_2 content and no silver ions, respectively. All Foturan®-type remelts exhibited positive refractive index change upon structuring with 800-nm light. At 800 nm, it has been shown that there is no crystallization in silver-free Foturan®.[34,35] The fact that silver-free Foturan® shows a positive index change in our experiments indicates that a different mechanism is responsible.

If crystallization could already be initiated by a femtosecond irradiation, Ag/Ce-containing sodium-aluminum-silicate (NAS) glasses should produce negative index changes as NaF has a lower index than the residual glass (1.32 and 1.49, respectively). However, in our experiments we observed a positive refractive index change in such glasses. It is further assumed that nonbonding oxygens (NBOs) take the role of electron donors in the photoreaction $Ag^+ + NBO \rightarrow Ag + NBO^+$. This result was also confirmed by our multiphoton resonance experiments with 620 and 960 nm. Both the silver-free Foturan® variation as well as the reduced-SiO_2 variation show negative index changes with intense positive side lobes.

V. CONCLUSION

In summary, we have presented an extensive study on femtosecond laser-induced refractive index modification in a wide variety of multicomponent glasses from SCHOTT AG. Except for some aluminum-silicate glasses all other investigated glasses exhibited a negative refractive index change upon laser irradiation. We find the process is highly glass composition dependent. The modification in different glasses can result in uniform positive or negative or nonuniform refractive index changes under the same writing conditions. In addition, a single glass under different irradiation conditions can show negative or positive index changes. Further, the shape of the index profile strongly varies with changing parameters. This makes refractive index profiling imperative for each glass composition under a wide range of writing conditions. Further experiments on elemental analysis of irradiated and unirradiated glass by energy dispersive spectroscopy would provide insight into the migration mechanism. Glasses with negative refractive index modification can be useful in a variety of applications, such as precursors for microfluidic channels and photonic crystals, as well as for writing depressed-index-core photonic devices, such as doughnut-shape waveguides.[36]

ACKNOWLEDGMENT

The authors wish to acknowledge Professor Riedle and his group at the LMU Munich for performing the multiphoton resonance experiments in LAS glasses.

[1] N. H. Rizvi, RIKEN Rev. **50**, 107 (2003).
[2] H. Lubatschowski *et al.*, RIKEN Rev. **50**, 113 (2003).
[3] K. M. Davis, K. Miura, N. Suguimoto, and K. Hirao, Opt. Lett. **21**, 1729 (1996).
[4] A. M. Streltsov and N. F. Borelli, Opt. Lett. **26**, 42 (2001).
[5] Y. Cheng, K. Sugioka, K. Midorikawa, M. Masuda, K. Toyoda, M. Kawachi, and K. Shihoyama, Opt. Lett. **28**, 1144 (2003).
[6] A. Zumbush, G. R. Holtom, and X. S. Xie, Phys. Rev. Lett. **82**, 4142 (1999).
[7] R. S. Taylor, C. Hnatovsky, E. Simova, D. M. Rayner, V. R. Bhardwaj, and P. B. Corkum, Opt. Lett. **28**, 1043 (2003).
[8] E. N. Glezer, M. Milosavljevic, L. H. Huang, R. J. Finlay, T. H. Her, J. P. Callan, and E. Mazur, Opt. Lett. **21**, 2023 (1996).
[9] X. Liu, D. Du, and G. Mourou, IEEE J. Quantum Electron. **33**, 1706 (1997).
[10] Y. Bellouard, A. Said, M. Dugan, and P. Bado, Opt. Express **12**, 2120 (2004).
[11] C. B. Schaffer, A. Brodeur, J. F. Garcia, and E. Mazur, Opt. Lett. **26**, 93 (2001).
[12] K. Miura, J. Qiu, H. Inouye, and T. Mitsuyu, Appl. Phys. Lett. **71**, 3329 (1997).
[13] K. Miura, J. Qiu, T. Mitsuyu, and K. Hirao, J. Non-Cryst. Solids **256–257**, 212 (1999).
[14] D. Homoelle, S. Wielandy, A. Gaeta, N. F. Borelli, and Ch. Smith, Opt.

Lett. **24**, 1311 (1999).
[15] A. M. Streltsov and N. F. Borrelli, J. Opt. Soc. Am. B **19**, 2496 (2002).
[16] R. Osellame, S. Taccheo, G. Cerullo, M. Maragoni, D. Polli, R. Ramponi, P. Laporta, and S. De Silvestri, Electron. Lett. **38**, 964 (2002).
[17] C. Florea, K. A. Winick, Y. Sikosky, A. Said, and P. Bado, Conference on Lasers and Electro-Optics, CLEO'2000, San Francisco, CA, 7–12 May 2000, Conf. Digest, paper #CMX5, pp. 128.
[18] M. Masuda *et al.*, Appl. Phys. A: Mater. Sci. Process. **76**, 857 (2003).
[19] S. Garcia Blanco, C. Hnatovsky, R. S. Taylor, and J. S. Aitchison, Appl. Phys. Lett. **85**, 1314 (2004).
[20] R. S. Taylor, C. Hnatovsky, E. Simova, D. M. Rayner, M. Mechandale, V. R. Bhardwaj, and P. B. Corkum, Opt. Express **11**, 775 (2003).
[21] Y. Cheng, K. Sugioka, M. Masuda, K. Shihoyama, K. Toyoda, and K. Midorikawa, Opt. Express **11**, 1809 (2003).
[22] S. Ho, P. R. Herman, Y. Cheng, K. Sugioka, and K. Midorikawa, Conference on Lasers and Electro-Optics, CLEO'2004, San Francisco, CA, 16–24 May2004, Conf. Digest, paper #CThD6, pp. 215.
[23] L. G. Glebov, C. DePriest, O. M. Efimov, S. Grantham, and M. Richardson, Proceedings of 18th International Congress on Glass, San Francisco, CA, 5–10 July, 1998, paper #C10, pp. 17
[24] S. R. Friberg and P. W. Smith, IEEE J. Quantum Electron. **23**, 2089 (1987).
[25] B. Yu, B. Chen, X. Yang, J. Qui, X. Jiang, C. Zhu, and K. Hirao, J. Opt. Soc. Am. B **21**, 83 (2004).
[26] H. Suche, I. Baumann, D. Hiller, and W. Sohler, Electron. Lett. **29**, 1111 (1993).
[27] J. W. Chan, Th. R. Huser, S. H. Risbud, J. S. Hayden, and D. M. Krol, Appl. Phys. Lett. **82**, 2371 (2003).
[28] J. W. Chan, T. Huser, S. Risbud, and D. M. Krol, Opt. Lett. **26**, 1726 (2001).
[29] J. W. Chan, T. R. Huser, S. H. Risbud, and D. M. Krol, Appl. Phys. A: Mater. Sci. Process. **76**, 367 (2003).
[30] E. N. Glezer and E. Mazur, Appl. Phys. Lett. **71**, 882 (1997).
[31] E. Bricchi, B. G. Klappauf, and P. G. Kazansky, Opt. Lett. **29**, 119 (2004).
[32] V. R. Bhardwaj, P. B. Corkum, D. M. Rayner, C. Hnatovsky, E. Simova, and R. S. Taylor, Opt. Lett. **29**, 1312 (2004).
[33] S. I. Najafi, *Introduction to Glass Integrated Optics* (Artech House Inc., Boston, 1992).
[34] Y. Kondo, K. Miura, T. Suzuki, H. Inouye, T. Mitsuyu, and K. Hirao, J. Non-Cryst. Solids **253**, 143 (1999).
[35] Y. Kondo, T. Suzuki, H. Inouye, K. Miura, T. Mitsuyu, and K. Hirao, Jpn. J. Appl. Phys., Part 2 **37**, L94 (1998).
[36] A. M. Ljungstroem and T. M. Monro, Opt. Express **10**, 230 (2002).

JOURNAL OF APPLIED PHYSICS 98, 013517 (2005)

High-resolution study of photoinduced modification in fused silica produced by a tightly focused femtosecond laser beam in the presence of aberrations

C. Hnatovsky[a] and R. S. Taylor
Institute for Microstructural Sciences, National Research Council, M23A, 1200 Montreal Road, Ottawa, K1A 0R6, Canada

E. Simova, V. R. Bhardwaj, D. M. Rayner, and P. B. Corkum
Steacie Institute for Molecular Sciences, National Research Council, 100 Sussex Drive, Ottawa, K1A 0R6, Canada

(Received 18 February 2005; accepted 5 May 2005; published online 7 July 2005)

An ultrahigh-resolution (20 nm) technique of selective chemical etching and atomic force microscopy has been used to study the photoinduced modification in fused silica produced at various depths by tightly focused femtosecond laser radiation affected by spherical aberration. We demonstrate that shapes of the irradiated zones near the threshold for modification can be predicted by taking proper account of spherical aberration caused by the refractive index mismatched air–silica interface. We establish a depth dependence of the pulse energy required to initiate modification and characterize the relationship between numerical aperture of the writing lens and practically achievable writing depth. We also show that spatial characteristics of the laser-modified zones can be controlled by a specially designed focusing system which allows correction for a variable amount of spherical aberration. © *2005 American Institute of Physics*.
[DOI: 10.1063/1.1944223]

I. INTRODUCTION

Femtosecond laser dielectric modification (FLDM) is recognized as a promising platform technology for three-dimensional (3D) photonics. There have been several examples of the production of waveguides,[1] simple passive devices, such as directional couplers[2] and splitters,[3] 3D optical data storage,[4] and even active laser gain components.[5] In addition, a combined approach of FLDM followed by chemical etching can produce channels inside glasses allowing the fabrication of 3D microfluidic devices.[6,7] The 3D capability originates from the nonresonant interaction of femtosecond laser light with transparent media. The intensity required for this highly nonlinear process is achieved by focusing the laser beam tightly. By keeping the pulse short the pulse energy can be low and modification can be controlled and localized on the micrometer scale.[8] The material surrounding the focal volume remains unaffected by the light passing through it, nominally allowing structures to be written at any depth in 3D fashion.

In practice FLDM is complicated by the presence of a dielectric interface between materials of mismatched refractive indices (e.g., air and the material to be processed) in the optical path of the focused laser beam. The interface introduces an aberration distorting the wave front of the converging spherical wave and causes significant spreading of the intensity distribution along the beam propagation direction near the focus. This effect is well known and has been extensively studied both theoretically and experimentally in optical microscopy,[9–11] production of 3D optical data storage in two-photon bleaching polymers,[12] laser microsurgery,[13] and optical trapping.[14,15] However, in femtosecond-laser microfabrication in glasses the role of the intensity distribution near the laser focus in shaping the photoinduced modification is usually underestimated and only recently has begun to be clarified. Working with a very high numerical aperture (NA=1.35) oil immersion objective at intensities above the modification threshold, Marcinkevičius *et al.* demonstrated an increase in the size and distortion of the shape of the modified regions when the refractive index of the sample was slightly different from the value for which the focusing objective was designed.[16] They also remarked on the depth dependence of the modification threshold and on the appearance, at intensities well above this threshold, of secondary modification associated with the elongation of the focus. The observations were made over a 100-μm depth range using confocal microscopy.

In this report we address the effects of spherical aberration on FLDM carried out through a large index change air–silica interface near the photoinduced modification threshold. This regime is important for controlled refractive index modification at the depths required for true 3D optical wiring and device fabrication. We use an ultrahigh spatial resolution (20 nm) technique to image submicron features of FLDM at depths up to 1.5 mm. We demonstrate a significant depth dependence and show through simulations that spherical aberration due to a planar air–silica interface accounts in general for the shapes and positions of the modified zones. We show that spherical aberration determines the variation of the threshold pulse energy for FLDM as a function of the focusing depth. We also demonstrate that the shape and size of the femtosecond-radiation modified zones in fused silica can be

---

[a] Electronic mail: cyril.hnatovsky@nrc.ca

controlled by focusing the laser beam with a *dry* (strong index mismatch) high numerical aperture (NA=0.75) long working distance (up to 2.2 mm) microscope objective allowing variable cover glass correction (up to 1.5 mm). This is important for 3D femtosecond-assisted fabrication of optical waveguides and microfluidic devices at depths varying on a millimeter scale. Dry, specially corrected objectives become the preferred tool to perform these tasks since at such depths the use of high NA immersion optics is inconvenient due to the necessity of manipulating submerged samples and the limited correction range of the commercially available designs. Understanding the limitations and possible ways to improve the performance of dry optics to achieve the required spatial characteristics and high spatial resolution of FLDM is a significant issue and will be discussed in this paper.

II. EXPERIMENT

Regeneratively amplified Ti:sapphire laser pulses (70-fs full width at half maximum after the compressor, 100-kHz repetition rate, central wavelength $\lambda=800$ nm) were spatially filtered and focused inside a Suprasil II synthetic quartz glass substrate with an infinity-corrected Zeiss LD Plan Neofluar® (63×, NA=0.75) microscope objective allowing adjustable compensation for spherical aberration caused by cover glass of varying thickness (0–1.5 mm) and refractive index of $n=1.5$. Lines of modification were produced by moving the sample perpendicular to the direction of propagation of the laser beam at 100 μm/s resulting in an effective exposure of ≈ 1000 shots/μm of travel. Laser polarization was along the translation direction.

To map the cross-sectional morphology of the modified zones the samples were cut in two pieces perpendicular to the translation direction. The inside surfaces were polished and characterized using selective chemical etching [3 min in a 1% aqueous solution of hydrofluoric acid (HF)] followed by atomic force microscopy (AFM). This technique maps the structural change that is associated with the refractive index change induced by FLDM and has a spatial resolution of 20 nm.[17]

In the first set of experiments the correction collar of the microscope objective was set at its no correction position and lines of modification were written at different depths. To determine the threshold pulse energy for modification E_{th}, for each depth the pulse energy E_p was varied from under threshold to above threshold values in steps of 5 nJ for focusing depths up to 550 μm and in steps of 10 nJ for a deeper focusing. After irradiation the sample was examined using a bright-illumination high-resolution optical microscope. E_{th} was determined as the minimum pulse energy measured after the objective at which a visible continuous line of material modification was produced. The observations showed that the transition from no modification to a continuous modification is achieved abruptly by varying E_p usually by less than 5% around the E_{th}. The threshold determined in this way is $\approx 30\%$ above the threshold for observation by AFM/etching under the same writing conditions (see below).

In the second set of experiments E_p was set slightly higher (40 nJ) than the previously obtained threshold of 30 nJ at 10-μm subsurface and FLDM was performed at different depths with the correction collar adjusted to compensate for spherical aberration. The "safety factor" in the pulse energy was introduced to compensate for possible inaccuracy in the correction collar settings.

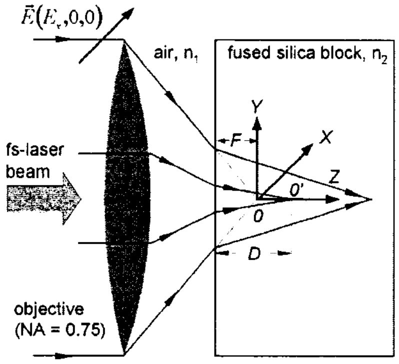

FIG. 1. A schematic of the experimental layout.

III. RESULTS AND DISCUSSION

To model the intensity distribution in the limit of no absorption near the focus we adopt the theory of Török *et al.* based on the vectorial generalization of the Debye integral for the case of the diffraction of a plane monochromatic linearly polarized electromagnetic wave focused through a planar dielectric interface.[18] Other theoretical approaches addressing this problem give very similar results.[19,20] In our analysis the Debye integral was calculated only for the central wavelength ($\lambda=800$ nm) of the laser radiation. The effect of spectral broadening on the focused intensity distribution becomes noticeable only for very short (<10 fs) laser pulses.[21,22] However, even in this extreme case the changes occur mainly in the fine structure of the intensity distribution, whereas the main features remain essentially intact. We also assume that the objective obeys Abbe's sine condition[23] and the illumination is homogeneous as the width of the incident Gaussian beam at $1/e^2$ level is two times wider than the entrance pupil of the objective lens.

Figure 1 shows a sketch of the focusing geometry used in the experiments. The origin of the coordinate system O is where the focus is located in the absence of the dielectric interface. O' which denotes the position of the paraxial focus, i.e., the focus produced by the central area of the focusing lens, is located at a distance of $D \approx (n_2/n_1)F$ from the air–silica interface, where n_1 and n_2 designate the refractive indices of air ($n_1 \approx 1$) and fused silica, respectively. The electric vector of the incident wave is aligned along the X axis.

Figure 2 shows the calculated axial laser intensities I as a function of the focusing depth D. As D (taken as the position of the main maximum with respect to the interface which approximately coincides with the paraxial focus[19,24]) increases, the following trends in the axial intensity distributions are observed: (i) a dramatic drop in the magnitude of the main maximum, (ii) relative growth of the secondary maxima with a gradual increase of the separation between

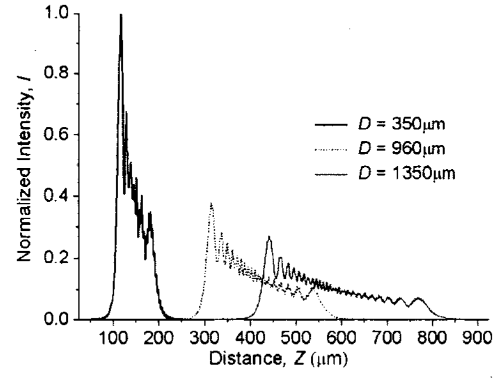

FIG. 2. Normalized axial intensity distributions calculated for focusing inside fused silica at different depths with a NA=0.75 lens through an air/silica (n_2=1.453 at λ=800 nm) interface.

the main and second maxima, and (iii) spreading of the distribution along the beam propagation over distances exceeding many times the unaberrated confocal parameter approximated by $4n_2\lambda/\mathrm{NA}^2$, where λ is the wavelength in vacuum and NA denotes the numerical aperture of a dry objective.[23] In Fig. 2 the severity of the spatial distortion is apparent even for a moderate writing depth of 350 μm, where the intensity distribution spreads from the unaberrated value of ≈8.5 μm to 110 μm.

Figure 3 compares the computed maximum axial intensity (corresponding to the peak values of the first maxima) $I_{\max}$ and the experimentally obtained E_{th} values as a function of D. When $I_{\max}$ drops with D due to the distortion of the focal volume by the aberration introduced by the dielectric interface, the pulse energy must be raised in compensation yielding the inverse correlation between $I_{\max}$ and E_{th} shown in the figure. E_{th} for an uncorrected 0.75-NA objective ranges by over an order of magnitude on going from a focusing depth of 10 μm (E_{th}=30 nJ) to 1400 μm (E_{th}=530 nJ). The correspondence with theory allows us to predict how spherical aberration limits performance at other NA's. The characteristic focusing depth $D_{1/2}$, at which $I_{\max}$ reduces to half of its maximum value, was empirically determined to be inversely proportional to $\approx(\mathrm{NA})^{9/2}$ of the focusing lens.

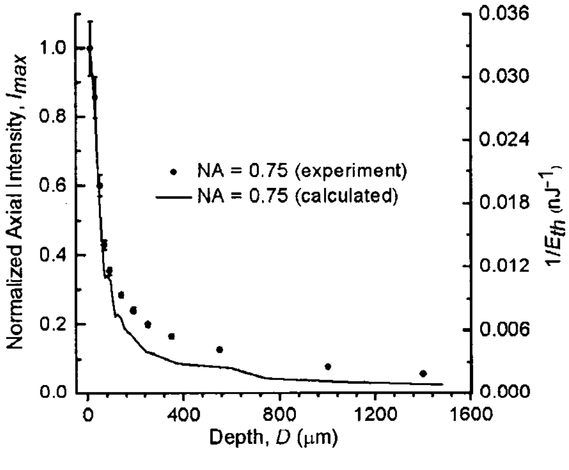

FIG. 3. Calculated maximum axial intensity $I_{\max}$ as a function of focusing depth for NA=0.75 (line). $I_{\max}$ corresponds to the first peak of the intensity distribution for each depth and is normalized to unity at the air/silica interface. Also shown are experimentally determined threshold energies (●) for different depths with a NA=0.75 objective at which the modified structures are observed. The ordinate on the left corresponds to the calculated intensities while the ordinate on the right shows the reciprocal of the experimental threshold energies.

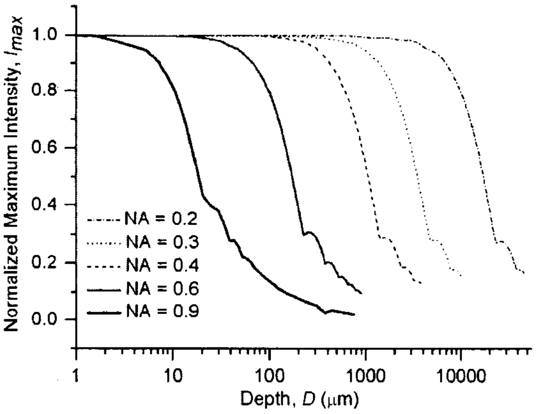

FIG. 4. Calculated maximum axial intensity $I_{\max}$ as a function of focusing depth for different NA's.

Figure 4 shows the calculated drop of $I_{\max}$ with depth for objectives with different NA's. With a dry objective of NA =0.2 it is possible to write at depths of over 10 mm without concern for the intensity drop due to spherical aberration, whereas dry writing with a 0.9-NA objective can be restricted to a few tens of microns under the surface unless the laser power is raised dramatically in compensation or the writing is done at fixed depths where the optics are corrected.[25]

The cross sections of the modified zones written at three different depths with the uncompensated lens are shown in Fig. 5(a). They are compared with intensity distributions in the YZ plane, I_{YZ}, calculated at the corresponding depths. The calculated intensity distributions are arranged so that the main maximum is centered on the major modified area.

In the focal volume, we expect that modification starts upstream of the paraxial focus due to nonlinear absorption switching on at the point where the axial intensity reaches I_{th}. In general, the absorption limits the delivered intensity close to I_{th} up to the focal plane and below it thereafter.[26] An aberrated beam feeds energy around this region extending the modified zone forward. Taking into account the sharp rise in the aberrated intensity distribution on the focusing optics side (see Fig. 2) and the near-threshold pulse energies used in the experiment, the location of the modified zones should be close to the paraxial focus.

At D=350 μm with E_p=160 nJ the AFM technique detects a single structure, whereas at D=960 μm with E_p =370 nJ and D=1350 μm with E_p=520 nJ double structures consisting of the main component and a secondary structure separated by 21 and 26 μm from center to center, respectively, are observed. The corresponding computed values are 21.5 and 25 μm, in good agreement with the experiment. No signature of the tertiary maxima at D=960 and 1350 μm and

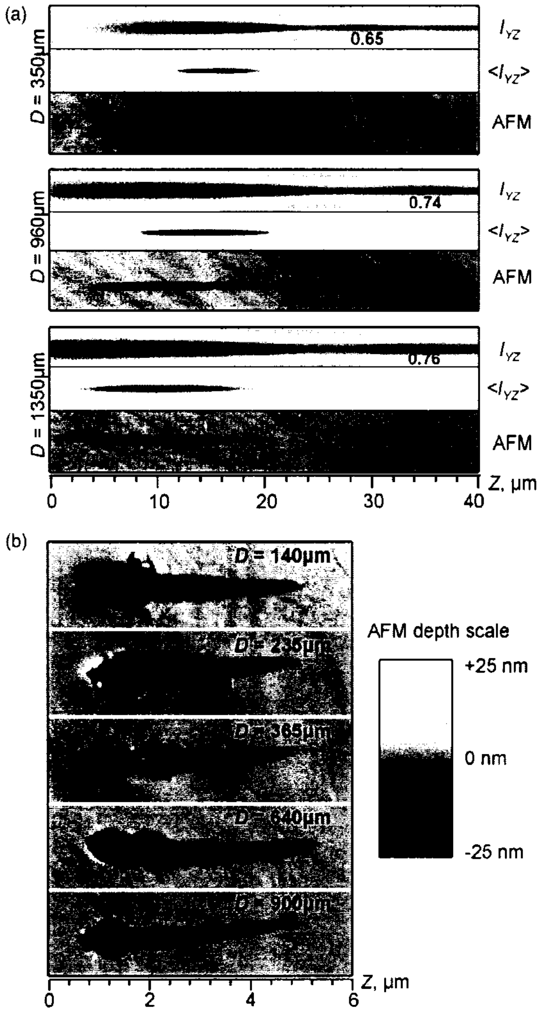

FIG. 5. (a) Intensity distributions with the corresponding AFM images in the YZ plane for the uncorrected focusing at three different depths. At each depth D the top plot is the calculated intensity distribution. The peak intensities of the first maxima are normalized to unity (black level on the grayscale). The middle plot, labeled $\langle I_{YZ}\rangle$, is the same distribution with all values below 70% of the maximum intensity filtered out. The bottom plot in each panel is an AFM image of the modified region. The dark regions on the AFM scans correspond to selectively etched femtosecond-laser-modified zones. The pulse energy E_p is 160, 370, and 520 nJ for $D=350$, 960, and 1350 μm, respectively. All calculated intensity distribution plots show only the first two maxima. The number inside each plot indicates the magnitude of the second maximum as a fraction of unity. (b) AFM images of the modified regions with the corrected focusing. $E_p=40$ nJ for all depths. For (a) and (b), AFM depth scale is the same and light propagates from left to right.

secondary maxima at $D=350$ μm was revealed by either visual inspection or the AFM technique. This suggests that in these cases the peak I_{YZ} in the second maxima was just above threshold for $D=960$ and 1350 μm and below it for $D=350$ μm. From the calculated ratios of I_{YZ} at the first and second maxima [Fig. 5(a)], the peak I_{YZ} in the first maxima was approximately 30% above that threshold value.

For a spherically aberrated focus where the second intensity peak is above I_{th} we expect to see two modified zones separated by approximately the distance between the predicted maxima, as observed. A dynamic equilibrium between self-focusing and defocusing by the electron plasma generated by weakly focused femtosecond radiation can potentially lead to the formation of multiple modified zones along the laser beam propagation.[27] The role of self-focusing in our experiment is believed to be small since (i) the peak laser powers were generally less than the critical power for self-focusing in fused silica [4.3 MW at $\lambda=800$ nm (Ref. 25)] and (ii) tight focusing of the femtosecond beam obtained using a relatively high NA lens (NA=0.75) allowed the peak laser intensity to exceed the sharp threshold for nonlinear absorption ($\approx 1.1\times 10^{13}$ W cm^{-2} for fused silica[26]) thereby reducing the laser peak power below the critical power for self-focusing.

Raising E_p to the values at which the interpeak (or valley) intensity reaches the modification threshold will cause merging of the modified zones. The axial growth in both directions accompanied with lateral expansion would finally lead to an extensive modification which may stretch over many tens of microns along the beam propagation. Other researchers working with tightly focused femtosecond-laser beams reported similar axial stretching of the modified zones at a fixed depth below the fused silica surface.[28]

Our results on uncorrected focusing are also supported by the studies on the effect of spherical aberration caused by focusing optics on picosecond-laser-induced breakdown in gases,[29,30] where the observed distinct regions of intense ionization were associated with the main axial intensity peaks of the calculated diffraction patterns near the lens focus.

Figure 5(b) summarizes the results of the corrected focusing experiment. The structures written at different depths varying from 140 to 900 μm exhibit reproducible shapes and lengths of ≈ 4 μm, which is considerably less than the uncorrected lengths of ≈ 20 μm shown in Fig. 5(a). The progressive bending of the structures with D can be caused by off-axis aberrations introduced by nonperfect coaxial alignment of the lens groups inside the microscope objective. The misalignment may accumulate during the relative motion of the lens groups as the correction collar is adjusted for a deeper focusing. The high etching selectivity occurring on the top parts of the modified zones is due to the complex morphology developing at above threshold (×1.3) writing conditions.[31] The laser-pulse energy required for the onset of visible modification in fused silica for the corrected focusing at 900 μm is an order of magnitude lower than in the uncorrected case.

IV. CONCLUSIONS

In conclusion, we have demonstrated, using ultrahigh spatial resolution diagnostics, that the shapes and separations of femtosecond-laser-modified zones in fused silica can be correlated to aberrated intensity distribution in the focal volume of the focusing optics. This allows us to assess how spherical aberration limits the depth performance obtainable with any NA objective and to choose between using a high NA objective to write small features over a limited depth and a lower NA objective to produce larger features but over a greater depth. We also show that a dry microscope objective allowing adjustable compensation for spherical aberration can effectively control the threshold pulse energy and size of the modification. Structures as short as 4 μm can be written at depths of $\approx$1 mm with 0.75-NA optics. The diffraction limited writing deep in bulk material at a fixed near-threshold pulse energy by simply and potentially dynamically adjusting spherical aberration correction of the focusing objective is important for 3D optical data storage and fabrication of integrated photonic and microfluidic devices where the production of identical structures at widely different depths becomes a critical issue.

[1] K. M. Davis, K. Miura, N. Sugimoto, and K. Hirao, Opt. Lett. **21**, 1729 (1996).

[2] A. M. Streltsov and N. F. Borrelli, Opt. Lett. **26**, 42 (2001).

[3] D. Homoelle, S. Wielandy, A. L. Gaeta, N. F. Borrelli, and C. Smith, Opt. Lett. **24**, 1311 (1999).

[4] E. N. Glezer, M. Milosavljevic, L. Huang, R. J. Finlay, T.-H. Her, J. P. Callan, and E. Mazur, Opt. Lett. **21**, 2023 (1996).

[5] R. Osellame, S. Taccheo, G. Cerullo, M. Marangoni, D. Polli, R. Ramponi, P. Laporta, and S. De Silvestri, Electron. Lett. **38**, 964 (2002).

[6] A. Marcinkevičius, S. Juodkazis, M. Watanabe, M. Miwa, S. Matsuo, H. Misawa, and J. Nishii, Opt. Lett. **26**, 277 (2001).

[7] Y. Kondo, J. Qiu, T. Mitsuyu, K. Hirao, and T. Yoko, Jpn. J. Appl. Phys., Part 2 **38**, L1146 (1999).

[8] D. Du, X. Liu, G. Korn, J. Squier, and G. Mourou, Appl. Phys. Lett. **64**, 3071 (1994).

[9] S. F. Gibson and F. Lanni, J. Opt. Soc. Am. A **8**, 1601 (1991).

[10] S. Hell, G. Reiner, C. Cremer, and E. H. K. Stelzer, J. Microsc. **169**, 391 (1993).

[11] P. Török, S. J. Hewlett, and P. Varga, J. Microsc. **188**, 158 (1997).

[12] D. Day and M. Gu, Appl. Opt. **37**, 6299 (1998).

[13] A. Vogel, K. Nahen, D. Theisen, R. Birngruber, R. J. Thomas, and B. A. Rockwell, Appl. Opt. **38**, 3636 (1999).

[14] P. C. Ke and M. Gu, J. Mod. Opt. **45**, 2159 (1998).

[15] A. C. Dogariu and R. Rajagopalan, Langmuir **16**, 2770 (2000).

[16] A. Marcinkevičius, V. Mizeikis, S. Juodkazis, S. Matsuo, and H. Mizawa, Appl. Phys. A: Mater. Sci. Process. **76**, 257 (2003).

[17] R. S. Taylor, C. Hnatovsky, E. Simova, D. M. Rayner, M. Mehendale, V. R. Bhardwaj, and P. B. Corkum, Opt. Express **11**, 775 (2003).

[18] P. Török, P. Varga, Z. Laczik, and G. R. Booker, J. Opt. Soc. Am. A **12**, 325 (1995).

[19] S. H. Wiersma, P. Török, T. D. Visser, and P. Varga, J. Opt. Soc. Am. A **14**, 1482 (1997).

[20] A. Egner and S. W. Hell, J. Microsc. **193**, 244 (1999).

[21] K. M. Romallosa, J. Bantang, and C. Saloma, Phys. Rev. A **68**, 033812 (2003).

[22] M. Gu, *Advanced Optical Imaging Theory* (Springer, Berlin, 2000).

[23] M. Born and E. Wolf, *Principles of Optics* (Pergamon, London, 1989).

[24] S. H. Wiersma, T. D. Visser, and P. Török, Pure Appl. Opt. **7**, 1237 (1998).

[25] C. B. Shaffer, A. Brodeur, and E. Mazur, Meas. Sci. Technol. **12**, 1784 (2001).

[26] D. M. Rayner, A. Naumov, and P. Corkum, Opt. Express **13**, 3208 (2005).

[27] Z. Wu, H. Jiang, L. Luo, H. Guo, H. Yang, and Q. Gong, J. Opt. A, Pure Appl. Opt. **5**, 102 (2003).

[28] L. Sudrie, A. Couairon, M. Franco, B. Lamouroux, B. Prade, S. Tzortzakis, and A. Mysyrowicz, Phys. Rev. Lett. **89**, 186601-1 (2002).

[29] L. R. Evans and C. G. Morgan, Phys. Rev. Lett. **22**, 1099 (1969).

[30] J. M. Aaron, C. L. M. Ireland, and C. G. Morgan, J. Phys. D **7**, 1907 (1975).

[31] C. Hnatovsky, R. Taylor, R. Bhardwaj, E. Simova, D. Rayner, and P. Corkum, Long-Range Periodic Planar Nanostructures Produced in Glass by Femtosecond Laser Dielectric Modification, CLEO, Baltimore, Maryland, USA, 22–27 May 2005 (unpublished).

APPLIED PHYSICS LETTERS 87, 014104 (2005)

Pulse duration dependence of femtosecond-laser-fabricated nanogratings in fused silica

C. Hnatovsky[a)] and R. S. Taylor
Institute for Microstructural Sciences, National Research Council of Canada, 1200 Montreal Road, Ottawa, Ontario K1A 0R6, Canada

P. P. Rajeev, E. Simova, V. R. Bhardwaj, D. M. Rayner, and P. B. Corkum
Steacie Institute for Molecular Sciences, National Research Council of Canada, 100 Sussex Drive, Ottawa, Ontario K1A 0R6, Canada

(Received 21 April 2005; accepted 10 June 2005; published online 29 June 2005)

Femtosecond laser radiation tightly focused in bulk fused silica is used to generate self-ordered nanogratings when the sample is translated under the lens at constant speed. The nanogratings are preserved over a length scale of millimeters. We demonstrate that nanogratings are formed for all pulse durations tested, ranging from 40 to 500 fs, and that the pulse energy threshold for this phenomenon increases with decreasing pulse duration. We use high spatial resolution diagnostics based upon selective chemical etching followed by atomic force microscopy and scanning electron microscopy to reveal the morphology of the nanogratings. © *2005 American Institute of Physics*. [DOI: 10.1063/1.1991991]

Focused femtosecond (fs) laser radiation can induce highly localized permanent changes in the chemical and physical properties of transparent dielectrics allowing femtosecond laser dielectric modification (FLDM) to be used in fabrication of photonic[1,2] and microfluidic[3] components, optical storage,[4] and nanostructures.[5] Studies of fs-laser modified regions inside various glasses have identified different regimes as the light intensity at the focus is increased, viz. the production of: (i) smooth refractive index changes,[1] (ii) birefringent zones,[6] and (iii) microvoids (disruptions).[4] The birefringence induced by focused fs radiation is ascribed either to laser-induced stress,[7] or to the formation of self-ordered nanogratings of subwavelength periodicity orientated perpendicularly to the laser light polarization leading to anisotropic reflection.[8]

The nanogratings have been observed in the static focus of a fs-laser beam using backscattering scanning electron microscopy (SEM).[9] Recently, using the technique of selective chemical etching combined with SEM we have shown that, when long range structures are written by continuous motion of the sample under the laser focus, the polarization-dependent nanogratings maintain their periodicity over the entire writing range.[10]

In this letter we measure the pulse energy threshold for the formation of polarization-dependent self-ordered nanogratings in the moving focus [numerical aperture (NA) $=0.65$] of a fs-laser beam for pulse durations ranging from 40 to 500 fs. We demonstrate that the threshold for initiating nanogratings significantly increases with decreasing pulse duration. Using an ultrahigh spatial resolution technique of selective chemical etching combined with atomic force microscopy (AFM) (15 nm resolution)[11] and SEM (5 nm resolution) we also reveal transformations occurring in the morphology of the modified regions as pulse duration and energy are varied. SEM images of cleaved samples show that the nanograting plane thickness can be less than 5 nm and indicate that these well-defined planes are rather photoinduced nanocracks than layers of modified material. Our results enable optimization of the FLDM parameter space to fabricate high-quality nanogratings.

Prior research on the pulse duration dependence of FLDM has mainly been dedicated to establishing the material modification (or breakdown) threshold through observing front surface damage or detecting the plasma emission from the optical breakdown in the sample.[12–15] Those experiments were carried out in a weak focusing geometry and polarization effects were not considered. Study of the dependence of FLDM morphology in bulk material on pulse duration has been performed so far only for weakly focused beams ($\mathrm{NA}=0.08$) using optical microscopy and no evidence of nanogratings was found.[16]

A regeneratively amplified mode-locked Ti:sapphire laser operating at $\lambda=800$ nm with a minimum pulse duration of 40 fs and repetition rate of 100 kHz is used in the experiments. The linearly polarized Gaussian laser beam, spatially filtered and attenuated by a variable density filter, is tightly focused with a microscope objective (Nikon, Achromat, ×40, $\mathrm{NA}=0.65$) 100 μm under the surface of a fused silica sample (Suprasil II from Heraeus). The laser irradiation is carried out by translating the sample perpendicularly to the direction of propagation of the laser beam using a motorized X-Y micropositioning stage at 30 μm/s speed. The laser light is polarized perpendicularly to the writing direction. The sample moves by only 0.3 nm between consecutive laser shots at this repetition rate thus being irradiated by thousands of pulses per micron of travel.

The pulse duration is varied from 40 to 500 fs by adjusting the grating separation in the pulse compressor with a computer-controlled translation stage. Pulse characterization is performed by interferometric autocorrelation. The fs pulse temporal broadening due to group-velocity dispersion in the microscope objective is compensated by pre-chirping the laser pulse in the compressor. After laser irradiation the sample is cut in half, normal to the writing direction and the two inside surfaces are wet polished. The samples are then etched at room temperature in 1% by volume hydrofluoric acid or

---

[a)] Electronic mail: cyril.hnatovsky@nrc.ca

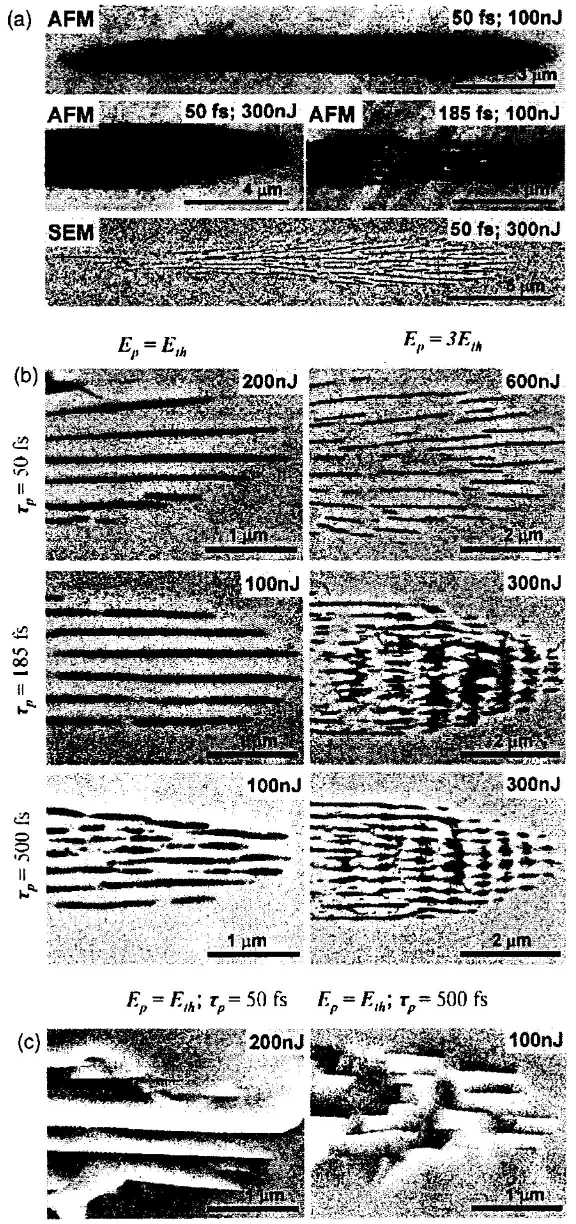

FIG. 1. Cross-sectional images of the modified regions: (a) AFM and SEM and (b) SEM on the etched sample (240 s in 1% HF); (c) SEM on the cleaved (unetched) sample. (b) and (c) show only the top portions of the modified regions. For SEM the samples are coated with 1.5 nm of Pt. Light propagates from right to left and is polarized perpendicularly to the writing direction and nanograting planes. Darker regions in AFM and SEM images correspond to deeper topography.

cleaved and cross-sectional images of the modified regions are obtained using AFM (Digital Instruments Dimension 3000, contact mode with silicon nitride probes) and SEM (Hitachi S-4700, secondary electron imaging). To avoid SEM imaging artifacts caused by surface charging, both etched and cleaved samples are coated with a 1.5 nm layer of Pt.

Figures 1(a)–1(c) present AFM and SEM images of the cross-sectional morphology of fs-laser modified regions for various pulse durations, τ_p, and pulse energies, E_p, obtained on selectively etched as well as cleaved samples. The two imaging techniques are complimentary. SEM increases contrast of abrupt deep topographic changes but is almost insensitive to smooth relief on a nanometer scale which is easily mapped by AFM. On the other hand, analysis of AFM images becomes difficult due to loss of contrast when smooth topographic background masks very narrow (<20 nm) and deep (>50 nm) features whose actual depth is underestimated in this AFM-probe limited regime.

For short $\tau_p(<150$ fs) with the laser pulse energy above the material modification threshold ($E_p \approx 50$ nJ), AFM reveals well-defined uniformly etched regions of smooth modification [Fig. 1(a); AFM, 50 fs, 100 nJ]. This smooth modification has been associated with refractive index changes on the order of 5×10^{-3}.[11] At higher pulse energies (≥ 150 nJ) a second τ_p-dependant threshold for nanograting formation, $E_{\mathrm{th}}(\tau_p)$, is reached. The grating pattern is embedded within and covers the full extent of the smooth modification [Fig. 1(a); AFM and SEM, 50 fs, 300 nJ]. The quasiperiodicity of the nanogratings (250 nm on the average) is independent of τ_p and E_p within the studied range. The etch rate of the interplane modification, as measured by the depth of the AFM image, is $\approx 70\%$ of that of the uniform modification obtained just below the nanograting threshold.

For longer $\tau_p(\geq 185$ fs), however, nanogratings are observed at a lower threshold $E_{\mathrm{th}}(\tau_p)=75-100$ nJ [Fig. 1(a); AFM, 185 fs, 100 nJ also shown in Fig. 1(b)]. For these pulse durations no material modification is detected either by optical microscopy or AFM/SEM at $E_p=50$ nJ. This suggests that the E_p range allowing smooth nanograting-free modification narrows down as τ_p increases and eventually tends to zero for $\tau_p > 185$ fs. The thresholds for smooth modification and nanograting formation are found to be independent of the orientation of the laser beam polarization with respect to the writing direction within measurement uncertainty. AFM images also show that there is a trend towards increasing widths and decreasing lengths of the modified regions as τ_p increases for a fixed E_p. This trend is especially pronounced for high $E_p(E_p > 500$ nJ).

The SEM images in Fig. 1(b) demonstrate the transformations in the modification morphology occurring above $E_{\mathrm{th}}(\tau_p)$ for different τ_p. At $E_{\mathrm{th}}(\tau_p) < E_p < 3E_{\mathrm{th}}(\tau_p)$ and $\tau_p > 185$ fs the nanogratings are fully developed in the top portion of the modified regions and merge with the uniform modification in their bottom portions. The etch rate of the interplane material in the top portion shows almost no etching selectivity ($<3\%$) as compared to the uniformly modified fused silica. At $E_p \geq 3E_{\mathrm{th}}(\tau_p)$ and $\tau_p > 185$ fs disruptive modulation of the nanoplanes builds up in the top portion of the modified regions and becomes massive as E_p is increased beyond 5 $E_{\mathrm{th}}(\tau_p)$. The threshold for the disruption formation dramatically increases as τ_p decreases and for $\tau_p=40-50$ fs no such disruption is observed for E_p up to 2500 nJ.

SEM images of the cleaved sample [Fig. 1(c)] reveal that the observed morphology is very similar to the case of the polished and etched sample for given τ_p and E_p. The nanoplanes are straight and uniform for $\tau_p=50$ fs at all used E_p's and for $\tau_p=185$ fs at $E_p < 200$ nJ (e.g., Fig. 1(c), 50 fs, 200 nJ). In this case, the thickness measurement is limited by the SEM resolution to 5 nm. For longer τ_p SEM detects fracturing of a variable thickness of 6–15 nm even at $E_p < 200$ nJ (Fig. 1(c), 500 fs, 100 nJ). At higher E_p's the fracturing be-

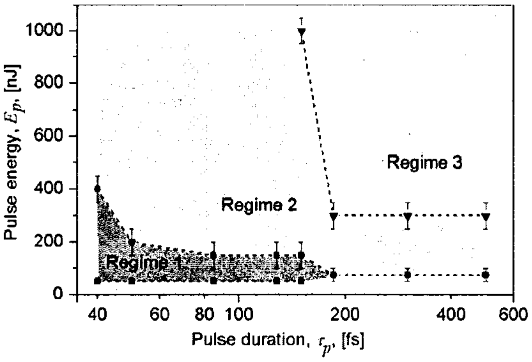

FIG. 2. Threshold pulse energies for different regimes of FLDM in fused silica. E_p's between ■ and ● (regime 1) produce smooth modification. E_p's between ● and ▼ (regime 2) produce nanogratings embedded into smooth modification. E_p's above ▼ (regime 3) produce complex morphology comprising of disrupted regions, nanogratings, and smooth modification.

comes highly disruptive. SEM images of the cleaved sample showing topography indicative of narrow slots and the fact that the etch rate inside the nanoplanes is at least two orders of magnitude higher than that of the uniform modification[10] lead to the conjecture that the nanoplanes are photoinduced nanocracks.

We are developing a nanoplasmonic model based on understanding the formation and orientation of nanoplanes in terms of local field enhancements occurring during inhomogeneous optical breakdown in dielectrics. The plasma density within the nanoplanes can reach supercritical values causing severe highly localized changes in the dielectric structure and even nanocracks. The model uses optical mode coupling in the laser-produced quasimetallic nanoplasma planes to account for the self-replication mechanism.

Threshold E_p's of the observed morphological changes as a function of τ_p are summarized in Fig. 2. Regime 1 corresponding to the formation of nanograting-free smooth modification is most suitable for writing low loss optical waveguides. The graph also emphasizes that smooth modification in a tight focusing geometry is achievable only for a narrow E_p-operating window which increases in size at the shortest τ_p. Regime 2 defines a region to produce self-ordered nanogratings which could allow the direct writing of Bragg filters, taps, and attenuators in fibers or waveguides. This regime is also of practical importance for the production of periodic nanoslots and fs-laser assisted microfluidic channel fabrication. The produced nanogratings allow high etch rates along the modified nanoplanes[10] and the low E_p's ($100\ \mathrm{nJ} < E_p < 300\ \mathrm{nJ}$) result in smooth sidewalls of the selectively etched microchannels. The onset of disruptive modification (regime 3) at modest pulse energies may impose limitations on the applications of FLDM at longer pulse durations (≥ 185 fs).

[1] H. Davis, K. Miura, N. Sugimoto, and K. Hirao, Opt. Lett. **21**, 1729 (1996).

[2] G. Cerullo, R. Osellame, S. Taccheo, M. Marangoni, D. Polli, R. Ramponi, P. Laporta, and S. De Silvestri, Opt. Lett. **27**, 1938 (2002).

[3] A. Marcinkevičius, S. Juodkazis, M. Watanabe, M. Miwa, Sh. Matsuo, and H. Misawa, Opt. Lett. **26**, 277 (2001).

[4] E. N. Glezer, M. Milosavljevic, L. Huang, R. J. Finlay, T.-H. Her, J. P. Callan, and E. Mazur, Opt. Lett. **21**, 2023 (1996).

[5] R. S. Taylor, C. Hnatovsky, E. Simova, D. M. Rayner, V. R. Bhardwaj, and P. B. Corkum, Opt. Lett. **28**, 1043 (2003).

[6] L. Sudrie, M. Franco, B. Prade, and A. Mysyrowicz, Opt. Commun. **191**, 333 (2001).

[7] V. R. Bhardwaj, P. B. Corkum, D. M. Rayner, C. Hnatovsky, E. Simova, and R. S. Taylor, Opt. Lett. **29**, 1312 (2004).

[8] J. D. Mills, P. G. Kazansky, J. J. Baumberg, and E. Bricchi, Appl. Phys. Lett. **81**, 196 (2002).

[9] Y. Shimotsuma, P. G. Kazansky, J. Qiu, and K. Hirao, Phys. Rev. Lett. **91**, 247405 (2003).

[10] C. Hnatovsky, R. S. Taylor, E. Simova, R. V. Bhardwaj, D. M. Rayner, and P. B. Corkum, Opt. Lett. (to be published).

[11] R. S. Taylor, C. Hnatovsky, E. Simova, D. M. Rayner, M. Mehandale, R. V. Bhardwaj, and P. B. Corkum, Opt. Express **11**, 775 (2003).

[12] A. C. Tien, S. Backus, H. Kapteyn, M. Murnane, and G. Mourou, Phys. Rev. Lett. **82**, 3883 (1999).

[13] B. C. Stuart, M. D. Feit, S. Herman, A. M. Rubnechik, B. W. Shore, and M. D. Perry, Phys. Rev. B **53**, 1749 (1996).

[14] M. Lenzner, J. Kruger, S. Sartania, Z. Cheng, Ch. Spielman, G. Mourou, W. Kautek, and F. Krausz, Phys. Rev. Lett. **80**, 4076 (1998).

[15] D. Du, X. Liu, G. Korn, J. Squier, and G. Mourou, Appl. Phys. Lett. **64**, 3071 (1994).

[16] H. Guo, H. Jiang, Y. Fang, Ch. Peng, H. Yang, Y. Li, and Q. Gong, J. Opt. A, Pure Appl. Opt. **6**, 787 (2004).

Polarization-selective etching in femtosecond laser-assisted microfluidic channel fabrication in fused silica

C. Hnatovsky, R. S. Taylor, E. Simova, V. R. Bhardwaj, D. M. Rayner, and P. B. Corkum
National Research Council of Canada, 1200 Montreal Road, Ottawa, Ontario, K1A 0R6, Canada

Received February 9, 2005

We fabricate microchannels in fused silica by femtosecond laser irradiation followed by etching in diluted hydrofluoric acid. We show a dramatic dependence of the etch rate on the laser polarization, spanning 2 orders of magnitude. We establish the existence of an energy-per-pulse threshold at which etching of the laser-modified zones becomes highly polarization selective. The enhanced selective etching is due to long-range, periodic, polarization-dependent nanostructures formed in the laser-modified material. © 2005 Optical Society of America

OCIS codes: 140.3390, 230.4000, 230.3990.

Biochip devices require fabrication techniques allowing integration of photonic and microfluidic components in a single substrate. Planar microfluidic assemblies are made by creating channels in a glass surface by a variety of methods and subsequently sealing them with a cover sheet.[1] Femtosecond (fs) laser-assisted micromachining is a promising alternative technique to produce 3-D devices in transparent dielectrics. It has the advantage that devices can be written directly inside a single block of material. This is due to the highly nonlinear nature of the light–matter interaction, which leads to material modification with high spatial precision determined by the focal volume.

The modified material undergoes preferential chemical etching, allowing the fabrication of microstructures that follow the pattern written by moving the laser focus through the material. This approach has been applied to make microchannels[2] and nanowells[3] directly in fused silica and photostructurable glasses with an additional step involving heat treatment.[4] The potential of the technique to achieve long, high-aspect-ratio channels depends on controlling the etch rate of the modified material.

We demonstrate that the etch rate of fs-laser-fabricated microfluidic channels in fused silica can be controlled by changing the angle between the electric vector of the linearly polarized fs-laser beam and the writing direction. We show that by varying the light polarization we increase the etch rate of the modified material up to 2 orders of magnitude. We also find an energy-per-pulse threshold at which chemical etching of the laser-irradiated zones becomes highly polarization selective. In addition, the etch rate can be controlled by a factor of 40 by varying the energy-per-pulse for certain polarizations of the writing beam. We show that both the polarization-selective etching and the energy threshold are related to the morphology of the irradiated zones.

A schematic of the experimental setup is presented in Fig. 1. Focused pulsed radiation from a regeneratively amplified Ti:sapphire near-infrared laser ($\lambda = 800$ nm, 40 fs pulse duration after the compressor, 100 kHz repetition rate) is used to produce modified zones inside an optical grade fused silica block (Suprasil). The laser beam is spatially filtered and focused with a NA=0.65 lens 100 μm under the surface. The angle θ (Fig. 1) between the electric vector of the linearly polarized output laser beam, **E**, and the writing direction, X, is varied with a zero-order half-wave plate.

To write the structures, the sample is translated perpendicular to the direction of propagation of the laser beam, Z, (transverse writing), as shown in Fig. 1, with a speed of 30 μm/s. Under these conditions the sample moves by only a few tenths of a nanometer between two consecutive laser shots and is exposed to several thousand laser shots per micrometer of travel. The energy-per-pulse, E_p, is varied with a variable attenuator from 50 to 1000 μJ. After irradiation the sample is cut into two pieces. One half is polished from the end face (yz plane) and immersed in a 2.5% aqueous solution of hydrofluoric acid (HF) at 20°C to preferentially etch the modified zones and produce microchannels.[2] The microchannels are characterized under a bright illumination optical microscope after predetermined etching periods. The other half of the sample is cut and polished parallel

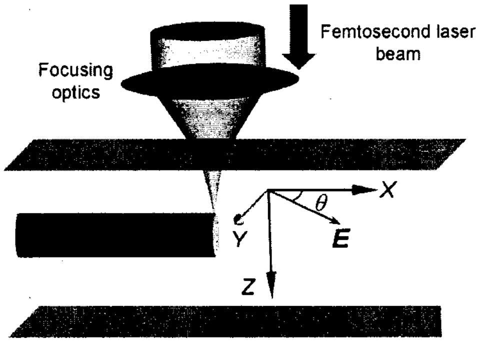

Fig. 1. Schematic of the experimental setup. θ is the angle between the writing direction (x axis) and the electric vector of the fs beam, **E**. The light propagates along the z axis.

0146-9592/05/141867-3/$15.00

to the top surface to intercept the laser-modified zones, etched for 20 min in a 0.5% aqueous solution of HF, and examined under a scanning electron microscope (SEM) to reveal the morphology.

Figure 2 shows optical images after etching of microchannels fabricated in the fused silica block at different E_p and θ. The channels have smooth walls with a sharp transition between modified and nonmodified material. At $E_p = 100$ nJ for all polarizations the modified zones exhibit very weak etching. However, at $E_p = 200$ nJ and above, the structures written at $\theta = 90°$ etch highly selectively, indicating a sharp transition from weak to high selectivity in etching, i.e., an energy threshold for this polarization. No such threshold is observed for $\theta = 0°$ and 45°. For 200 nJ $< E_p <$ 1000 nJ and for all polarizations ($\theta = 0°$, 45°, 90°), the etch rate gradually increases with E_p, with the fastest growth occurring for $\theta = 45°$. A similar sharp increase in the etch rate with E_p of fs-laser-fabricated channels on the surface of fused silica was observed by Bellouard *et al.*,[5] but the polarization state of the laser light in the experiments was not indicated.

The trends observed in the images in Fig. 2 are summarized in Fig. 3, where the etch rates of the modified material, R_m, are plotted as a function of energy-per-pulse, E_p, for three linear polarizations ($\theta = 0°$, 45°, 90°). For the fast etching structures, the etch rate, R_m, is determined as the ratio of the channel length, L, to the etching time. As the channels penetrate deeper into the material, it becomes more difficult for the fresh acid to reach and for the etched material to be removed from the microchannel tips. This causes an apparent decrease in the etch rate. To stay in the regime where L is linearly proportional to the etching time, the value of L chosen for measurements is shorter than 60 μm. For the weakly etching structures R_m is calculated using the relationship $R_m/R_0 = 1 + 1/\tan(\phi/2)$,[6] where the cone angle ϕ is introduced in Fig. 2(b) and the etch rate of nonmodified material, $R_0 = 0.012$ μm/min, is independently determined as the thinning rate of a nonirradiated sample in a 2.5% aqueous solution of HF.

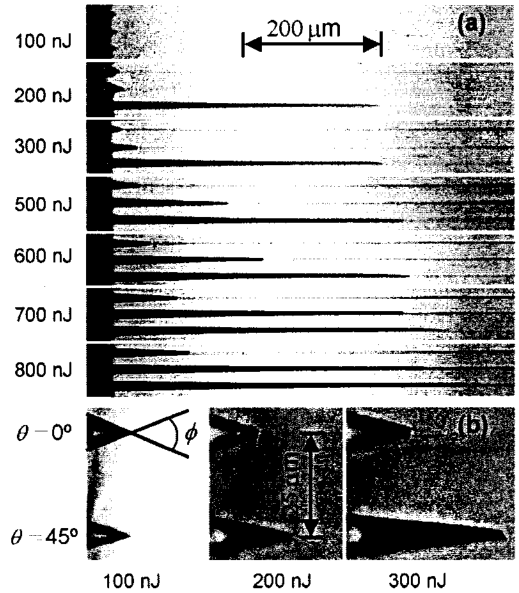

Fig. 2. Optical images of the microchannels in a Suprasil sample after 480 min of etching in a 2.5% aqueous solution of HF acid: (a) In each panel corresponding to a different energy-per-pulse, E_p, the channels from top to bottom are shown for $\theta = 0°$, 45°, 90°. (b) Magnified images of microchannels fabricated at low E_p to determine the etch rate ratio from cone angle ϕ (see text).

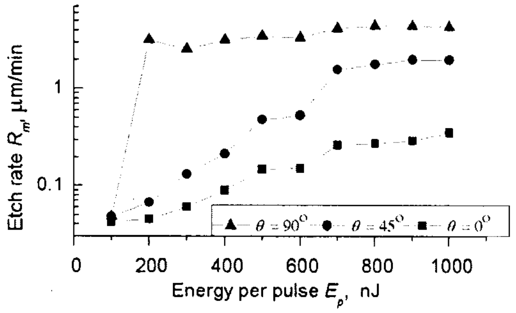

Fig. 3. Etching of the fs-laser-modified zones for different polarizations of the writing beam as a function of energy-per-pulse.

Figure 3 shows that, at $E_p = 200$ nJ, the etching selectivity $R_m/R_0 \approx 3.8$ for $\theta = 0°$, whereas $R_m/R_0 \approx 280$ for $\theta = 90°$. This results in a polarization-etching selectivity of $R_m(\theta = 90°):R_m(\theta = 0°) \approx 70:1$. At $E_p = 1000$ nJ this high ratio drops to 12:1 for $\theta = 0°$ and to a mere 2:1 for $\theta = 45°$. For $\theta = 45°$, R_m changes by a factor of 40 with E_p, i.e., $R_m(E_p = 1000\text{ nJ}):R_m(E_p = 200\text{ nJ}) \approx 40:1$.

The dramatic difference in the polarization-selective etch rates can be explained by analyzing the SEM images of the fs-laser-irradiated and chemically etched structures. At low energy-per-pulse, 50 nJ $< E_p <$ 100 nJ, the laser-induced modification is uniform and polarization independent with $R_m/R_0 \approx 3.5$.[7] At the energy-per-pulse threshold, 100 nJ $< E_p <$ 200 nJ, where the polarization-selective etching starts, SEM images reveal long-range gratinglike nanostructures. Figure 4 shows SEM images of these periodic nanostructures formed along the writing direction for different θ, where the technique reveals that the laser-irradiated zones consist of thin slabs (a few tens of nanometers) of strongly modified material separated by thicker layers ($\approx$250 nm thick) of weakly modified (less than 10% of the modification inside the slabs) fused silica. The gratinglike pattern is always oriented perpendicular to the electric vector of the laser beam and can be controlled by rotating it. The persistence of a constant average period over the entire writing range (many hundreds of micrometers) despite the sample movement suggests a self-replication mechanism underlying the grating formation.[8] Similar polarization-dependent self-organized nanogratings in bulk fused silica have been observed in the static focus of the fs-

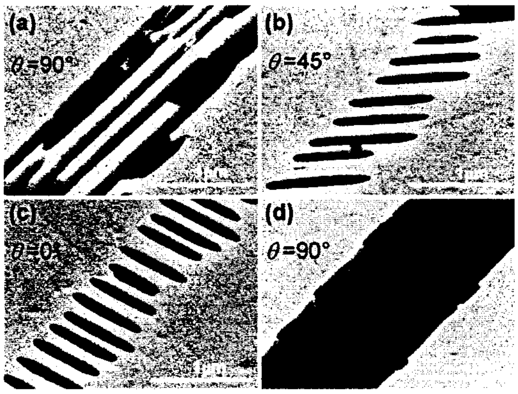

Fig. 4. (a)–(c) Top view (xy-plane) SEM images of long-range periodic nanostructures formed along the writing direction for different θ at $E_p=300$ nJ. (d) $E_p=900$ nJ. The structures were revealed after 20 min of etching in a 0.5% aqueous solution of HF.

laser beam using SEM analysis.[9] The phenomenon was interpreted in Ref. 9 as interference between the incident light field and the electric field of a bulk electron plasma wave. Currently, we are developing a model based on optical mode coupling in laser-produced periodic nanoplasma sheets to account for the long-range self-replication mechanism.

In the grating structures with the planes perpendicular to the writing direction [Fig. 4(c)], the acid encounters alternate layers of modified and unmodified material (that etches slowly), which reduces the cumulative etch rate of a microchannel written with the polarization vector along the writing direction. However, when the grating planes are aligned with the writing direction [Fig. 4(a)], the cumulative etch rate is very high as the etching is confined inside the strongly modified thin slabs, which have a high etch rate. In this case, the acid flow is virtually unobstructed and proceeds along large distances in parallel fashion.

As the energy-per-pulse is increased, the periodic grating planes are gradually destroyed and are eventually substituted with disruptive modification [Fig. 4(d)]. In the high E_p regime, as can be seen in Fig. 3, the polarization sensitivity in etching is significantly reduced.

In conclusion, we have demonstrated polarization-selective etching in fs-laser-fabricated microfluidic channels in fused silica. We have shown that the etch rate of the modified material changes up to 2 orders of magnitude by rotating the writing beam polarization under the specified writing conditions. The polarization sensitivity is caused by the formation of periodic nanoplanes inside the fs-laser-irradiated zones, whose polarization-controlled orientation with respect to the acid flow direction determines the etch rate of the microchannel. The observed energy-per-pulse threshold at which the etch rate becomes polarization selective coincides with the onset of grating-like nanostructures. The all-optical control of the etch rate that is achieved by varying the polarization state of the fs radiation provides a new method for selective chemical etching of dielectric materials and may have a significant effect on the whole domain of laser-assisted micromachining.

C. Hnatovsky's e-mail address is cyril.hnatovsky@nrc.ca.

References

1. M. S. Giridhar, K. Seong, A. Schülzgen, P. Khulbe, N. Peyghambarian, and M. Mansuripur, Appl. Opt. **43**, 4584 (2004).
2. A. Marcinkevičius, S. Juodkazis, M. Watanabe, M. Miwa, S. Matsuo, H. Misawa, and J. Nishii, Opt. Lett. **26**, 277 (2001).
3. R. S. Taylor, C. Hnatovsky, E. Simova, D. M. Rayner, V. R. Bhardwaj, and P. B. Corkum, Opt. Lett. **28**, 1043 (2003).
4. Y. Li, K. Itoh, W. Watanabe, K. Yamada, and D. Kuroda, J. Nishii, and Y. Jiang, Opt. Lett. **26**, 1912 (2001).
5. Y. Bellouard, A. Said, M. Dugan, and Ph. Bado, Opt. Express **12**, 2120 (2004).
6. B. A. F. Puygranier and P. Dawson, Ultramicroscopy **85**, 235 (2000).
7. R. S. Taylor, C. Hnatovsky, E. Simova, D. M. Rayner, M. Mehendale, V. R. Bhardwaj, and P. B. Corkum, Opt. Express **11**, 775 (2003).
8. C. Hnatovsky, R. Taylor, R. Bhardwaj, E. Simova, D. Rayner, and P. Corkum, "Long-range periodic planar nanostructures produced in glass by femtosecond laser dielectric modification," paper to be presented at Conference on Lasers and Electro-Optics 2005, Baltimore, Md., May 22–27, 2005.
9. Y. Shimotsuma, P. Kazansky, J. Qiu, and K. Hirao, Phys. Rev. Lett. **91**, 247405 (2003).

Fabrication of microchannels in glass using focused femtosecond laser radiation and selective chemical etching

C. Hnatovsky, V. R. Bhardwaj
University of Ottawa, Physics Department,
150 Louis Pasteur, Ottawa, Ontario K1N 6N5, Canada

R. S. Taylor
Institute for Microstructural Sciences, National Research Council of Canada,
1200 Montreal Road, Ottawa, Ontario K1A 0R6, Canada

E. Simova, P. P. Rajeev, D. M. Rayner, and P. B. Corkum
Steacie Institute for Molecular Sciences, National Research Council of Canada,
100 Sussex Drive, Ottawa, Ontario K1A 0R6, Canada

Abstract:

We use the combination of femtosecond laser dielectric modification and selective chemical etching to fabricate high-quality microchannels in glass. The photoinduced modification morphology has been studied in fused silica and in borosilicate glass BK7 using ultra-high spatial resolution techniques of selective chemical etching followed by atomic force or scanning electron microscopy. The analysis shows that the high differential etch rate inside the modified regions is determined by the presence of polarization-dependent self-ordered periodic nanocracks or nanoporous structures. We also investigate optimum irradiation conditions to produce high-aspect ratio microchannels with small symmetric cross-sections and smooth walls.

I. INTRODUCTION

Microchannels are the key components of a broad class of micro-total analysis systems (μ-TAS) and biochip devices designed for high-speed and efficient analysis of nano- (and pico-) liter volumes of (bio)-chemical reagents and biological species.[1] Currently, the fabrication of μ-TAS is mainly based on the photolithographic techniques. Although, photolithography is well established, it is an inherently planar technology requiring multiple processing steps (stacking, bonding, sealing, etc.) to integrate photonic and microfluidic components in three dimensions (3-D).[2]

Femtosecond (fs) laser-assisted micromachining is a promising alternative technique to produce 3-D devices in transparent dielectrics. The 3-D capability originates from the non-resonant interaction of femtosecond laser pulses with transparent media. The intensity required for this highly non-linear process is achieved by tightly focusing the laser beam. Short pulses also minimize the heat affected zone and allow modification to be controlled and localized on a sub-micrometer scale. The material surrounding the focal volume remains unaffected by the light passing through it, nominally allowing structures to be written at any depth in 3-D fashion. In some glasses femtosecond laser irradiation produces positive refractive index changes in the modified zones and enables fabrication of optical waveguides embedded in bulk material.[3, 4, 5, 6] Femtosecond laser radiation can also either assist or be directly used to fabricate microchannels allowing their integration with the optical waveguides using one writing laser.

Focused femtosecond laser radiation has been used to fabricate microchannels by drilling surface channels and subsequently sealing them with a coversheet.[7] True 3-D femtosecond laser-assisted microfabrication techniques reported so far are based on: i) drilling bulk quartz[8] and silicate glasses[9] in air, ii) drilling glasses with focused radiation in water[10] and other liquids,[11] iii) irradiation of photosensitive glasses with subsequent stages of baking, chemical etching in hydrofluoric acid (HF)[12] and post-annealing,[13] and iv) irradiation of fused silica followed by chemical etching in HF.[14] Drilling in air requires high pulse energies to ablate the material (> 100 μJ) and is limited to the fabrication of axial microchannels whose straightness and wall roughness may become issues. Only short channels have been demonstrated with drilling in liquids, so far. The technique also requires relatively high pulse energies (> 1 μJ) to disrupt the material causing significant channel wall roughness. Fabrication in specialty photosensitive glasses is a four-step technologically demanding process.

In this paper we concentrate on the last technique for microchannel fabrication by femtosecond irradiation of fused silica with subsequent etching in diluted HF. This simpler true 3-D technique allows writing capabilities and speeds[15] similar to those demonstrated in photosensitive glasses. Moreover, we have recently demonstrated the capability of all-optical control of the etch rate achieved by varying the polarization state of the writing beam.[16] Although previous research has demonstrated the potential of this technique in fabrication of 3-D high aspect ratio microchannels and microchambers, the very mechanism of the preferential chemical etching remains unclear.[15]

We establish the direct effect of the dielectric modification morphology on the etch rate. We show that the selective chemical etching is caused by the formation of polarization-dependent ordered (nanocracks) and disordered nanostructures inside the femtosecond laser modified zones. These observations are supported by measurements showing pronounced fluorescent dye penetration into the modified regions in fused silica. We also identify optimum conditions to produce smooth, long and narrow microchannels in fused silica. In addition, we investigate a borosilicate glass (BK7), in which there is an absence of self-ordered nanostructures, and show that the etching selectivity of modified zones in this material is much weaker than that in fused silica under the same laser irradiation and etching conditions.

The paper is organized as follows: the description of the experimental setup and sample characterization procedures are presented in Sec. II. In Sec III, we demonstrate distinct regimes of the modification morphology in fused silica and their effects on selective chemical etching and the corresponding etch rates. In Sec. IV, we present the results on BK7. The discussion in Sec. V focuses on the physical mechanisms underlying microchannel fabrication using this technique.

II. EXPERIMENT

A. Writing geometries

A schematic of the experimental setup is presented in Fig. 1. A regeneratively amplified mode-locked Ti:Sapphire laser operating at a central wavelength λ_0= 800 nm with a minimum pulse duration of 40 fs after the compressor and a repetition rate, f, of 10-250 kHz is used to produce modified zones inside optical grade glass blocks [synthetic fused quartz (fused silica) from Heraeus (Suprasil® 2 Grade A) or BK7 glass from SCHOTT AG]. Other samples of high grade synthetic fused quartz including wafers (used, e.g., for bioarrays and photomasks) from HOYA and Suprasil® 1 KrF Grade from Heraeus have shown similar performance to Suprasil® 2 Grade A. The linearly polarized Gaussian laser beam is spatially filtered and attenuated by a variable density filter. The orientation of the linear polarization is controlled with a zero-order half-wave plate, whereas the circular polarization is produced with a zero-order quarter-wave plate. The laser beam is tightly focused with one of two microscope objectives with different numerical apertures (NA) [Nikon, Achromat, NA = 0.65 or Nikon, Achromat, Extra Long Working Distance (13 mm), NA = 0.45] under the sample surface. The laser beam overfills the entrance aperture of the focusing optics therefore providing the nominal values of the numerical apertures. Straight regions of modification were made by translating the sample i) perpendicularly to the direction of the laser beam propagation, ***k***, (Fig.1(a), transverse writing geometry) or ii) parallel to ***k*** (Fig.1(b) and (c), axial writing geometry), by using a motorized x-y-z micro-positioning stage. The writing direction, ***S***, defining the direction in which the modification in the sample is produced, is therefore directed opposite the sample's actual motion. The writing speed, v, is varied between 1-1000 μm/s for the transverse geometry and is kept constant at 110 μm/s for the axial geometry. Most of the experiments are performed at f = 100 kHz and v = 30-110 μm/s. Under these conditions the sample moves by less than a nanometer between two consecutive laser shots and is exposed typically to several thousands laser shots per micrometer of travel. The axial writing has two distinct modes when the laser focus is moved i) from the top to the bottom surface (Fig.1(b)) and ii) from the bottom to the top surface of the sample (Fig.1 (c)). The pulse energy, E_p, is varied from 50 nJ to 2.5 μJ delivered to the sample. The pulse duration, τ_p, is varied from 40 to 500 fs by adjusting the grating separation in the pulse compressor with a computer-controlled translation stage. Pulse characterization is performed by intensity autocorrelation. To achieve the nominal τ_p inside the sample, the femtosecond pulse temporal broadening due to group-

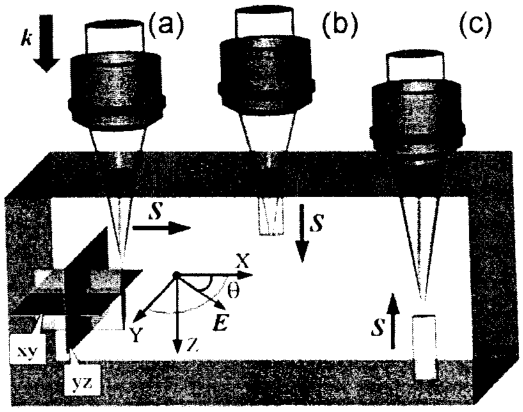

Fig.1 Schematic diagram of the femtosecond laser-induced modification in glass samples. (a) transverse writing geometry. Axial writing geometry is represented by (b) top-to-bottom and (c) bottom-to-top modes. Morphology is studied along xy- and yz-sections.

velocity dispersion in the microscope objectives and polarization components is compensated by pre-chirping the laser pulse in the compressor.

To study the penetration of a dye (filtered solution of rhodamine 6G in isopropanol) through modified regions, the cut and polished samples are pre-etched in 2.5% HF, soaked in the dye solution for 3 hours and then bright-illuminated with an argon-ion laser radiation at 488 nm. The excitation light is cut off using a long-wave pass filter (cut-off wavelength 550 nm) and images of the etched modified regions in the fluorescence light are recorded with a CCD camera.

B. Sample characterization and microchannel fabrication

To characterize the modification morphology, samples are i) cut and polished (or cleaved) perpendicular (yz-plane, Fig. 1) and/or parallel to the top surface (xy-plane, Fig. 1) to intercept the laser-modified zones, ii) etched at room temperature in a weak aqueous solution of hydrofluoric acid (HF), and iii) analyzed using atomic force microscopy (AFM)[17] (Digital Instruments Dimension 3000, contact mode with silicon nitride probes; spatial resolution 15 nm) and scanning electron microscopy (SEM) (Hitachi S-4700, secondary electron imaging; spatial resolution 5 nm). To study fine morphology using both AFM and SEM, the HF concentration used is 0.5% by volume (1 part of 49% HF water solution in 99 parts of water) and the etch time is typically 1-4 min. To reveal the effects of the modification morphology on the etching process, the samples are etched for either longer times in 0.5% HF (15-20 min.) or in 2.5% HF for (3-6 min.) and examined by SEM. To avoid SEM imaging artifacts caused by surface charging the samples are coated with a 1.5-3 nm layer of Pt. The AFM and SEM techniques are complimentary. SEM increases contrast of abrupt deep topographic changes but is almost insensitive to smooth relief on a nanometer scale which is easily mapped by AFM. On the other hand, analysis of AFM images becomes difficult due to loss of contrast when smooth topographic background masks very narrow (< 20 nm) and deep (> 50 nm) features whose actual depth is underestimated in this AFM-probe limited regime.

To fabricate microchannels the samples are wet end-polished to avoid edge/surface effects (see Sec. III C) and immersed into a 2.5% aqueous solution of HF at 20°C to preferentially etch the modified zones. The length of the microchannels is measured under a bright illumination optical microscope after predetermined etching periods and the etch rate is deduced as described in detail in Sec. III B and C.

III. RESULTS: FUSED SILICA

A. Fundamental morphology of modification

Previous studies of femtosecond laser modified regions in fused silica have identified different regimes depending on the laser parameters and focusing conditions, viz. the production of: i) smooth refractive index changes,[3] ii) birefringent zones[18] caused by the laser-induced stress[19] or the formation of self-ordered nanogratings,[20] and iii) micro-voids/microexplosions.[21]

1. Regime of smooth modification

Under tight focusing conditions (NA ≥ 0.45) explored in our experiments, smooth modification is achieved only in a narrow E_p-τ_p operating window which increases in size for very short τ_p's.[22] The regime of smooth modification is observed for any polarization state of the femtosecond laser writing beam for both transverse and axial writing geometries above a polarization-independent pulse energy threshold, typically around 50 nJ. This smooth modification has been associated with uniform positive refractive index changes in the order of 5×10^{-3} and is most suitable for writing low loss optical waveguides[3] and producing nanowells integrated with optical waveguides.[23] However, due to a very weak selectivity in etching[17] this regime is not suitable for fabrication of microchannels.

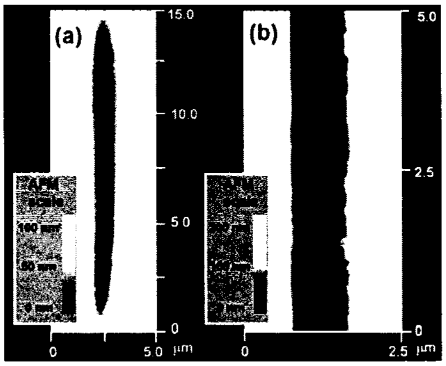

Fig. 2 AFM images of the modified regions produced in the regime of smooth modification in the transverse writing geometry 65 µm subsurface with linear polarization; NA = 0.65, τ_p = 50 fs, f = 100 kHz. (a) yz-section, E_p = 200 nJ, v = 30 µm/s (b) xy-section, E_p = 150 nJ, v = 1 µm/s. The samples were etched for 4 min. in 0.5% HF.

Figure 2 shows the cross-sectional AFM images of femtosecond laser uniformly modified regions written in the transverse geometry in fused silica samples prepared as described in Sec. II B. The roughness inside the modified zones is in the order of a few nanometers.

2. Regime of nanostructure formation

In the regime corresponding to writing with higher pulse energies, E_p, and longer pulse durations, τ_p, self-ordered periodic nanostructures are formed by a linearly polarized femtosecond laser beam. The nanostructures orientated perpendicular to the electric

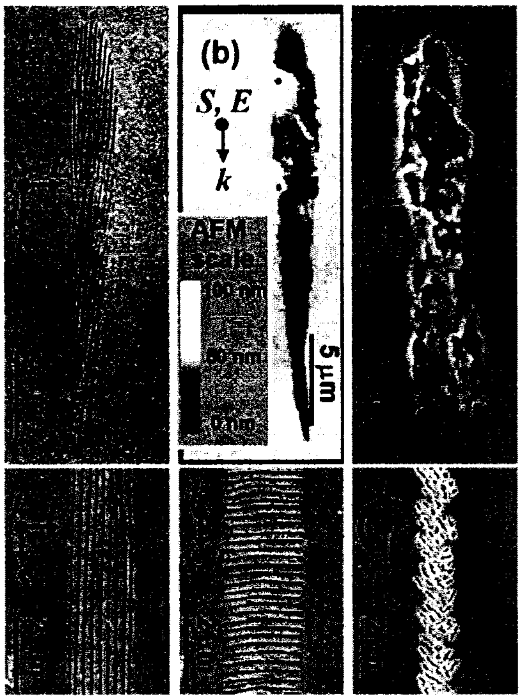

Fig. 3 Polarization-dependent nanostructure formation in the transverse writing geometry. SEM and AFM ((b), top panel) images of modification produced 65 μm subsurface with linear polarization (a) and (b) at τ_p = 125 fs, and (c) circular polarization at τ_p = 300 fs. For (a)-(c) top and bottom panels correspond to yz- and xy-sections, respectively; NA = 0.65, E_p = 300 nJ, f = 100 kHz, v = 30 μm/s. The samples were etched for 3 min. in 0.5% HF.

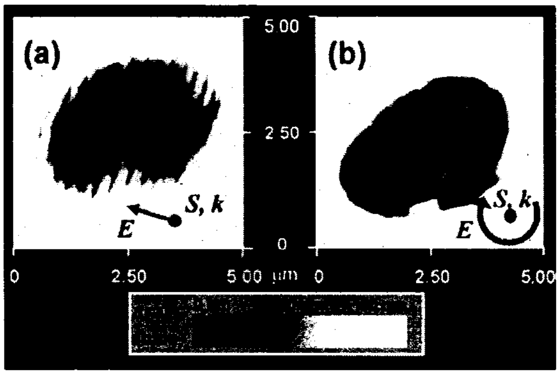

Fig. 4 Polarization-sensitive nanostructure formation in the axial writing geometry. AFM images of the modification xy-sections 100 μm below the top surface (the bottom-to-top writing mode) with (a) linear polarization and (b) circular polarization. For (a) and (b) NA = 0.45, τ_p = 120 fs, E_p = 200 nJ, f = 100 kHz, v = 110 μm/s. The samples were etched for 4 min. in 0.5% HF.

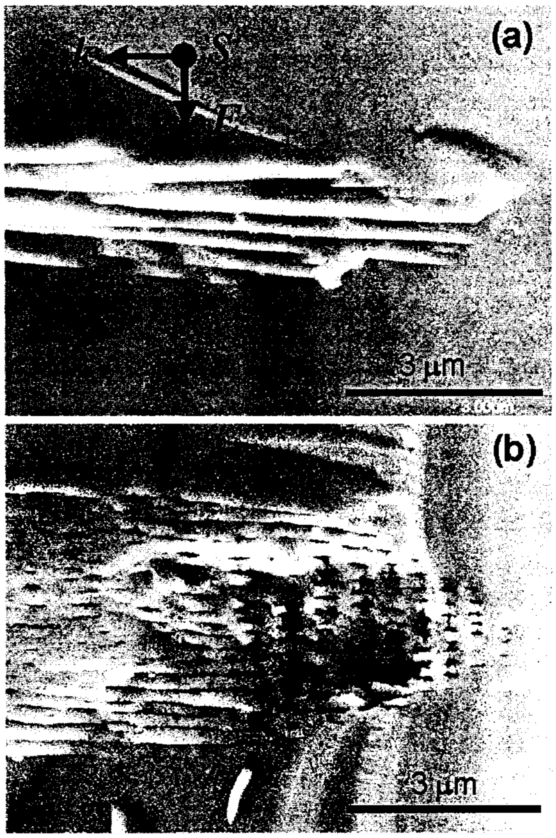

Fig. 5 Evidence of the nanocrack nature of the nanostructures on cleaved unetched samples. SEM images of yz-sections of modification produced in the transverse writing geometry 65 μm subsurface with linear polarization; NA = 0.65, f = 100 kHz, v = 30 μm/s. (a) τ_p = 50 fs, E_p = 200 nJ. (b) τ_p = 500 fs, E_p = 500 nJ. The images show only the top portions of the modified regions. Light propagates from right to left for (a) and (b), i.e. the images are oriented 90 deg. with respect to those shown in Fig. 3.

vector of the laser beam, *E*, were first reported in the static focus of a femtosecond laser beam inside bulk material using back-scattering SEM and Auger electron spectroscopy in one plane at a fixed depth (corresponds to the xy-section in Fig. 1).[20] The phenomenon was interpreted in Ref. 20 as the interference between the incident light field and the electric field of a bulk electron plasma wave. We discuss the appropriateness of this model to our results in Sec. V. Using the technique of selective chemical etching combined with SEM we have shown that, when long range structures are written by continuous motion of the sample under the laser focus, the polarization-dependent nanogratings are formed in 3-D and maintain their periodicity over the entire writing range.[16] The nanograting planes are separated by thicker layers (≈ 250 nm thick) of weakly modified fused silica. The persistence of a constant average period despite the sample motion suggests a self-replication mechanism underlying the nanograting formation. The produced nanogratings show dramatic differences in the etch rate for different orientations of the electric vector with respect to the writing direction.[16] Cross-sectional SEM and AFM images of the nanogratings produced in the transverse writing after weak chemical etching are presented in Fig. 3(a) and (b). In Fig. 3(b) the polished end face of the sample partially intercepts a nanograting plane in the top portion of the modified region, but mainly lies in between the nanograting planes revealing smooth weakly etched modification, best mapped with AFM. Quite different modification morphology is produced with circularly polarized femtosecond radiation within a similar E_p-τ_p parameter space, as seen in Fig. 3(c). Instead of nanogratings typical of linear polarization, circular polarization produces disordered nanostructures varying in size between 30 and 300 nm. The formation of nanogratings for linear polarization and disordered nanostructures for circular polarization is also confirmed for the axial writing within the same regime of writing conditions. The nanostructures for the axial writing are demonstrated in Fig. 4 (a) and (b) for linear and circular polarization, respectively.

Evidence that the nanogratings consist of photo-induced nanocracks is provided in Fig. 5 by SEM images on samples cleaved along the yz-plane. The images reveal morphology indicative of extremely narrow cracks which is nearly identical to the case of polished and etched samples for given pulse duration and energy.[22] The nanocracks are straight and uniform for $\tau_p < 185$ fs with the thickness measurement limited by the SEM resolution to 5 nm (Fig. 5(a)), whereas for longer τ_p SEM detects modulated, highly disruptive fracturing and a variable thickness of 6-15 nm (Fig. 5(b)). The etch rate inside such a nanograting is at least two orders of magnitude higher than that of the smooth modification (Fig. 2).[16] Studies of the fluorescent dye penetration into modified regions produced with both linear and circular polarizations provide further support for the nanocrack/nanovoid nature of femtosecond radiation induced modification in this regime (See Sec. V).

B. Effects of the morphology on selective chemical etching

The etch rate, R_m, of microchannels produced in the transverse writing geometry is strongly affected by the state of polarization of the writing femtosecond laser beam. In the nanograting structures with the planes perpendicular to the writing direction (Fig. 6(a)), the acid encounters alternate thick layers of weakly modified material (that etches slowly) separated by nanocracks, which reduces the cumulative etch rate of a microchannel written with the polarization vector along the writing direction. The etch rate of the inter-plane modification, as measured by the depth of the AFM image, is less than 70% of that of the uniform modification obtained just below the nanostructure threshold (Fig. 2). However, when the nanocracks are aligned with the writing direction (Fig. 6(b)), the cumulative etch rate is very high as the acid flow is virtually unobstructed and proceeds along large distances in parallel fashion. The straightness of the nanocracks depends on how accurately the laser polarization is aligned with respect to the writing directions. Experiments show that a 3-degree deviation from the perfect orthogonality between E and S limits the continuity of the planes to ≈ 10-15 μm, whereas a 1-degree misalignment can result in nanocracks extended over many tens of micrometers along S.

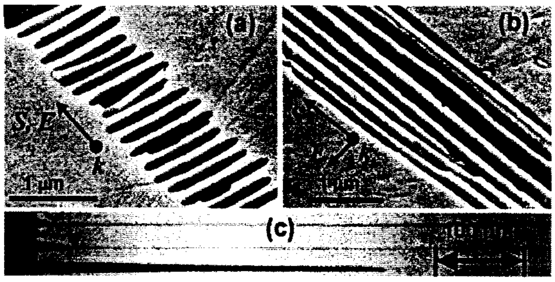

Fig. 6. Polarization-selective etching enabled by the nanograting formation. SEM images of xy-sections of modification produced 65 μm subsurface in the transverse writing geometry with linear polarization (a) parallel and (b) perpendicular to the writing direction, S, NA = 0.65, τ_p = 150 fs, E_p = 300 nJ, f = 100 kHz, v = 30 μm/s. The samples were etched for 20 min. in 0.5% HF. (c) optical images of channels etched for 480 min. in 2.5% HF. The top cone-shaped, very low-aspect-ratio channel corresponds to (a), the bottom channel corresponds to (b), and the channel in the middle corresponds to linear polarization with E at 45° to S.

The dramatic difference in the etch rates of channels with the nanograting aligned perpendicular and along the scan direction is illustrated in Fig. 6(c), where the top cone-shaped etched structure (corresponds to Fig. 6(a)) etches almost two orders of magnitude slower than the microchannel shown at the bottom (corresponds to Fig. 6(b)).

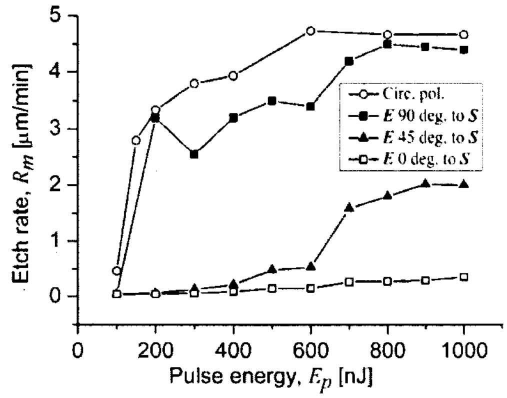

Fig. 7. Polarization-selective etch rates for the transverse writing geometry. Femtosecond laser modified zones produced 65 μm subsurface; NA = 0.65, f = 100 kHz, v = 30 μm/s. τ_p = 150 fs and 130 fs for linear and circular polarization, respectively.

The etch rates of microchannels fabricated with different states of polarization in transverse writing are presented in Fig. 7 as a function of pulse energies, E_p, for circular polarization and linear polarization parallel, perpendicular and at 45° to S. For the fast etching structures, R_m is deduced from the measurements of the channel length, L, versus the etch time, T. As the channels penetrate deeper into the material, it becomes more difficult for the fresh acid to reach and for the etched material to be removed from the micro-channel tips. This causes an apparent decrease in the etch rate as L increases (See Sec. III C). For consistency the value of L chosen to determine the etch rates, R_m, is 50 μm for all microchannels. For the weakly etching structures, the R_m calculations are based on measuring the vertex angle of the cone-shaped structures.[16, 24] Figure 7 demonstrates that the ratio of polarization-selective etch rates, $R_m(E \perp S)$:$R_m(E \parallel S)$ is higher than 70:1. Other orientations of linear polarization provide etch rates lying in between the limiting cases of perpendicular and parallel polarizations. As the energy, E_p, is increased, the nanograting planes become less regular and at $\tau_p > 185$ fs (See below) can eventually be substituted with a disruptive modification. This accelerates the etch rate and partially reduces the polarization sensitivity for microchannels written with linear polarizations, parallel and at 45° to S at high E_p's. As seen from the graph, microchannels written with circular polarization show etch rates similar to those for linear polarization perpendicular to S. The observed high etch rates, R_m, for circular polarization are due to the formation of disordered nanostructures (possibly nanovoids) (see Fig. 3(c)), which can be interconnected allowing fast penetration of the acid along the written modification.

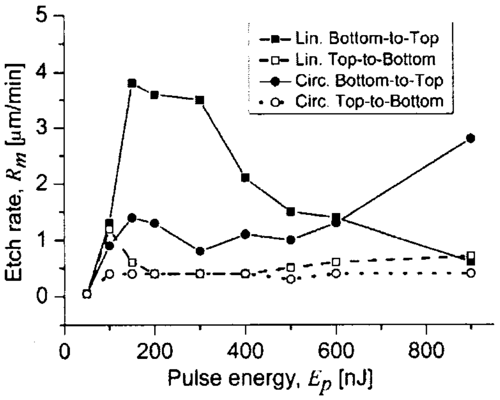

Fig. 8. Polarization-selective etch rates for the axial writing geometry. The etch rates in the femtosecond laser modified zones are measured near the top surface; NA = 0.45, $\tau_p = 120$ fs, $f = 100$ kHz, $v = 110$ μm/s.

For the axial writing geometry the high etching selectivity is also determined by the formation of nanostructures in the modified regions. However, in this case linear polarization does not provide the control of the etch rate, R_m, because of the axial symmetry of the fabrication process. This geometry is also more susceptible to variations in the laser and other writing parameters owing to the combined action of the sample-induced optical aberration[25] and the overwriting effect (See Sec. III C). In the axial writing, the etch rate dependence on pulse energy shows different trends for linear and circular polarizations and also varies with the writing direction, i.e. top-to-bottom vs. bottom-to-top (Fig. 8). For linear polarization, at high pulse energies, E_p, the nanograting becomes less organized and consequentially more obstructive to the acid flow, whereas high energies for circular polarization increase the disordered nanostructure density thus facilitating the acid propagation for this case. This qualitatively explains the shown dependence of R_m on E_p for linear and circular polarizations for the bottom-to-top writing direction. A similar, but a much weaker trend is observed for the transverse writing (See Fig. 11) at short pulse durations ($\tau_p < 130$ fs). For the top-to-bottom writing the overwriting effect and the distortion of the laser focus by the already modified regions upstream of the laser beam can cause strong disordering and interruptions in the produced nanostructures resulting in a systematic decrease in etch rates. For longer pulses ($\tau_p > 150$ fs) the sensitivity of the etch rate on writing direction becomes less pronounced.

The effect of energy, E_p, and pulse duration, τ_p, with the linearly polarized transverse writing beam on the morphology of modification and, as a consequence, on the etching properties of the modified zones is presented in Fig. 9. The case of linear polarization with E oriented perpendicular to S is considered. Generally, the nanogratings are embedded into the smooth modification stretched along the beam propagation direction. The modification caused by the nonlinear absorption is confined to a volume where the femtosecond radiation intensity exceeds the material modification threshold. The modified region will expand both axially and laterally as energy is raised and can stretch over many tens of microns along the beam propagation direction (Fig. 9(a) and (b) at $E_p = 1000$ nJ). The fraction of the modified region which is occupied by the nanograting, however, is strongly affected by the E_p-τ_p writing regime. The nanograting covers the full extent of the smooth modification (i.e., it is embedded into the smooth modification) at short pulse duration ($\tau_p < 130$ fs) for energies ranging from the τ_p-dependent nanograting formation threshold, $E_{th}(\tau_p)$ (100-400 nJ) to more than 1000 nJ.[22] At high pulse energies, however, the average length of nanocracks is reduced in both xy- and yz-planes, their density becomes smaller and the order is weaker than for less energetic pulses (Fig. 9(a)). At longer pulse durations the nanograting formation zone shifts towards the top portion of the smooth modification leaving its tapered tip portion essentially featureless. Operation at high pulse energies in the transitional regime of 130 fs $< \tau_p <$ 185 fs results in progressive disordering of the nanograting and interconnection between some grating planes becomes possible. At energies, $E_p \geq 3\,E_{th}(\tau_p)$ and pulse duration, $\tau_p > 185$ fs, disruptive modulation of the nanogratings builds up in the top portion of the modified regions and becomes massive for $E_p \geq 5\,E_{th}(\tau_p)$ (Fig. 5(b) and Fig 9(b)). The threshold for the disruption formation dramatically increases with decreasing pulse duration and for τ_p =

40-50 fs no such disruption is observed for energies, E_p, up to 2500 nJ.[22]

Morphological changes occurring with the modification produced with circular polarization as energy, E_p, and pulse duration, τ_p, are varied show trends similar to those observed with the writing with linear polarization. Short pulse duration ($\tau_p \sim$ 50-130 fs) for a wide energy range ($E_p \sim$ 100-1500 nJ) produce well-defined, weakly interconnected disordered nanostructures embedded into the smooth modification, whereas longer pulse duration (τ_p > 300 fs) even at moderate energies (E_p > 300 nJ) induce greater disruption consisting of merged micro- and nanostructures. The disordered nanostructures tend to form in the top portion of the modification, even for short pulses (τ_p = 50 fs) and the density of nanostructures increases with E_p. The fraction of the modification occupied by the nanostructures generally decreases as E_p and τ_p are increased, similar to the case of linear polarization.

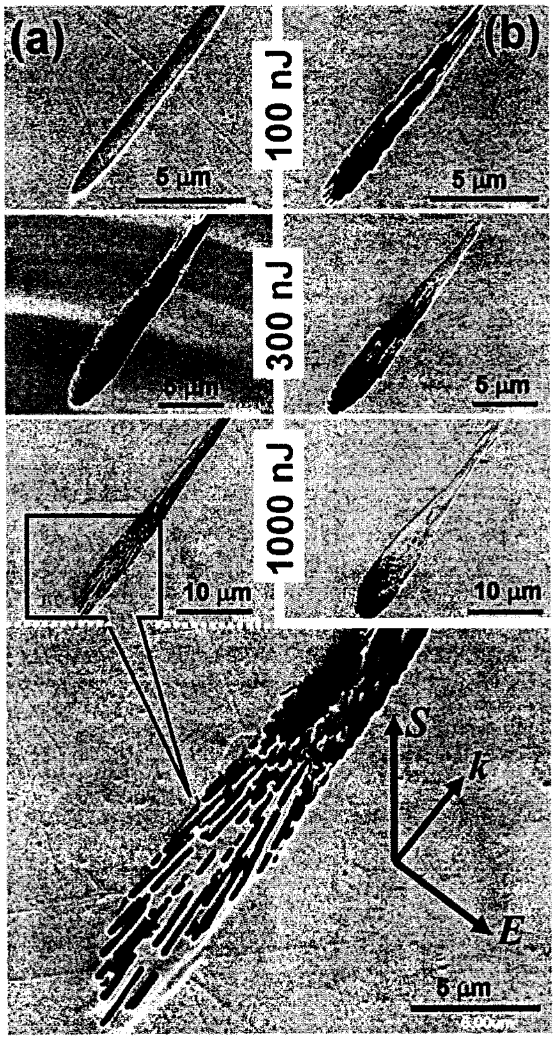

Fig. 9. Dependence of the modification morphology on the pulse duration and pulse energy. SEM images of yz-sections of modification produced in the transverse writing geometry 65 µm subsurface with linear polarization; NA = 0.65, f = 100 kHz, v = 30 µm/s. (a) τ_p = 50 fs. (b) τ_p = 185 fs. The samples were etched for 6 min. in 2.5% HF.

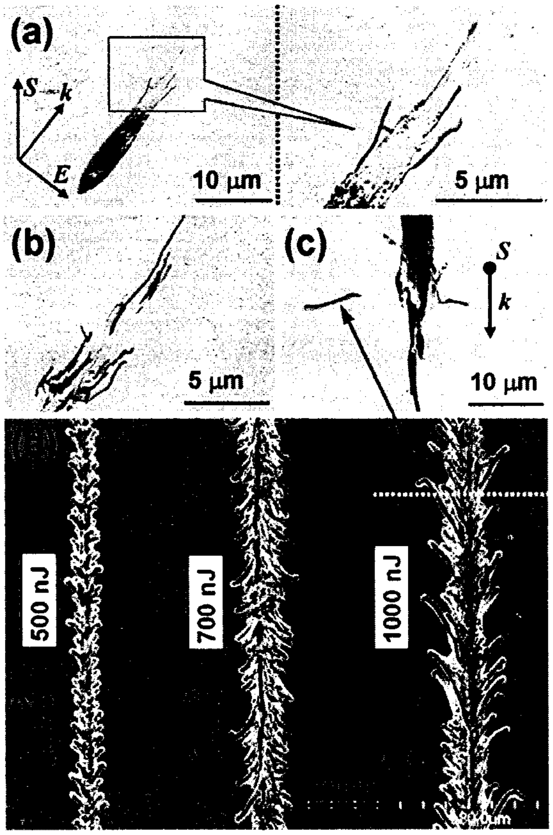

Fig. 10. Irregular cracking at the bottom portions of the modification caused by long pulse durations. SEM images of modification produced in the transverse writing geometry 65 µm subsurface; NA = 0.65, f = 100 kHz, v = 30 µm/s. (a) yz-sections, linear polarization, τ_p = 300 fs, E_p = 500 nJ. (b) yz-sections, linear polarization, τ_p = 500 fs, E_p = 650 nJ. (c) yz-sections, circular polarization, τ_p = 500 fs, E_p = 1000 nJ. (d) xy-section intercepting the cracks, circular polarization at different E_p and S, τ_p = 500 fs. Etch time in 2.5% HF: (a)-(b) 6 min. and (d) 30 min.

At long pulse durations (τ_p > 300 fs) and $E_p \geq 5\, E_{th}(\tau_p)$, irregular cracking (not to be confused with the periodic nanocracks, i.e. nanograting patterns, discussed above) occurs around the tip portions of the modification (Fig. 10). This phenomenon, which was observed both for linear (Fig. 10(a) and (b)) and circular (Fig. 10(c) and (d)) polarizations, affects the wall roughness as well as the minimum achievable cross-sectional area of microchannels and can have serious implications for their microfluidic properties. These cracks become longer and more developed as E_p and τ_p are increased and can be found many microns from the main modification as shown in Fig. 10(c) and (d) at E_p = 1000 nJ, where the cutting plane (white dotted line) happened to intercept one of the longprotruding cracks. A very dramatic observation is shown in Fig. 10(d). The longitudinal xy-sections of modifications reveal that the irregular cracks, for both linear and circular polarizations, branch out from the instantaneous location of the laser focus and tend to propagate in the writing direction *S* towards the region of unmodified material. The nature of this remarkable phenomenon is unclear at the moment.

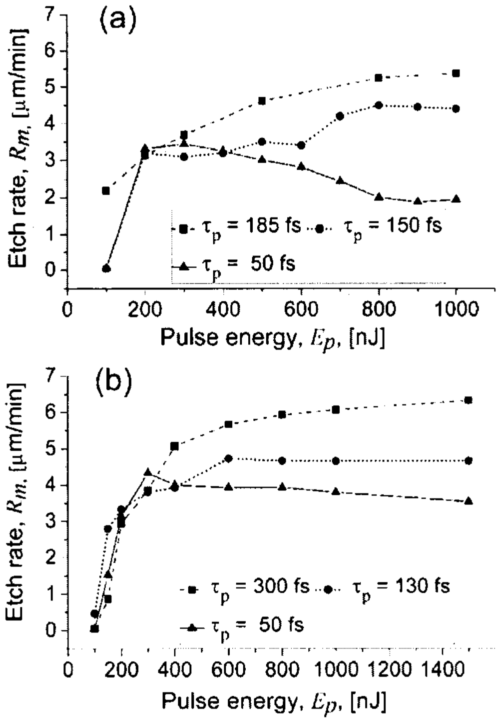

Fig. 11. Etch rate dependence on the pulse energy E_p for different pulse durations τ_p's in the transverse writing geometry. The femtosecond laser modified zones were produced 65 µm subsurface with (a) linear polarization perpendicular to *S* and (b) circular polarization. NA = 0.65, f = 100 kHz, v = 30 µm/s.

The etch rate dependence of modified zones transversely written with circular and linear polarizations on the pulse duration, τ_p, and pulse energy, E_p, is shown in Fig. 11. At energies exceeding 200 nJ and $\tau_p > 130$ fs, the etch rates, R_m, grow with E_p for both polarizations. The reverse trend observed for $\tau_p = 50$ fs (more pronounced for linear polarization) can be qualitatively explained by the SEM images of the modification morphology presented in Fig. 9(a) for $E_p = 1000$ nJ. In this case, as it was mentioned earlier, the density and length of nanocracks is smaller than for lower pulse energies, E_p, and it takes longer for the etchant to penetrate the modified zones and dissolve the slowly etching material in between the nanocracks. Even though initial etch rates (measured at $L = 50$ µm) increase by a factor of three for long pulses and high energies, the magnitude of this effect will be significantly diminished by the etch rate saturation observed with long channels (See Sec. III C).

C. Fabrication of microchannels

The high etching selectivity of femtosecond laser modified zones governed by the formation of nanostructures is the key parameter determining the potential of the technique to fabricate long and high aspect ratio microchannels. To utilize the capabilities of this technique fully, however, other aspects of the fabrication process should be taken into account. Factors affecting the production of microchannels can be subdivided into the following major categories: i) edge effect associated with the transverse writing geometry, ii) femtosecond laser beam scattering effect produced by the material surface ablation in the axial writing (top to bottom), iii) spherical aberration caused by focusing through the air-sample refractive index mismatched interface, iv) overwriting and beam distortion effects accompanying axial writing, and v) saturation in the etch rate of long microchannels. All of the mentioned phenomena are universal and will affect to a greater or lesser extent *any* laser assisted microchannel-fabrication technique in 3-D.

i) The edge of the sample intercepting the converging femtosecond laser beam allows only a portion of the radiation to be focused in the material and produce modification. The rest of the beam remains focused outside the sample in the air at a depth different from that in the material. This discontinuity causes a depletion of the laser power delivered to the focus and gradual disappearance or significant distortion of the modification near the end faces of transversely written modified zones. This effect is especially strong for deep focusing with high-NA optics and requires either removal of significant layers of the material to reach the unaffected modification or submersion of the sample into an index matching fluid.

ii) In the axial writing geometry, when the laser focus crosses the air-sample interface from the top surface (Fig. 1(b)), the initial surface damage caused by ablation creates a scattering zone followed by a volume where the radiation deposited into the sample is attenuated below the nanostructure formation threshold required for the highly selective etching. As the laser focus moves deeper into the sample, the surface damage zone intercepts a smaller fraction of the laser beam at the surface and the deposited energy eventually reaches the threshold for nanostructure formation and high etching selectivity. As a result, for the top-to-bottom writing geometry we observe initial weak selectivity in etching until the unmodified volume is etched away. When the beam is moved from the rear surface upwards (Fig. 1(c)), however, the laser beam is not affected by the surface damage scattering

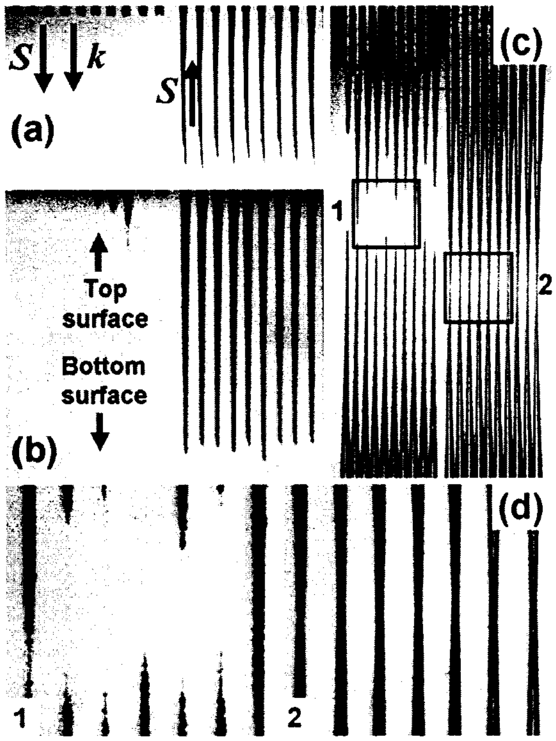

Fig. 12. Optical images showing the effects of the writing direction in the axial writing geometry (a)-(c) on the etching process due to the beam scattering caused by surface ablation and (d) on the microchannel wall roughness due to the overwriting effect. The microchannels were written with linearly polarized femtoseconds radiation; NA = 0.45, $\tau_p = 200$ fs, $E_p = 1000$ nJ, $f = 100$ kHz, $v = 110$ µm/s. (a) 70 min. in 2.5% HF. (b) 300 min. in 2.5% HF. (c) 1450 min. in 2.5% HF. (d) 1450 min. in 2.5% HF; "1" and "2" correspond to the top-to-bottom and bottom-to-top modes, respectively. The separation between the channels is 25 µm. The sample orientation and the beam propagation direction is the same for (a)-(d).

as it continuously propagates through the unmodified material

Fig. 12(a)-(c) show stages in the etching process of microchannels written axially in both the top-to-bottom (left group of channels) and bottom-to-top (right group of channels) modes. Fig. 12(a) demonstrates that initially no selective etching occurs beyond the ablation craters in the top-to-bottom produced modification, whereas the bottom-to-top modification etches highly selectively. Fig. 12(b) shows that in some locations the weakly etching zones following the ablation craters have been etched away and the highly selective etching has started in these locations. In Fig. 12(c) all the top-to-bottom channels etch highly selectively. The channel length variation is caused by the randomness in the breakthrough times. The scattering effect can be overcome by either writing channels in the bottom-to-top mode or by polishing off some 20-25 microns of the material from the top surface. Writing in an index matching fluid may be another possible solution to the problem.

iii) In practice writing channels both transversely and axially is complicated by the presence of the dielectric interface between materials of mismatched refractive indices (e.g., air and the material to be processed) in the optical path of the focused laser beam. The interface introduces an aberration in the wavefront of the converging spherical wave and causes significant spreading of the intensity distribution along the beam propagation direction near the focus. This spreading is also accompanied with a drop in the peak light intensity near the focus,[26, 27] which, under certain conditions, can bring the intensity below the nanostructure formation or even material modification thresholds. The drop in the intensity with the focusing depth occurs much faster in writing with high-NA optics. With a 0.2 NA dry objective it is possible to write at depths of over 10 mm without serious concern for the intensity drop due to spherical aberration, whereas dry writing with a 0.9 NA objective can be restricted to a few tens of microns under the surface unless the laser power is increased dramatically in compensation or the writing is done at fixed depths where the optics are corrected.[28]

So far, we have explored in great detail writing with a 0.65 NA objective which allows one to modify glass at hundreds of microns subsurface without catastrophic deterioration of the laser focus due to the interface-induced spherical aberration. This NA is sufficiently high to minimize self-focusing effects typical of weak focusing geometries.[28, 29] We have also used a 0.45 NA-optic and confirmed the existence of the nanostructure regime of modification enabling fabrication of microchannels at even greater depths without serious effect on the cross-sectional size and shape of the channels. Etch rates of the channels fabricated with 0.45 NA-focusing are similar to those achieved with a 0.65 NA. In experiments with a 0.45 NA objective we found that the threshold for the nanostructure formation increases from $E_p = 75$ nJ near the top surface to ≈ 300 nJ at the bottom surface of a 1.5 mm-thick fused silica block, in a good agreement with our theoretical calculations accounting for spherical aberration.[25] The shapes of the femtosecond laser modified zones in fused silica can also be correlated with the aberrated intensity distribution in the focal volume of the focusing optics.[25, 30] The negative effects of the interface-induced aberration can be alleviated by a microscope objective allowing adjustable compensation for spherical aberration. Using this approach, we have demonstrated diffraction limited writing with a 0.75 NA specialty objective deep (≈ 1 mm) in bulk material at a fixed near-threshold pulse energy, E_p.[25]

iv) When the femtosecond laser focus axially traverses the sample from the top to bottom the converging laser beam is distorted/scattered by the already modified material and the modification downstream of the laser beam is therefore carried out with a modified intensity distribution. This can lead to less modification and possibly poorer quality nanostructures. Furthermore, for axial writing of the sample the highly tapered modified structures (top images in Fig. 3) are drawn through each other. The overwriting process with a tapered beam may cause partial erasure and disruption to the previously written structures. This can lead to alteration in the quality and spacing of the grating planes. When transverse writing is employed the modified nanostructures are mapped onto themselves with little distortion.

Although taking into account all these effects is very difficult, it is plausible to anticipate that the channels written transversely versus axially and top-to-bottom versus bottom-to-top will etch differently. For example, Fig. 12(d) shows that the channels written in the top-to-bottom direction are rougher than their bottom-to-top counterparts, and Fig. 8 shows that etch rates for linear and circular polarizations are dramatically affected by the writing direction.

v) Another phenomenon which strongly affects the fabrication process is saturation of the etch rate of microchannels. Wet chemical etching of fused silica in aqueous HF solution has been the subject of a broad research effort and substantial progress has been achieved in the understanding of the etching mechanism.[31] The dissolution of femtosecond radiation modified fused silica into an aqueous HF solution is a much less studied area, but a heterogeneous chemical reaction requiring several steps to break the chemical bonds in the processed material most likely governs the etching process. The ability of an HF solution to react with the modified material is determined by the acid concentration and will depend on the mass transport properties of the microchannel. As the microchannel length increases, the amount of fresh acid able to reach its end reduces and the etch rate gradually decreases, i.e. saturates. This saturation leads also to the production of microchannels with lower aspect ratios. We observe this trend with microchannels written both axially and transversely using different states of polarization. The reduction in channel etch rate with channel length seems to be a universal phenomenon, not restricted to the described fabrication technique. Similar etch rate saturation has been reported, e.g., in microchannels patterned lithographically.[32]

The magnitude of the saturation effect is exemplified in Fig. 13 presenting the dependence of the channel length, L, on etch time and the dependence of the etch rate, R_m, on L for different pulse energies E_p. The initial E_p-dependent etch rate of microchannels which can be as high as 7-8 μm/min reduces to 1-2 μm/min at $L \approx 200$ μm and further drops to a mere 0.5 μm/min for a millimeter-long microchannel. Increased microchannel lengths also reduce the initial contrast in etch rates, R_m, of the high-energy, fast etching microchannels and their low-energy counterparts (see Fig. 13(b)). To measure L-dependent etch rates of microchannels, R_m-saturation curves are plotted for all of them and etch rates, R_m, are linearly extrapolated at a fixed L (see inset to Fig. 13(b)). The linear fit used for the extrapolation is based on the first 2-3 measurements of R_m made when the channels are shorter than 50 μm. At L = 50 μm, chosen for measurements, the etching process stabilizes and becomes representative of the microchannel.

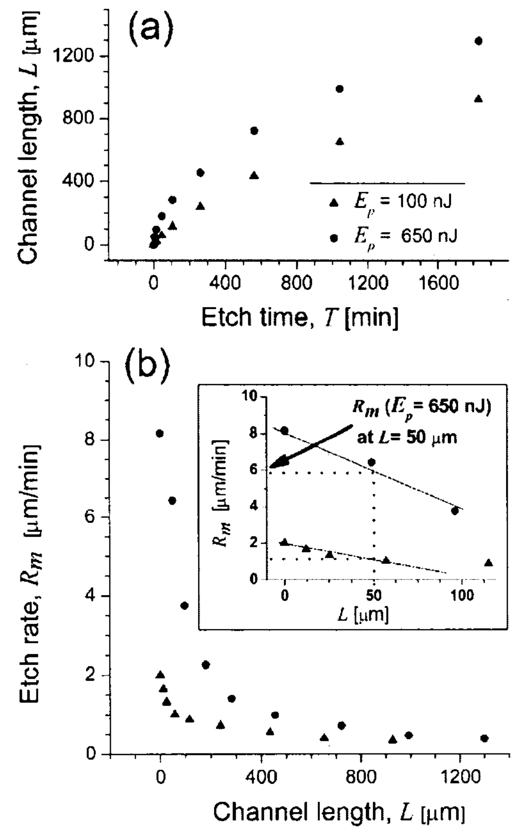

Fig. 13. Etch rate saturation effect observed in microchannels produced in the transverse writing geometry. The channels were written 65 μm subsurface with linear polarization perpendicular to S, NA = 0.65, τ_p = 300 fs, f = 100 kHz, v = 30 μm/s. (a) dependence of channel length on etch time, (b) dependence of channel etch rate on channel length.

IV. RESULTS: BK7

The technique of femtosecond irradiation followed by chemical etching to produce microchannels has been demonstrated so far only for fused silica (quartz glass). In the quest for a cheaper alternative to fused silica, we have applied this fabrication technique to the best-known representative of the borosilicate crown glass family–BK7 (SCHOTT AG nomenclature) optical glass. Chemical stability combined with excellent transmission through visible to near-infrared spectra would make this glass very attractive for various microfluidic applications provided that the high discrimination in etching of the laser-modified versus surrounding material can be achieved.

BK7 is tested within a broad space of laser parameters (50 fs < τ_p < 500 fs, 50 nJ < E_p < 2500 nJ, 10 kHz < f < 250 kHz, focusing (0.45 < NA < 0.9, focusing depth (20-800 μm) and scanning (1 μm/s < v < 1000 μm/s). To correlate the morphology of modification with the femtosecond irradiation conditions the samples are prepared as described in Sec. II B and studied using AFM.

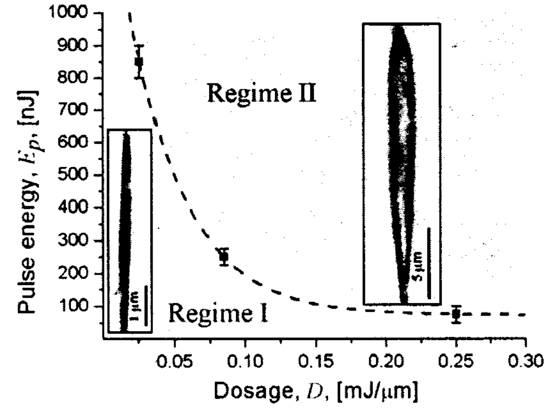

Fig. 14. Regimes of BK7 modification morphology produced in the transverse writing geometry. AFM images represent two distinct types of morphology in the yz-section typical of Regime I (E_p = 50 nJ, v = 300 μm/s) and Regime II (E_p = 200 nJ, v = 3 μm/s). Modification was produced 65 μm subsurface with linear polarization perpendicular to S, NA = 0.65, τ_p = 70 fs, f = 10 kHz. The samples were etched for 2 min. in 0.5% HF.

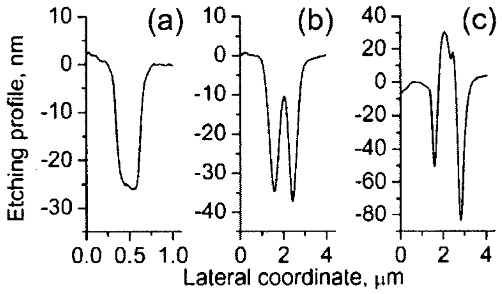

Fig. 15. Etching profiles of the modification in BK7 obtained by AFM. The modification was produced in the transverse writing geometry 65 μm subsurface with linear polarization perpendicular to S, NA = 0.65, τ_p = 70 fs, f = 10 kHz. (a) E_p = 50 nJ, v = 300 μm/s. (b) E_p = 200 nJ, v = 3 μm/s. (c) E_p = 900 nJ, v = 3 μm/s. The etching profiles correspond to (a) Regime I and (b)-(c) Regime II. The samples were etched for 2 min. in 0.5% HF.

AFM reveals two distinct types of morphology i) smooth modification and ii) modification consisting of elevated and depressed filamentary structures. The two regimes allowing the formation of smooth and filamentary modification can be visualized in an energy-dosage diagram, E_p-D-diagram, where the irradiation dosage, D, is defined as $D = E_p f / v$. Within the studied parameter space, the E_p-D-diagram in Fig. 13 (f = 10 kHz) shows a quasi-inverse dependence between E_p and D separating the two regimes. In both Regimes I and II the length of the femtosecond modified zone is determined by the pulse energy, E_p.

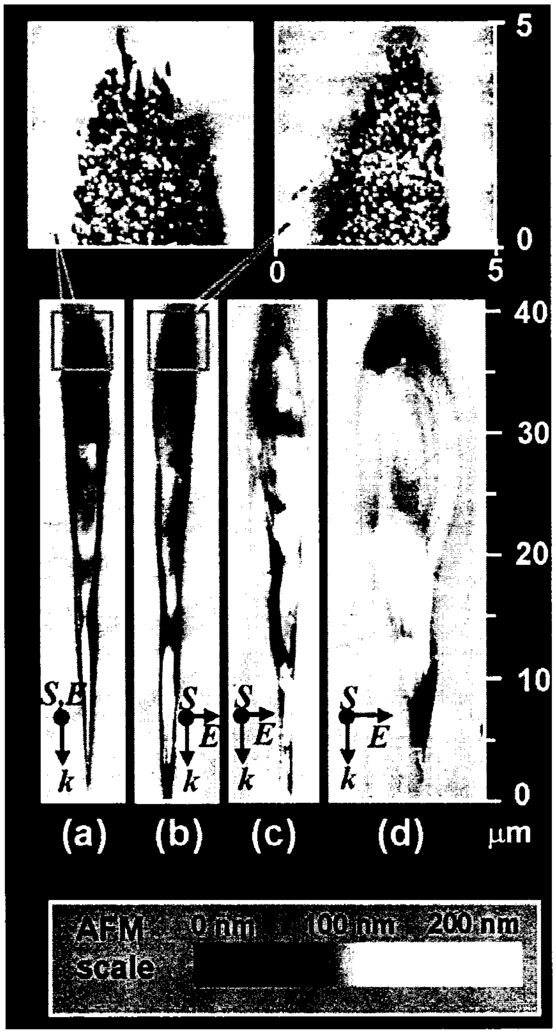

Fig.16 The modification morphology in BK7 corresponding to Regime II. AFM images of the yz-sections of modification produced in BK7 in the transverse writing geometry 65 μm subsurface with linear polarization; NA = 0.65. (a) $\boldsymbol{E}$ parallel to S, τ_p = 70 fs, E_p = 300 nJ, f = 10 kHz, v = 3 μm/s. (b) $\boldsymbol{E}$ perpendicular to S, τ_p = 70 fs, E_p = 300 nJ, f = 10 kHz, v = 3 μm/s. (c) $\boldsymbol{E}$ perpendicular to S, τ_p = 200 fs, E_p = 900 nJ, f = 100 kHz, v = 30 μm/s. (d) $\boldsymbol{E}$ perpendicular to S, τ_p = 500 fs, E_p = 1500 nJ, f = 100 kHz, v = 30 μm/s. The samples were etched for 2 min. in 0.5% HF.

In Regime II the morphology varies depending on the irradiation conditions. An increase in the E_p/v-ratio at constant pulse duration, τ_p, and pulse repetition rate, f, accentuates the filaments. Fig. 15 presents AFM topographic sections across etched smooth and filamentary modifications to follow this trend. The sections were obtained at the bottom portions of the modified regions presented in Fig. 14 and Fig. 16(a). At energy and dosage near the boundary between the regimes, a reversal in the etching selectivity is observed in the middle of the step-like etching profile corresponding to smooth modification. At this stage, however, the filament still etches faster than the surrounding unmodified glass (Fig. 15 (b)). As the E_p-D-point moves further away from the boundary, the etch rate, R_m, in the filament first equals to and then starts lagging behind the etch rate of the unmodified glass (Fig. 15 (c)). In addition, writing at high E_p's and D's produces a granular-like pattern consisting of tiny molten beads, in the top portion of the modification (Fig. 16(a) and (b) with the corresponding zoom-ins on the top portions). By increasing the repetition rate, f, and writing speed, v, at a constant dosage D, the filaments at E_p > 500 nJ are transformed into turbulences (Fig. 16(c)). The granular structures also tend to disappear at high energies. This trend is confirmed for 50 fs < τ_p < 500 fs. At f > 100 kHz, τ_p > 200 fs and E_p > 900 nJ, the lateral expansion of the bulbous top portion of the modification is accompanied with the formation of regions exhibiting high etching selectivity with respect to the unmodified glass (Fig. 16(d)).

The most striking dissimilarity between the femtosecond radiation induced modification in fused silica and BK7 is the absence [Fig. 16(b), (c) and (d)] of nanograting patterns in the latter material under any of the mentioned experimental conditions. Since nanograting planes promote fast polarization-controllable etching in the modified regions the use of BK7 glass in microfluidic applications is severely limited. The etch rates of modified regions in BK7 are essentially independent of the polarization of the laser beam for the same writing parameters and slowly vary from 0.2 to 0.4 μm/min as E_p is increased from 100 to 900 nJ. In the regime of long and high energy pulses (τ_p = 500 fs, E_p = 1500-2500 nJ) conducive to the formation of fast etching regions in the top and bottom portions of the modified zones (Fig. 16(d)), the etch rates R_m, can be as high as 1-2 μm/min, which is close to a typical R_m in fused silica. However, even these high values do not allow one to produce high-aspect-ratio microchannels owing to an order of magnitude higher etch rate of the unmodified BK7 in 2.5% HF (0.11 μm/min) as compared to that of fused silica (0.012 μm/min). The essentially non-uniform distribution of the zones of high etching selectivity over the extensive modified regions results in the production of wide channels with irregular cross-sectional shapes.

V. DISCUSSION

A. Mechanism of nanograting formation

The crucial role of the self-ordered periodic nanocracks in enabling highly differential etching of the modified regions requires analysis of possible mechanisms underlying their formation. Sub-wavelength periodic ripples have been observed over the years on the surface of fused silica as well as other dielectric materials irradiated by lasers operating at different wavelengths and pulse durations. Ripple formation has generally been of short range (microns) and attributed to the interference between the incident laser radiation and scattered or excited surface waves.[33, 34, 35] In most cases the ripple orientation was found to be perpendicular to the incident light polarization. Recently long-range periodic nanostructures with a period of ≈ 220 nm have been produced on the surface of a fused silica sample with tightly focused λ = 800 nm, 100 fs duration laser pulses.[36] The authors claim that the incident light can interact with excited surface plasmons which are not totally restricted to the surface but rather travel inside the material due to the production of a subsurface quasi-metallic plasma.

To explain the formation of nanogratings in bulk material, Shimotsuma *et al.*[20] proposed a model based on the interference between the electric fields of the incident light and an electron plasma wave. This interference imposes a periodic modulation on the electron plasma density causing a corresponding periodic modification in the material. The model predicts a significant dependence of the grating period on the electron plasma density, N_e, and temperature, T_e, i.e., on the laser pulse energy. However, to explain the observed grating spacing, the T_e, required by this model, has to be close to an unrealistically high 10^7 K (corresponds to an electron energy of ≈ 1300 eV) and N_e must approach the critical density $N_c \approx 1.75 \times 10^{21}$ cm^{-3}. Knowing the volume of the modified region from our 3-D measurements we estimate that a minimum E_p of 11 μJ is required to achieve electron temperatures of $\approx 10^7$ K at a plasma density $N_e \approx N_c$. This simple energy balance assumes that all of the laser pulse energy is deposited in the modified zone and in the electron plasma. In contrast, we have found that the threshold for nanostructure formation is typically only 100-200 nJ. The near-critical density N_e assumed by Shimotsuma *et al.* is very restrictive since light will not penetrate the plasma once the critical density is exceeded. On the other hand, if N_e is less than N_c, then T_e must be even higher to reproduce the experimentally observed spacing.

In an independent effort to study the modification morphology at a nanometer scale, we have performed many measurements with a large number of fused silica samples and found that the nanoplane spacing in the laser-modified regions is independent of both the laser polarization and the laser pulse energy, E_p, as reported in our paper.[37] However, in agreement with Shimotsuma *et al.*,[20] we do observe a decrease in the spacing with a high number ($\geq 10^4$) of laser pulses per micrometer of scanning. Specifically, this trend is observed for nanogratings formed near the top of the modified regions. However, the average period of the fully developed nanogratings occupying the central, largest portions of the modification is essentially independent on the number of pulses used for irradiation.

We have developed an alternative model based on nanoplasmonic theory to account for the observed trends in the nanograting formation.[37] According to our model, the nanograting evolution is a three-step process, which takes place over many laser shots, including i) inhomogeneous dielectric breakdown and formation of nanoplasmas, ii) modification of the material on the nanoscale to create a "memory" of previous nanoplasma formation and growth of the modified regions into nanoplanes, and iii) self-organization of the nanoplanes.

Dielectric breakdown can be inhomogeneous for several reasons. The high non-linearity of the process may result in instabilities that lead to an intrinsic inhomogeneity, color centers and defects may act as nucleation centers and hole-enhanced ionization may also play a role.[38] All of the above can lead to the production of localized nanoplasmas in the material. The nanoplasmas are underdense during most of the time of their interaction with the incident laser pulse. The electric field inside an underdense plasma exceeds the laser field, which further enhances the local nature of the breakdown. The boundary conditions require that the electric field around the equator of an underdense spherical nanoplasma with the polar axis aligned along the laser polarization is enhanced as compared with the pole regions where the electric field is suppressed. Thus, underdense nanoplasmas must grow into sheets oriented perpendicular to the laser polarization, as observed experimentally. Even when the plasma density increases, since the nanoplasmas will have a density gradient, their outer boundary remains always underdense, ensuring that they grow into nanoplanes.

The process of nanoplane growth occurs over many laser shots leading to alteration of the material. This implies a memory of the cumulative effect of previous shots that we relate to a lowering of the multiphoton ionization threshold in material that has been previously ionized. In the early stages of material modification these changes might be the result of metastable color centers, bond breaking and the creation of defects. In the later stages the material structure itself can be significantly altered on the nanoscale. The self-organization of the nanoplasmas is postulated to be a result of their semi-metallic properties (i.e., obtained in the later stages of nanoplasma development when the plasma electron density approaches the critical density) which affect the field propagation in a way similar to planar metallic waveguides. Growth of the planes will be favored if they support modes whose field distribution reinforces their own growth or where the field is enhanced by a suitably placed neighbor. The spacing is solely determined by the mode structure and therefore scales linearly with the wavelength independent of the laser pulse energy, as indeed was confirmed in our experiments at $\lambda = 400$ nm[37] (Shimotsuma *et al.* predict a non-linear wavelength dependence[20]). For the lowest order optical mode structure, the nanoplasmonics model predicts a minimum nanograting period of $\lambda/2n$, where n is the index of refraction of the medium. The bulk value of n (i.e., for fused silica $n = 1.453$ at $\lambda = 800$ nm) can be used if plasma formation and material modification predominately occurs at the transient quasi-metallic grating planes. Our model prediction for the minimum nanoplane spacing in fused silica is therefore 275 nm, which is in reasonable agreement with an average value for the experimentally observed spacing of 250 ± 20 nm (measured in the xy-plane using thousands of grating planes).

With a moving focal volume and laser electric field $\boldsymbol{E}$ parallel to the writing direction $\boldsymbol{S}$, the mode structure in the previous spot determines where the nanoplanes would grow in the newly exposed region. In the case when $\boldsymbol{E}$ is perpendicular to $\boldsymbol{S}$, order is imposed on new material via the field distribution at the boundaries of the nanoplanes. Thus self-ordered periodic nanoplanes can be produced when the sample is moved. In the case of circular polarization we expect the nanoplasmas to develop into prolate ellipsoids with their long axis aligned with the beam propagation vector $\boldsymbol{k}$. This is because the field is only continually enhanced at boundary points close to this axis under circular polarization. Our experimental results largely show disordered structures consistent with there being no mechanism to impose long-range order.

We are continuing to develop the theoretical model to more quantitatively describe the dynamics of how nanoplasmas evolve and organize into long-range periodic nanoplanes. We are particularily interested in understanding how short duration ($\tau_p \leq 180$ fs) laser pulses first produce a uniform modified region above the material modification threshold then above a second threshold $E_{th}(\tau_p)$ generate very narrow (5 nm) nanoplanes (Fig. 5) embedded within a uniform modified region such as is shown in Fig. 4(a) and described in Ref. 22.

B. Capabilities of the technique

Pulse duration and pulse energy for any laser polarization play a crucial role in defining the regime of nanostructure formation necessary for the high etching selectivity and the regime of smooth modification to write waveguides which can potentially be integrated with the microchannels produced after etching. The operating windows for both regimes for 0.65 NA focusing have been presented elsewhere.[22] The ability to control the distribution and size of nanostructures over the modified region by changing pulse energy, E_p, and pulse duration, τ_p, is important for microchannel fabrication. To produce channels uniformly etched over their cross-sections, it is desirable that the nanostructures cover the full extent of the modification.

This requirement can be strictly fulfilled within a wide energy range only for linear polarization and $\tau_p <$

130 fs (See Fig. 9). Fig. 17 shows microchannels fabricated under optimum conditions at different E_p's and writing speeds, v. Fig. 17 also demonstrates that the shape and size of microchannels can be controlled by varying E_p, whereas changes in the writing speed, v, have a minor effect on shaping the microchannel cross-sections. Etch rates of the channels are essentially independent of "v" except at the lowest energy, ($E_p \sim$ 150 nJ) close to the nanograting formation threshold in which case the etch rate, R_m, increases with decreasing "v". Inspection of the entrance of the slots with SEM reveals a wall roughness ≤ 50 nm.

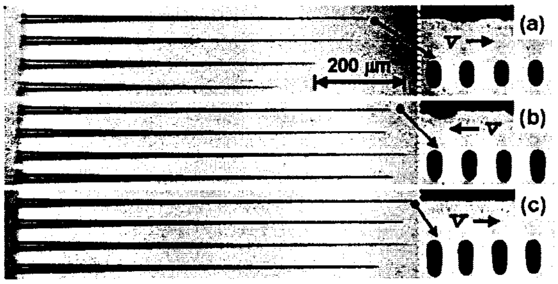

Fig. 17. Cross-sectional and top-view optical images of the microchannels written transversely 65 µm subsurface with linearly polarized fs-radiation; NA = 0.65, τ_p = 120 fs, ,f = 100 kHz. For each E_p = 150, 300 and 400 nJ corresponding to (a), (b) and (c), respectively, 4 different writing speeds v = 3, 10, 20, and 30 µm/s were used. The arrow by the writing speed notation "v" in each panel shows the direction in which "v" is increased. The separation between the channels is 50 µm. The channels were etched for 920 min. in 2.5% HF.

In general, for microchannel formation long pulse duration ($\tau_p > 300$ fs) and high energy ($E_p > 400$ nJ) are not suitable because of increased channel wall roughness associated with uncontrollable cracking under these conditions (See Fig. 10). Even though prolonged etching smoothens the walls near the wide channel entrance, the cracking will seriously affect the channel roughness and shape near its end compromising the use of such channels in microfluidic applications. For long pulses, in order to maximize the coverage of the modified region with the nanogratings, pulse energy should be kept close to $E_{th}(\tau_p)$. This applies for both linear and circular polarization.

Another practical issue affecting the use of a femtosecond laser in microchannel fabrication is the time required to modify and etch fused silica blocks. To fully develop the nanograting 500-3000 laser shots per micrometer of scanning are required. This number is determined by the laser repetition rate f divided by the scan speed, v. We consistently observe the formation of periodic nanocracks in fused silica at 10 kHz < f < 250 kHz and at writing speeds ensuring hundreds of shots per micrometer of scanning. The repetition rates attainable with our setup (f_{max} = 250 kHz) has allowed a writing speed, v = 200 µm/s, to produce fast etching microchannels. Since the periodic nanostructures are still present after annealing at temperatures > 1100°C [39] they may also be present at MHz repetition rates when the characteristic thermal diffusion time becomes comparable to the time between laser pulses.[40] Repetition rates of 1-2 MHz, for which no heat accumulation effects have been observed in fused silica,[41] combined with 500 shots per micrometer of scanning required to produce high-quality nanogratings leads to an impressive potential writing speed in the range of 2-4 mm/s, which is still a conservative estimate.

By combining different regimes of writing and laser polarizations complex channel shapes can be produced in 3-D. As a matter of fact, circular polarization is not very sensitive to the writing direction and allows scanning the sample along any path in 3-D without continuously aligning $\boldsymbol{E}$ and $\boldsymbol{S}$ as required in the case of linear polarization. The maximum length of a microchannel that can be achieved without sacrificing the microchannel aspect ratio (See Sec. III C) is the factor that severely limits the use of the technique so far. Maximum lengths of narrow microchannels attained by us (e.g., Fig. 12) and other authors[14, 15, 42] are limited to 1-2 mm for the etching proceeding from one end. This length budget can easily be exhausted in 3-D integration of microchannels. Longer etch times provides only a small increase in channel length at the expense of significantly poorer aspect ratios. Possible solutions to this problem may include: i) perfect alignment of the nanoplanes along the writing direction when using linear polarization, ii) optimization of the etchant to increase etching selectivity,[43] iii) raster scan the laser beam to create larger zones of modification to compensate for the tapering effect, and iv) operation with laser parameters which produce significant disruption and promote the acid flow over long lengths by microcapillary forces. This can initiate simultaneous dissolution of the modified material along the channel and potentially result in the production of high-aspect-ratio (> 500:1), 2-4 mm-long microchannels.

The feasibility of the latter approach is demonstrated in Fig. 18. The left-hand panel shows images of channels filled with a dye solution (See Sec.II A) in visible light, whereas the right-hand sequence corresponds to the fluorescent images of the same channels. Fig. 18(a) demonstrates that at short pulse duration (τ_p = 50 fs), for which no significant disruptive modification and/or interconnecting nanocracks occurs the dye penetration, is confined within the visible lengths of the microchannels. At longer pulse durations and high pulse energies (Fig. 18(b) and (c)), for both linear and circular polarizations, the dye solution penetrates well beyond the point where the bulk etching has stopped. On the fluorescence images, the ends of the microchannels conveying the dye beyond their actual termination are encircled for clarity. In fact, the dye penetrates up to the very end of the modification lying ≈ 3 mm to the right. SEM images (Fig. 9(b)) of the modification morphology of the channels in Fig. 18(c) show significant disruption in the top portions of the modified regions at E_p > 500 nJ. The partially destroyed nanogratings perforated with numerous interconnected disordered nanostructures (see Fig. 9(b) at E_p = 1000 nJ) can now be penetrated by various liquids including the etchant.

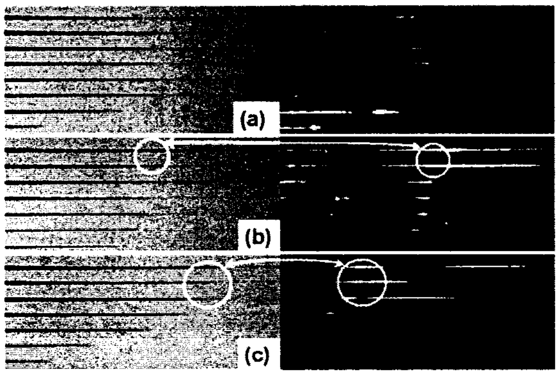

Fig. 18 Fluorescent images demonstrating the dye penetration beyond the etched length of microchannels. Optical images in bright illumination (left) and fluorescent light (right) of the microchannels written transversely 65 μm subsurface with circularly polarized (a)-(b) and linearly polarized (c) fs-radiation; NA = 0.65, τ_p = 50, 300 and 185 fs for (a), (b) and (c), respectively, f = 100 kHz, v = 30 μm/s. For (a) and (b) E_p decreases from top to bottom as 1500, 1000, 800, 600, 400, 300, 200, and 150 nJ; E_p = 150 nJ is not shown for (b). For (c) E_p decreases from top to bottom as 1000, 800, 500, 300, 200, 100, and 75 nJ. The separation between the channels is 50 μm. Etch time in 2.5% HF: 1940 min. for (a)-(b) and 1830 min. for (c).

This observation further confirms that i) the nanostructures play the dominant role in transferring the acid along the modified regions and ii) the etching process in long microchannels is essentially diffusion limited, because otherwise the etching would occur along the full length of the modification. It also suggests that the etch rate saturation problem can be alleviated by frequently interrupting, i.e. cycling the etching process. During each cycle acid will be replenished in the narrow modified regions and the saturation effect decreased.

The ability to produce controlled periodic nanocracks in 3-D has important implications on the field of nanofluidics. The polarization sensitive etching suggests that the acid flows efficiently into very narrow nanocracks whose width at low pulse duration can be as small as few nanometers.[22] Operation near the nanograting formation threshold, for the case of the laser polarization perpendicular to the writing direction *S*, allows the production of a solitary uninterrupted nanocrack extending many tens of micrometers through the modified region along *S*. In the yz-cross-section, the length of a near-threshold nanocrack is only 2-4 μm. We have observed such single nanocracks in the transverse writing geometry when we accurately aligned the laser polarization to be perpendicular to the writing direction (within a degree). By improving the alignment as well as the stability of the femtosecond laser parameters and the translation stage the upper length limit of a solitary nanocrack can be probably pushed even further to hundreds of microns. Such nanocracks can be very attractive for studies of nanoflows and nanocapillary effects.[44]

An extensive study of the morphology and etching properties of fs-radiation induced modification in BK7 borosilicate glass shows that it is impossible to generate nanograting patterns and achieve high etching selectivity in this glass within the explored parameter space. This result provides further evidence of the crucial role of the nanostructures in the selective chemical etching but also restricts the choice of potential materials to those where they can be effectively produced in a controlled fashion. The presence of network modifiers in multicomponent glasses makes it more difficult to understand the mechanisms of fs-induced modification. Our studies of femtosecond induced refractive index changes in various multicomponent glasses, e.g. show that the index changes can be positive (e.g., SiO_2), negative (e.g., BK7), or nonuniform depending on the glass composition, which requires an individual explanation in each particular case.[6] So far, the nanograting patterns in the bulk material have been observed in a scant assortment of materials, viz. SiO_2 glass and TeO_2 crystal.[45] In a multicomponent glass BK7, phase separation effects (See Fig. 16) and migration of network modifiers due to local melting, which may occur on a shot-to-shot basis, can continuously erase the memory about previous laser exposures thus impeding the formation of ordered nanostructures. Any heat accumulation of energy in the modified volume at high pulse repetition rates makes it even more difficult to achieve nanogratings. The formation of the molten beads (Fig. 16 (a) and (b)) and filaments (Fig 14 –16) and the transformation of the modified region to a bulbous structure at high repetition rates support this thermal-based explanation. Further experimental and theoretical work has to be done to elucidate conditions promoting or preventing the nanograting formation in other glasses.

VI. CONCLUSION

In summary, we have used ultra-high spatial resolution diagnostics to show that the dielectric modification morphology in fused silica determines the etch rate of microchannels fabricated using focused femtosecond laser radiation and selective chemical etching. The highly differential etching of the modified regions is correlated with the formation and orientation of self-ordered nanocracks in 3-D (linear polarization) and disordered nanostructures (circular polarization) which allow the etchant to penetrate into the glass and etch microchannels. In BK7 glass, where the femtosecond laser irradiation cannot produce such nanostructures, the differential etching between laser-modified and surrounding material is insufficient to fabricate long high-aspect-ratio microchannels. Only certain types of modification morphology, which are determined by the femtosecond laser and writing parameters, ensure the production of microchannels with regular cross-sectional shapes and smooth walls. The demonstrated control over the etching (and optical) properties of the photo-modified regions is important for 3-D monolithic integration of the microchannels with microphotonic components to fabricate various biochip devices.

References

1. A. Manz, H. Becker (eds.): *Microsystem Technology in Chemistry and Life Sciences* (Springer, New York 1998).
2. G. T. A. Kovac, *Micromachined Transducers Source Book*, (Mc Graw Hill, New York, 1998).
3. K. M. Davis, K. Miura, N. Sugimoto, and K. Hirao, Opt. Lett. **21**, 1729 (1996).
4. K. Miura, J. Qiu, H. Inouye, and T. Mitsuyu; K. Hirao, Appl. Phys. Lett. **71**, 3329 (1997).
5. D. Homoelle, S. Wielandy, and A. L. Gaeta; N. F. Borelli and C. Smith, Opt. Lett. **24**, 1311 (1999).
6. V. R. Bhardwaj, E. Simova, P. B. Corkum, and D. M. Rayner, C. Hnatovsky, R. S. Taylor, B. Schreder, M. Kluge, and J. Zimmer, J. Appl. Phys. **97**, 83102-1-9 (2005).
7. M. S. Giridhar, K. Seong, A. Schülzgen, P. Khulbe, N. Peyghambarian, and M. Mansuripur, Appl. Opt. **43**, 4584 (2004).
8. H. Varel, D. Ashkenasi, A. Rosenfeld, M. Wähmer, E. E. B. Campbell, Appl. Phys. A **65**, 367 (1997).
9. L. Shah, J. Tawny, M. Richardson, and K. Richardson, Appl. Surf. Sci. **183**, 151 (2001).
10. Y. Li; K. Itoh, W. Watanabe, K. Yamada, and D. Kuroda; J. Nishii; Y. Jiang, Opt. Lett. **26**, 1912 (2001).
11. D. J. Hwang, T. Y. Choi and C. P. Grigoropoulos, Appl. Phys. A **79**, 605 (2004).
12. Y. Kondo, J. Qiu, T. Mitsuyu, K. Hirao, and T. Yoko, Jpn. J. Appl. Phys. **38**, L1146 (1999).
13. K. Sugioka, Y. Cheng and K. Midorikawa, Appl. Phys. A **81**, 1 (2005).
14. Marcinkevičius and S. Juodkazis; M. Watanabe, M. Miwa, Sh. Matsuo, and H. Misawa; J. Nishii, Opt. Lett. **26**, 277-279 (2001).
15. Y. Bellouard, A. Said, M. Dugan, and Ph. Bado, Opt. Express **12**, 2120 (2004).
16. C. Hnatovsky, R. S. Taylor, E. Simova, V. R. Bhardwaj, D. M. Rayner, and P. B. Corkum, Opt. Lett. **30**, 1867 (2005).
17. R. S. Taylor, C. Hnatovsky, E. Simova, D. M. Rayner, M. Mehendale, V. R. Bhardwaj, and P. B. Corkum, Opt. Express **11**, 775 (2003).
18. L. Sudrie, M. Franco, B. Prade and A. Mysyrowicz, Opt. Commun. **191**, 333 (2001).
19. V. R. Bhardwaj, P. B. Corkum, D. M. Rayner, C. Hnatovsky, E. Simova and R. S. Taylor, Opt. Lett. **29**, 1312 (2004).
20. Y. Shimotsuma, P. G. Kazansky, J. Qiu and K. Hirao, Phys. Rev. Lett. **91**, 247405 (2003).
21. E. N. Glezer, M. Milosavljevic, L. Huang, R. J. Finlay, T.-H. Her, J. P. Callan, E. Mazur, Opt. Lett. **21**, 2023 (1996).
22. C. Hnatovsky and R. S. Taylor; P. P. Rajeev, E. Simova, V. R. Bhardwaj, D. M. Rayner, and P. B. Corkum, Appl. Phys. Lett. **87**, 014104-1-3 (2005).
23. R. S. Taylor, C. Hnatovsky, E. Simova, D. M. Rayner, V. R. Bhardwaj, and P. B. Corkum, Opt. Lett. **28**, 1043 (2003).
24. B. A. F. Puygranier and P. Dawson, Ultramicroscopy **85**, 235 (2000).
25. C. Hnatovsky, R. S. Taylor, E. Simova, V. R. Bhardwaj, D. M. Rayner, and P. B. Corkum, J. Appl. Phys. **98**, 13517-1-5 (2005).
26. P. Török, P. Varga, Z. Laczik, and G. R. Booker, J. Opt. Soc. Am. A **12**, 325 (1995).
27. S.H. Wiersma, P. Török, T.D. Visser, and P. Varga, J. Opt. Soc. Am. A **14**, 1482 (1997).
28. C. B. Shaffer, A. Brodeur and E. Mazur, Meas. Sci. Technol. **12**, 1784 (2001).
29. D. M. Rayner, A. Naumov, and P. Corkum, Opt. Express **13**, 3208 (2005).
30. A. Marcinkevičius, V. Mizeikis, S. Juodkazis, S. Matsuo, H. Mizawa, Appl. Phys. A **76**, 257 (2003).
31. G. A. C. M. Spierings, J. Mater. Sci. **28**, 6261 (1993).
32. M. B. Stern, M. W. Geis, and J. E. Curtin, J. Vac. Sci. Technol. B, **15**, 2887 (1997).
33. Z. Guosheng, P. M. Fauchet, A. E. Siegman. Phys. Rev. B, **26**, 5366 (1982).
34. J. E. Sipe, J. F. Young, J. S. Preston, H. M. van Driel, Phys. Rev. B, **27**, 1141 (1983).
35. A. Barborica, I. N. Mihailescu, V. S. Teodorescu, Phys. Rev. B, **49**, 8385 (1994).
36. R. Wagner, J. Gottmann, A. Horn, and E. W. Kreutz, Proc. SPIE **5662**, 168 (2004).
37. R. P. Pattathil, C. Hnatovsky, E. Simova, R. B. Vedula, R. S. Taylor, D. M. Rayner, P. B. Corkum, Photonics North 2005, 12–14 Sept. 2005, Toronto, Canada, Proc. SPIE **5971**, 53.
38. L. N. Gaier, M. Lein, M. I. Stockman, P. L. Knight, P. B. Corkum, M. Yu. Ivanov, and G. L. Yudin, J. Phys. B: At. Mol. Phys. **37**. L57 (2004).
39. E. Bricchi, W. Yang, and P. Kazansky, *'Robustness of Femtosecond Direct Written Structures in Silica Glass,'* presented at the Conference on Lasers and Electro-Optics, Baltimore, MA, (USA), May 22-27, 2005.
40. C. B. Schaffer, J. F. García, and E. Mazur, Appl. Phys. A **76**, 351 (2003).
41. S. M. Eaton, H. Zhang, and P. Herman; F. Yoshino, L. Shah, J. Bovatsek, A. Y. Arai, Opt. Express **13**, 4708 (2005).
42. J. Amako, D. Sawaki, and E. Fujii, J. Opt. Soc. Am. B, **20**, 2562 (2003).
43. J. L. Vossen, W. Kern (eds.): *Thin Film Processes* (Academic Press, Inc., Orlando 1978), Part V Etching Processes, pp. 401.
44. J. Han and H. G. Craighead, Science **288**, 1026 (2000).
45. Y. Shimotsuma and K. Hirao; J. Qiu; P. G. Kazansky, Mod. Phys. Lett. B **19**, 225 (2005).

Conclusion

The results presented in this thesis can be subdivided into two major categories: i) ultra-high spatial resolution studies of the modification produced in fused silica and other glasses at different fs laser pulse parameters and focusing conditions and ii) and the fabrication of microchannels using the technique of selective chemical etching of the fs radiation-induced modification in fused silica. We start the discussion by establishing the link between the glass composition, fs laser parameters and focusing conditions on one side and the optical properties and morphology of the modification on the other. Then we show how the morphology affects the fabrication of microchannels. We conclude this thesis with outlining new potential applications of the fs laser dielectric modification technique.

Effects of glass composition on induced refractive index change

In ARTICLE II we have performed an extensive study on fs laser-induced refractive index changes in a wide variety of multicomponent glasses from SCHOTT AG in order to assess their suitability for photonic applications. The microreflection technique described in ARTICLE I and the refractive near-field (RNF) technique were used to obtain high resolution refractive index profiles of the fabricated waveguide structures. The intercomparison of these two techniques performed on selected glasses confirmed that they yield similar results. As it was mentioned in **Section 2**, the microreflection technique provides the best compromise between resolution and accuracy which can be achieved and the easiness of implementation. The data showed that except for some aluminum–silicate glasses all other investigated glasses exhibited a negative refractive index change upon laser irradiation. The modification in different glasses can result in uniform positive (e.g., SiO_2), uniform negative (e.g., BK7) or nonuniform refractive index changes (alkali–aluminum–silicate glasses) under the same writing conditions. Moreover, a single glass under different irradiation conditions can exhibit negative or positive index changes. The shape of the index profile also strongly varies with changing the writing parameters. The observed pronounced variability between glasses makes refractive index profiling imperative for each glass composition under a wide range of writing conditions. It also appears that fused silica glass is a preferable material for the fs laser fabrication of waveguides as it provides the highest and most uniform photo-induced refractive index change among other studied glasses.

Influence of irradiation conditions on modification in fused silica glass

Spherical aberration induced by the air-sample interface. In ARTICLE III we address the effects of an optical aberration on the shapes and positions of the fs laser-modified zones in fused silica glass. Spherical aberration introduced by the dielectric interface between materials of mismatched refractive indices (e.g., air and the material to be processed) causes significant spreading of the intensity distribution along the beam propagation direction near the focus of a fs laser beam. This spreading is also accompanied with a drop in the peak light intensity near the focus and can easily bring the intensity below the nanostructure formation or even material modification thresholds.

The threshold pulse energy values for the different regimes of modification (Regimes I-III) described in the thesis and ARTICLES IV and VI were obtained with a NA = 0.65 objective ~60 micrometers below the sample surface where the estimated drop in the intensity is below 10% of the original unaberrated value. The operation at higher NA's and larger focusing depths requires compensation of spherical aberration to avoid inaccuracy in determining the threshold values. We also note that investigation of the self-focusing effects in the tight focusing geometry on the shape and size of the modified regions should be carried out only in the absence of spherical aberration because otherwise it will mask the possible contribution of the nonlinear response of the medium. In ARTICLE III we have demonstrated, using the etching-AFM technique, that the shapes and separations of fs-laser modified zones in fused silica are correlated with the aberrated intensity distribution in the focal volume of the focusing optics. This allows one to assess how spherical aberration limits the depth performance obtainable with any NA objective and to choose between using a high NA objective to write small features over a limited depth and a lower NA objective to produce larger features but over a greater depth. In ARTICLE III we also show that spatial characteristics of the laser-modified zones can be controlled by special objectives designed to provide correction for a variable amount of spherical aberration. This is important for 3-D fs-assisted fabrication of optical waveguides, optical data storage and microfluidic devices at depths varying on a millimeter scale. Dry objectives become the preferred tool to perform these tasks since at such depths the use of high NA immersion optics is inconvenient due to the necessity of manipulating submerged samples and the limited correction range of the commercially available designs.

Laser polarization, pulse duration and pulse energy. In ARTICLES IV and VI we have shown that the morphology of fs laser modified regions in fused silica is determined by the combination of these three laser parameters. The pulse energy threshold values were obtained for a NA = 0.65 objective.

1) At short pulse durations (< 150 fs) with the laser pulse energy above the material modification threshold, the etching-AFM/SEM diagnostics techniques reveal well-defined uniformly etched regions of smooth modification. This smooth modification (Regime I) has been associated with positive refractive index changes on the order of 5×10^{-3} and is most suitable for writing low loss optical waveguides. Heating the sample to 900°C can erase this type of modification. The microreflection technique combined with NSOM used in the collection mode allow one to characterize the magnitude and the profile of the induced index changes and assess the actual performance of the fs laser-written waveguides. It also appears, that the smooth modification is achievable only for a narrow pulse energy-pulse duration operating window which increases in size for very short pulses (~ 50 fs). The regime of smooth modification is observed at approximately the same pulse energy for any polarization state of the fs laser writing beam for both transverse and axial writing geometries.

2) Above a certain pulse energy threshold value which strongly depends on the pulse duration nanostructures are formed within the modified region (Regime II). Linearly polarized radiation produces nanogratings with an average period of ~ 250 nm orientated perpendicular to the electric vector of the laser beam, whereas circular polarization tends to form disordered nanostructures (nanovoids) varying in size between 30 and 300 nm. Using the etching-AFM/SEM techniques we show that the polarization-dependent nanogratings are formed in 3-D and maintain their periodicity over the entire writing range when the modification is produced by continuous motion of the sample under the laser focus of a linearly polarized fs laser beam. The nanograting structures, at least for long pulses, consist of ordered nanocracks with the width on the order of 10 nm separated by thicker layers of weakly modified fused silica. The formation of nanogratings or disordered nanostructures is

imperative for the fs laser-assisted microfluidic channel fabrication to provide the required high etching selectivity of the modified regions. The self-ordered nanogratings produced in Regime 2 may also allow the direct writing of Bragg-filters (in Ref. [98] we show that the nanograting period can be controlled by adjusting the wavelength of the fs laser radiation), taps and attenuators in fibers or waveguides.

The formation of the nanograting structures in the volume has been reported so far only for fused silica glass and tellurium dioxide crystal (TeO_2) [99]. Our studies of fs laser-modified zones in BK7 borosilicate glass reveal i) a different morphology consisting of smooth modification or filaments and turbulences depending on the irradiation conditions and ii) an absence of self-ordered nanostructures. This result emphasizes the crucial role of the material composition in the grating formation mechanism. Further experimental data obtained on other dielectrics is sorely needed to clarify in which way the physical and chemical properties of the material determine its propensity to form nanostructures during fs irradiation. It is also worth reiterating that only ultra-high spatial resolution techniques can allow one to unambiguously detect and study these nanometer-size structures.

3) At high pulse energies the extent of individual nanograting planes is reduced, their density becomes smaller and the order is weaker than for less energetic pulses. The effect of high energies for circular polarization is mainly associated with an increase in the disordered nanostructure density. For relatively long pulses (≥ 200 fs) the etching-AFM/SEM techniques also detect the onset of disruptive modification in the top portion of the modified regions (Regime III). At even higher pulse energies the disruptive modification becomes very significant. In the case of linear polarization the nanogratings are perforated with distinct nano- and microvoids, whereas in the modified regions produced with circular polarization the disordered nanostructures grow in numbers and merge to eventually form nanoporous modification. The threshold for the disruption formation dramatically increases as the pulse duration decreases and for 40 fs pulses no such disruption is observed for the pulse energies up to 2500 nJ.

Femtosecond laser-assisted fabrication of microchannels in glass

In ARTICLES V and VI we demonstrate that polarization-dependent nanostructures (i.e., nanogratings or nanovoids) formed inside the fs laser-modified zones determine their high etching selectivity and that the all-optical control of the etch rate becomes possible by varying the polarization state of the fs radiation. These findings significantly enhance the existing capabilities and indicate new potential applications of the technique. The low threshold required for the nanostructure formation (~ 100 nJ) makes the channel fabrication possible at high pulse repetition rates (hundreds of kHz) and high writing speeds (~ 1-5 mm/s). The inherent insensitivity of circular polarization to the writing direction allows one to modify the material in 3-D along any path. The cross-sectional area of a microchannel can be controlled by using the focusing optics with different NA or adjusting the laser power. Operation near the nanograting formation threshold allows the production of a solitary uninterrupted nanocrack extending many tens of micrometers through the modified region along the writing direction (the laser polarization is assumed to be perpendicular to the writing direction). We believe that the upper length limit of a solitary nanocrack can be as high as hundreds of microns. Such nanocracks can be very important for studies of nanoflows and nanocapillary effects. In the case of circular polarization, high pulse energies ($\geq$ 500 nJ) and relatively long pulse durations ($\geq$ 200 fs) the nanovoids covering the modified regions merge and produce a sponge-like nanoporous structure which becomes permeable for liquids *without any chemical etching*. The cross-sectional area of such a nanoporous region is typically 5 x 5 μm^2, but it can be controlled by adjusting the laser parameters. We have observed penetration of a fluorescent dye into such capillaries over millimeters. The penetration rate depends on the pulse energy and is slower for less energetic pulses. This discovery has very important implications for the whole field of microfluidics. A nanoporous capillary, for example, could separate molecules by their size and shape or be used to produce a controllable leak in the sample introduction system of a mass spectrometer.

Unfortunately, this technique of microchannel fabrication still remains limited to fused silica. In this material, the nanostructures facilitate the etchant penetration into the material and ensure the highly differential etching of the modified regions. In BK7 glass, where the femtosecond laser irradiation cannot produce nanostructures, the differential etching between laser-modified and surrounding material is insufficient to fabricate long high-aspect-ratio microchannels. We also speculate that this trend is general, and only those materials where the regime of nanostucture formation is possible are suitable for the microchannel fabrication using the combination of femtosecond laser modification and selective chemical etching in hydrofluoric acid.

Final thoughts

Femtosecond lasers provide very high quality of micromachining in a wide range of materials. One particular domain where femtosecond lasers allow one to achieve unequaled results is bulk modification of glasses. The key factors which determine this unparalled performance are the ability to initiate nonlinear light absorption in a medium transparent at the laser wavelength and the energy deposition into this medium on a time scale essentially smaller than the characteristic electron-lattice relaxation time. During the study of the modification morphology in fused silica we have identified the regimes that provide smooth modification necessary to produce waveguides and nanograting-nanovoid modification required for the etching of high-quality microchannels. The next step will be the integration of the waveguiding structures and microchannels in a single block of glass to build a micro-total analysis system (μ-TAS). The integration process is quite demanding from the engineering point of view as it requires a sub-micrometer accuracy and repeatability from the micro-positioning unit which moves the sample under the femtosecond laser focus. To continue the work on prototyping a microfluidic chip within NRC's Genomics Health Care Initiative project on pathogen detection we have purchased a state-of-the-art 3-D stage meeting these strict requirements. The nanoporous modification mentioned in the Conclusion may form a foundation of new potential applications of the femtosecond processing of glasses. We are currently studying (article in preparation) the properties of these interesting structures.

We also continue exploratory work on the fundamental issues related to the interaction of femtosecond laser pulses with transparent materials. One of the most puzzling features of the material modification dynamics is the formation of nanogratings or disordered nanostructures inside the modified regions. Our very recent studies (article in preparation) demonstrate that the morphology of the modification produced with circularly polarized fs laser radiation strongly depends on the handedness of the polarization. Inside the modified regions we observe left-handed or right-handed nanovortices which are less than 0.5 μm in diameter depending on the state of the circular polarization. Once again, only ultra-high spatial resolution diagnostics can be used to reveal and characterize such tiny objects. These experimental discoveries demonstrate that the physical processes involved in the nonlinear interaction of femtosecond light and matter are very far from being finalized and the studies in this interesting field will continue.

Appendix A

Calculations of the spreading of femtosecond laser pulses in space and time due to spherical aberration caused by focusing through a planar dielectric interface between refractive index-mismatched media: Geometric optics approximation.

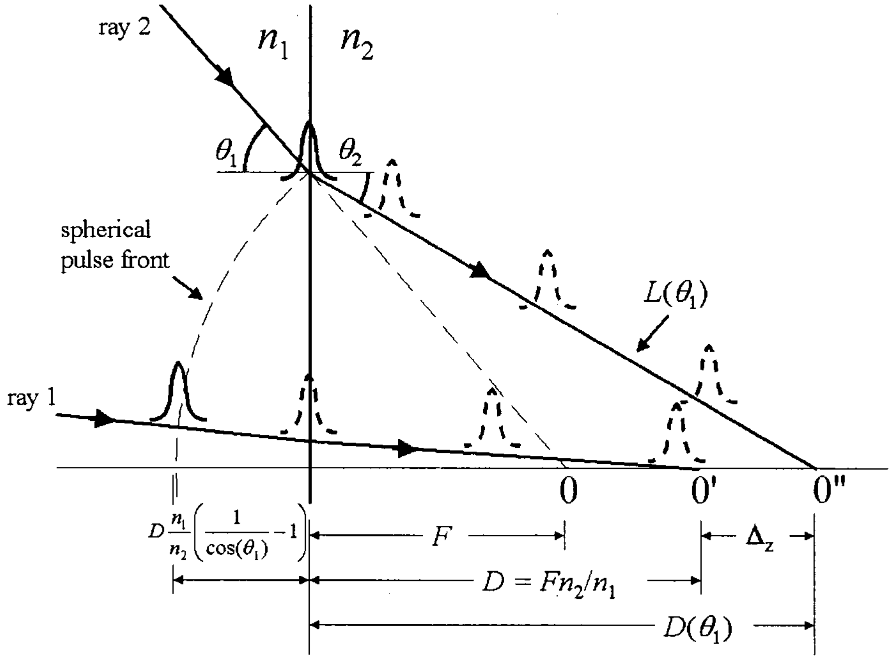

Fig. A. Refraction of a spherical pulse front at a planar dielectric interface between two media with the refractive indices n_1 and n_2. Rays 1 and 2 represent paraxial and marginal rays, respectively. O" denotes the position of the marginal focus. F, D, O, and O' are defined in the text and Fig. 2 of Section 0.1.

The derivation of formulae (17) and (18) is based on the assumption that the focusing objective is i) corrected for spherical and chromatic aberration and ii) that upon the refraction at the interface the pulse front remains parallel to the phase front. The first assumption leads to the coinciding, perfectly spherical pulse and phase fronts propagating in the first medium with n_1 after the focusing objective. The latter assumption can be justified by estimating the magnitude of the angle, α, between the normal vectors to the refracted pulse and phase fronts which initially coincide. In Ref. [20] it is shown that for an air-glass interface α is given by

$$\tan(\alpha) = \left(\frac{-\lambda\, dn/d\lambda}{n - \lambda\, dn/d\lambda} \right) \frac{\sin(\theta_1)}{\sqrt{n^2 - \sin^2(\theta_1)}}, \tag{A1}$$

where n is refractive index of the second medium. For an air-fused silica interface (n = 1.453, $dn/d\lambda = -1.7 \times 10^{-2}$ [μm^{-1}] at $\lambda = 0.8$ μm [20]) and θ_1 = arcsin(NA) = arcsin(0.75) (i.e., the maximum angle) formula (A1) yields $\tan(\alpha) \approx \alpha \approx 0.32°$, which can be neglected in comparison with the angle of refraction for the phase front ($\theta_2 \approx 30°$) given by Snell's law.*

I) Formula (17) is derived from Snell's law, which reads $n_1\sin(\theta_1) = n_2\sin(\theta_2)$, and a simple geometry presented in the Figure:

$$D(\theta_1) = F\frac{\tan(\theta_1)}{\tan(\theta_2)} = F\frac{\sin(\theta_1)/\cos(\theta_1)}{\sin(\theta_2)/\cos(\theta_2)} = F\frac{n_2\cos(\theta_2)}{n_1\cos(\theta_1)} = F\frac{n_2}{n_1}\sqrt{\frac{1-[\sin(\theta_1)n_1/n_2]^2}{1-\sin^2(\theta_1)}} \tag{A2}$$

By noting that the position of the paraxial focus is given by $D \approx (n_2/n_1)F$ and the magnitude of the longitudinal spreading caused by spherical aberration is defined as $\Delta_z = D(\theta_{1\max})-D$ one can easily obtain (17):

$$\Delta_z = D(\theta_{1\max}) - D = D\left\{\sqrt{\frac{1-[\sin(\theta_{1\max})n_1/n_2]^2}{1-\sin^2(\theta_{1\max})}} - 1\right\} \tag{A3}$$

II) One can derive (18) by considering the difference in the pulse propagation times along the marginal and paraxial rays shown in Fig. A. From Fig. A and (A2) it is seen that the path along the marginal ray 2, $L(\theta_1)$, is

$$L(\theta_1) = D(\theta_1)/\cos(\theta_2) = D/\cos(\theta_1) \tag{A4}$$

and the corresponding propagation time $T(\theta_1)$ is

$$T(\theta_1) = L(\theta_1)/v_g \approx L(\theta_1)/v_p = L(\theta_1)n_2/c = \frac{Dn_2}{c}\frac{1}{\cos(\theta_1)}, \tag{A5}$$

if, in order to simplify the derivation, the phase velocity $v_p = c/n_2$ is used instead of the group velocity $v_g = c/(n_2 - \lambda dn/d\lambda)$. For a pulse propagating along a paraxial ray the propagation time from the initial position on the spherical pulse front to the paraxial focus O' is given by

$$T_0 \approx \frac{D\frac{n_1}{n_2}\left[\frac{1}{\cos(\theta_1)} - 1\right]}{\frac{c}{n_1}} + \frac{D}{\frac{c}{n_2}} = \frac{D}{c}\left\{\frac{n_1^2}{n_2}\left[\frac{1}{\cos(\theta_1)} - 1\right] + n_2\right\} \tag{A6}$$

---

[*] The angle of refraction for the pulse front is $\theta_2-\alpha$.

At λ = 800 nm the difference between the phase and the group velocity is small (for most glasses including fused silica $|\lambda dn/d\lambda| < 0.05$) and this approximation gives an error less than 5% [20].** The delay between the pulse arrival at the marginal and paraxial foci can be obtained by subtracting (A6) from (A5):

$$\Delta T = T(\theta_{1\max}) - T_0 = \frac{D}{c}\frac{n_2^2 - n_1^2}{n_2}\left[\frac{1}{\cos(\theta_{1\max})} - 1\right], \qquad \text{(A7)}$$

which gives expression (18).

** In the near ultraviolet (NUV) spectral region, however, the dispersion is much stronger (e.g., at λ = 248 nm for SiO_2 the term $\lambda dn/d\lambda \approx -0.58$) and the group velocity should be used in expressions (A5) and (A6). In the NUV, the angle between the pulse and wavefront also becomes significant, which results in a smaller cone of angles produced in the second medium.

Ultra-high resolution index of refraction profiles of femtosecond laser modified silica structures

R. S. Taylor, C. Hnatovsky and E. Simova,

Institute for Microstructural Sciences, National Research Council
Montreal Road, Build. M-23A, Ottawa, ON, K1A 0R6, Canada
rod.taylor@nrc.ca; cyril.hnatovsky@nrc.ca; eli.simova@nrc.ca

D. M. Rayner, M. Mehandale, V. R. Bhardwaj and P. B. Corkum

Steacie Institute for Molecular Sciences, National Research Council
100 Sussex Dr., Ottawa, ON, K1A 0R6, Canada
david.rayner@nrc.ca; ravi.bhardwaj@nrc.ca; paul.corkum@nrc.ca

Abstract: The combination of selective chemical etching and atomic force microscopy has been used for the first time to make ultra-high spatial resolution (20 nm) index of refraction profiles of femtosecond laser modified structures in silica glass.

OCIS codes: (320.7110) Ultrafast nonlinear optics; (140.3330) Laser damage; (140.3440) Laser-induced breakdown;

References

1. Q. Zhong and D. Inniss, "Characterization of the lightguiding structure of optical fiber by atomic force microscopy," J. Lightwave Technol. **12**, 1517-1523 (1994).
2. K. Raine, J. Baines and D. Putland, "Refractive index profiling – state of the art," J. Lightwave Technol. **7**, 1162-1169 (1989).
3. N. Gisin and B. Perny, "Optical fiber characterization by simultaneous measurement of the transmitted and refracted near field," J. Lightwave Technol. **11**, 1875-1883 (1993).
4. R. Taylor and C. Hnatovsky, "High resolution index of refraction profiling of optical waveguides," Proc. SPIE **4833**, 811-819 (2003).
5. J. Kang and C. Musgrave, "The mechanism of HF/H_2O chemical etching of SiO_2," J. Chem. Phys. **116**, 275-280 (2002).
6. S. Huntington, P. Mulvaney, A. Roberts, K. Nugent and M. Bazylenko, "Field characterization of a D-shaped optical fiber using scanning near-field optical microscopy," J. Appl. Phys. **82**, 510-512 (1997).
7. K. Chen, P. Herman, R. Taylor and C. Hnatovsky, "Photosensitivity and application with 157 nm F_2 laser radiation in planar lightwave circuits," J. Lightwave Technol. **21**, 140-148 (2003).
8. A. Streltsov and N. Borrelli, "Study of femtosecond-laser-written waveguides in glasses," J. Opt. Soc. Am. B **19**, 2496-2504 (2002).
9. H.Wang, "Multiple refractive index profiling of optical fibers using the reflection and refracted near-fields methods," Optik **102**, 36-40 (1996).
10. M. Ikeda, M. Tateda and H.Yoshikiyo, "Refractive index profile of a graded index fiber: measurement by a reflection method," Appl. Opt. **14**, 814-815 (1975).
11. R. Taylor, C. Hnatovsky, E. Simova, D. Rayner, R. Bhardwaj and P. Corkum, "Femtosecond laser fabrication of nanostructures in silica glass," accepted to Opt. Lett., 2003.
12. L. Sudrie, M.Franco, B. Prade and A. Mysyrowicz, "Study of damage in fused silica induced by ultra-short IR laser pulses," Opt. Commun. **191**, 333-339 (2001).
13. C. Schaffer, J. Aus der Au, E. Mazur and J. Squier, "Micromachining and material change characterization using femtosecond laser oscillators," Proc. SPIE, **4633**, 112-118 (2002).
14. T. Gorelik, M. Will, S.Nolte, A. Tuennermann and U. Glatzel, "Transmission electron microscopy studies of femtosecond laser induced modifications in quartz," Appl. Phys. A **76**, 309-311 (2003).
15. O. L. Bourne, D. M Rayner, P. B. Corkum, M. Mehendale, and A. Naumov, "Methods for creating optical structures in dielectrics using controlled energy deposition," *International Application Published Under the Patent Cooperation Treaty (PCT) WO 02/16070 A2*, 2002.

#2207 - $15.00 US Received March 05, 2003; Revised March 24, 2003

16. R. Taylor and K. Leopold, "Probe microscopy for photonic applications," Microscopy and Analysis, May, 15-17 (1999).
17. J. Chan, T. Huser, S. Risbud and D. Krol, "Structural changes in fused silica after exposure to focused femtosecond laser pulses," Opt.Lett. **26**, 1726-1728 (2001).
18. R. Devine, R. Dupree, I. Farnan and J. Capponi, "Pressure-induced bond-angle variation in amorphous SiO_2," Phys. Rev. B **35**, 2560-2562 (1987).
19. A.Gusarov and D. Boyle, "Contribution of photoinduced densification to refractive-index modulation in Bragg gratings written in Ge-doped silica fibers," Opt.Lett. **25**, 872-874 (2000).
20. A. Marcinkevicius, S. Juodkazis, M. Watanabe, M. Miwa, S. Matsuo and H. Misawa, "Femtosecond laser-assisted three-dimensional microfabrication in silica," Opt. Lett. **26**, 277-279 (2001).

---

1. Introduction

In 1994 Zhong and Inniss discovered that weak chemical etching in hydrofluoric acid (HF) of a cleaved germanosilicate fiber, followed by atomic force microscopy (AFM) to measure the resulting topography, could be used to deduce the fiber's index of refraction profile [1]. The index profile could be measured with a spatial resolution of 20 nm, some 20 to 30 times better than what could be achieved with conventional optical indexing techniques [2, 3] that are restricted by the diffraction limit of light. It is possible to improve the spatial resolution to beyond the diffraction limit of light using reflection Near-Field Scanning Optical Microscopy (R-NSOM). However, R-NSOM experiments are difficult to perform and it is not straightforward to transform the reflection data into meaningful index data [4]. The AFM etch technique successfully mapped out the refractive index profile, because it was shown experimentally that i) for Ge doped fibers the core etches faster than the cladding and ii) the differential etch rate of the core versus the cladding in HF was linearly dependent on the core dopant concentration [1]. Since the index of refraction of the core was also linearly dependent on the dopant concentration, the inverted etch profile represented the index of refraction profile of the fiber. It should be noted that the etch depth cannot be used to give the absolute value for the index change, Δn, but it can provide a relative measure, allowing one to compare index changes of germanosilicate fibers with different dopant concentrations. The linear relationship between etch rate and dopant concentration was not obvious since the chemistry of etching pure silica never mind doped silica is very complicated [5]. The high spatial resolution of the technique has proved useful over the years for obtaining accurate index profiles of small core GeO_2 doped fibers [6].

There is presently a need for such high spatial resolution index profiling to map out induced index changes in dielectrics such as glass produced, for example, by VUV (157 nm) laser radiation [7] as well as produced by high intensity femtosecond laser (800 nm) radiation [8]. However, there is no a priori reason to expect that the AFM/etch technique can be applied to these cases. In fact, the formation mechanisms responsible for both these laser induced index changes are not well known [7, 8] and they clearly differ from the doped fiber case mentioned above. In reference [7], we used high resolution (400 nm) microreflectivity measurements of the type described in [9, 10] to confirm the validity of using the AFM technique to map out a very narrow (1/e width = 800 nm) region of VUV induced index change at the core cladding interface of hydrogen loaded Corning SMF-28 telecom fibers.

In this paper, we show that the combined use of selective chemical etching and AFM can also be used to predict the index profiles produced when Ti:Sapphire femtosecond laser radiation at a wavelength of 800 nm is focussed into a block of silica to form waveguide structures. The modification process is highly non-linear and some of the induced index changes have feature sizes as small as 50 nm, which cannot be measured with standard optically based index profiling techniques. Detailed knowledge of these fine structures has very recently allowed us to fabricate sub-micron holes and channels in silica [11]. In other research on femtosecond laser modification of dielectrics scanning electron microscopy [12], third harmonic generation microscopy [13] and transmission electron microscopy [14] have been used to image the modified structures with sub-micron resolution. However, none of these techniques are able to measure the index of refraction profile which is key to assessing the potential of a modified structure for waveguide applications. We also show in this paper that the AFM/etch technique is particularly well suited to measuring index profiles of arrays of waveguides.

2. Experimental

A regeneratively amplified Ti:Sapphire laser operating at λ=800 nm over a repetition rate range of 10-250 kHz and with a maximum average power of 270 mW measured after a spatial filter was used in the experiments. The laser pulse duration was nominally 40 fs. A 40x, NA=0.65 microscope objective was used to focus the laser radiation transverse to a polished block of high grade fused silica at a depth of approximately 100 μm. Waveguides were written by translating the sample with scan rates in the range of 10-200 μm/s.

The use of the NA=0.65 microscope objective results in a focal volume that is significantly stretched in the direction of light propagation. We have found that the insertion of a long focal length (40 cm) cylindrical lens before the objective to produce a line focus at an angle to the sample scan direction can be used to decrease the ellipticity of the focal volume [15]. Waveguides with more circular cross-sections were produced in this way for index profiling analysis. We also used reflective optics to write waveguide structures longitudinally (i.e., sample translation is in the direction of the laser beam). Here the laser beam was brought through the work-piece and reflected back into it using a 50 mm focal length mirror with an effective aperture of 8 mm.

After laser writing the waveguides the silica block was cut into two pieces perpendicular to the scan direction and the two inside surfaces were polished for index profiling analysis using a standard pitch polishing technique. The two inside surfaces were chosen for analysis to eliminate the problem of laser damage, which often occurred on the outside surface. Furthermore, focussing light transversely through the edge of a block results in distortions within a few microns of the natural ends of the waveguide. We have verified that the uniformity of the waveguides down the length of the block of silica was excellent so that the same index profile could be obtained independent of exactly where the block was cut and polished.

To validate the AFM/etching technique and to obtain the absolute value Δn, microreflectivity was performed on one of the two non etched polished inside surfaces. The sample was glued onto a probe holder at the base of a scanning probe microscopy (SPM) head of a Digital Instruments Dimension 3000 AFM. The AFM has been modified to permit a tethered mode of operation allowing the SPM head to be decoupled from its vertical position in the main microscope body and deployed horizontally to scan the sample [16]. A 50x, NA=0.8 microscope objective focussed unpolarized He-Ne light (633nm) to a near-diffraction limited spot on the sample. Light reflected from this surface returned through the lens and was directed by a cube beamsplitter onto a Newport model 1830-C powermeter for detection. Blockage of the laser beam before the lens provided a reference signal to estimate the core/cladding index difference using the Fresnel equations for an air/glass reflection [10]. Blocking the light after the lens verified that backreflection and backscattering from the lens was negligible. The back surfaces of the waveguides were terminated with a bead of index matching epoxy to ensure that negligible back reflected light returned to the front surface. The microreflection technique could detect index changes as small as $1\mathrm{x}10^{-4}$ with a lateral spatial resolution of approximately 400 nm.

The second piece of silica block was used for the AFM/etch analysis. The AFM was operated in the contact mode with silicon nitride probes. Prior to etching we confirmed that polishing did not produce any significant topography ($\leq$ 1 nm) change over the waveguide region. Etching took place in a room temperature bath of 1% by volume hydrofluoric acid (HF) for typically 3 to 6 minutes. The sample was rinsed in distilled water then cleaned in isopropanol, dried and mounted and placed under the AFM. The etching generally produced a structure approximately 20–40 nm deep. The lateral resolution of the AFM image is determined by the sharpness of the probe tips, estimated to be between 15 nm and 20 nm. The vertical resolution is generally sub-nm although for very large image scans (≥40 μm) the vertical accuracy was a few nm.

3. Results

Figure 1 shows an inverted image of the AFM topography profile of an etched longitudinally written waveguide. It is the claim of this paper that the inverted AFM image represents the index of refraction profile. The waveguide is circular with a diameter of only 1.7 μm much less than the estimated diameter (8 μm) of the focussed laser beam waist. Similar observations have been made in references [12-14]. We have performed a preliminary theoretical analysis which suggests that at laser pulse energies of ≈ 40 nJ (peak power of ≈1MW) there is a sudden onset of a six photon absorption process (based upon the femtosecond laser photon energy of 1.4 eV and an ≈ 8 eV band-gap for silica) which compensates for self-focussing to prevent catastrophic collapse of the modified zone resulting in the uniform circular structure shown in Fig. 1.

Figure 1 demonstrates the importance of using an ultra-high resolution index profiling technique. The AFM image shows that there is a very sharp (100 nm) transition to the induced index change again indicative of highly non-linear processes being responsible for the material modification. There is also an immediate transition to a flat-topped index profile suggesting saturation in the magnitude of the induced index change. A section analysis through the center of the inverted AFM image is shown in Fig. 2. Normalized index data obtained from microreflectivity measurements on the sample before etching are also shown for comparison. Considering the poorer resolution of the microreflectivity technique (400 nm) the agreement between the two index profiles shown in Fig. 2 is good providing validation for the AFM etch technique.

Fig. 1. Inverted cross-sectional AFM image of a chemically etched longitudinally written waveguide. The laser was operated at a repetition rate of 250 kHz and an average power of 175 mW. The scan rate was 100 μm/s. The width of the flat-topped region is ≈ 1.7 μm.

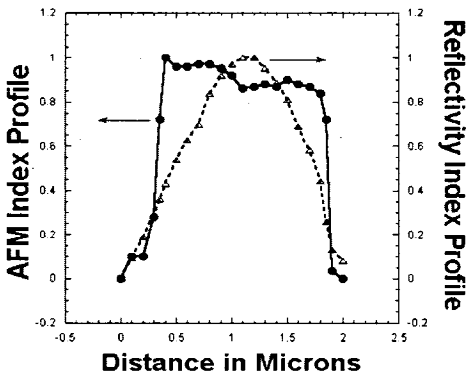

Fig. 2. Index of refraction profiles (arbitrary units) across the longitudinally written waveguide shown in Fig.1 and obtained using the chemical etching/AFM and microreflectivity techniques.

We have verified for a number of different experimental conditions that the etch depth (1% HF) for both longitudinally and transversely written waveguides depends linearly on etch time at least up to etch depths of 100 nm. We have also observed that the shape of the etched profile is invariant with etch time showing no change for a five times increase in etch duration. There is an optimum etch time for a given etch concentration. If the etch time is too short then a shallow trench is formed which results in a poorer signal to noise ratio on the AFM image. If the etch time is too long then deep (>100 nm) trenches are formed. In this case the AFM probe tip does not accurately track the topography of such narrow deep trenches. An etch depth range of 20-60 nm gives the most reliable results.

In Fig. 3, the average etch depth across a waveguide is plotted as a function of induced index of refraction obtained from microreflectivity measurements for five waveguides that were written in the same block of silica using the aspherical lens (microscope objective plus cylindrical lens). Measurements were made for three different angles (6°, 10° and 15°) between the line focus produced with the cylindrical lens and the sample scan direction and at

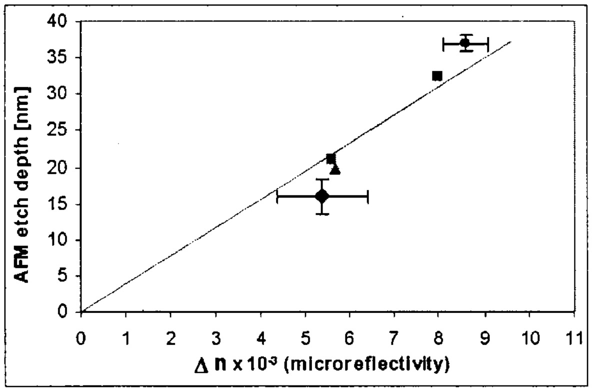

Fig. 3. Average AFM etch depth (1%HF,6 minutes) as a function of induced index change measured using microreflectivity averaged across the width of five waveguides written with an aspherical lens using a femtosecond laser power of 250mW and under the following conditions: (◆) 15°, 100µm/s, (■) 15°,50µm/s, (▲) 10°,100µm/s, (■) 10°, 50 µm/s and (●) 6°, 50µm/s. The line shown in the figure is the best line visually through the data and the origin. The error bars indicate the experimental uncertainty on the AFM and microreflectivity data, which is higher for the lower index changes.

two different scan rates (50 µm/s and 100 µm/s). The laser power was 250 mW before the lens combination for each waveguide. The lower scan rate results in a times two higher dosage of laser energy per micron of scan travel leading to a higher index change. The higher values for the induced index of refraction with the lower laser writing angles is the result of narrower but more highly modified waveguide structures. Figure 3 clearly demonstrates that the etch depth for a fixed HF etch concentration and etch time scales approximately linearly with the induced index of refraction change. Consequently the inverted topographic profiles of the weakly etched waveguides represent the induced index of refraction profiles produced by the femtosecond laser pulses.

The potential of the AFM/etch technique for high resolution index mapping is demonstrated in Fig.4, which shows an inverted AFM image of a chemically etched transversely written (lens NA=0.65) conical tapered structure. The structure is highly tapered in the direction of the focussed light from ≈ 1 µm to a very sharp tip of only ≈ 100 nm width. The high resolution (20 nm) of the AFM/etch technique revealed for the first time the sharpness of the tip region (100 nm); the steepness (150 nm) of the transition from the unmodified to a flat-topped modified region and the uniformity of the index change throughout the conical structure. This information led to the fabrication of sub-micron holes and channels in silica [11]. Microreflectivity data supports the AFM /etch data. Similar shaped conical tapered structures were observed in the microreflectivity images.

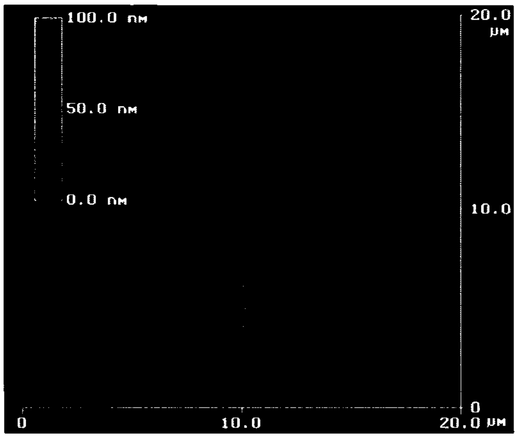

Fig. 4. Inverted AFM image of the cross-section of an etched tapered conical structure in a silica glass sample. The etch depth (before inversion) was ≈ 40 nm over the entire conical structure. The structure was produced by focussing (NA=0.65) a 30 mW, 100 kHz laser beam ≈ 150 µm below the top surface and translating the sample perpendicular to the laser beam at a scan rate of 25 µm/s. The sample was then cut in two pieces transverse to the scan direction. One of the inside surfaces was polished then etched (1% HF for 3 min) and placed under the AFM. The focussed femtosecond laser light entered from the top of the image.

We have performed numerous microreflectivity experiments to measure the index of refraction profiles of femtosecond laser written waveguides in amorphous silica. The data consistently confirmed the index profiles predicted by the AFM/etching technique. Furthermore, the results of Fig. 3 how that the etch depths (for a given concentration of acid and etch time) of the modified regions created with different laser parameters provide a relative measure of the magnitude of the index changes. The AFM technique is very straightforward to use and since all the waveguides written into a block of silica are etched simultaneously it is possible to obtain index data on tens of waveguides in a few hours. The technique is simpler to perform and is less sensitive to sample surface quality (i.e., dust, scratches) than microreflectivity. The technique is essentially non-invasive since etching produces topography changes of less than 100 nm, which shouldn't effect the ability to couple light out of the waveguide.

4. Discussion

In this paper, we show that the etch rate of femtosecond laser modified silica structures is approximately linearly dependent on the induced index of refraction change at least up to index changes of ≈ 0.01. The linear relationship between etch depth and index may only apply to fused-silica and could be completely different for multi-component glasses.

The mechanism, which accounts for the formation of positive index regions in silica glass using focussed femtosecond laser radiation is not completely clear [8]. The dimensions of some of the highly tapered modified regions such as shown in Fig. 4 are much smaller than what would be predicted from just multiphoton absorption. The etched structures reveal a complex response of the material that develops over a number of laser shots. It is believed that near the power threshold for material modification changes occur in the silica bond structure affecting how the bonds pack together. For example, there appears to be an increase in the number of 3 and 4 member silica ring structures at the expense of 5 or 7 member rings [17]. The reordering into smaller ring member structures reduces the bridging bond angle [17,18]. This process is often referred to as "densification" and is believed to be the primary mechanism for UV writing of strong Bragg gratings in Ge-doped silica fibers [19].

If the modified structure corresponds to a region of densification then there should also be a surrounding region of lower density. This region might correspond to the much larger focal volume prior to the non-linear collapse to form the modified structure. We have used both microreflectivity and the AFM/etch technique to search for the low density region. In the case of the AFM technique we highly over-etched the modified structure to produce ≈ 2 μm deep holes hoping to pick-up a weak topography transition at larger dimensions between the non-irradiated silica and a lower density region. To date we have had no success finding such a low density region.

Marcinkevicius et. al. have suggested that the decrease in bridging bond angle in densified silica increases the reactivity of the oxygen atoms due to the deformed configuration of their valence electrons [20]. The increase in reactivity results in greater etching in the modified zones with respect to the unmodified zones. It is also possible that there is an increase in the number of non-bridging oxygen atoms due to bond breaking which can enhance the chemical activity.

More research is required to understand the relationship between the etching activity, densification, index of refraction and the decrease in the bridging bond angle.

5. Conclusions

In this paper, we have shown that selective chemical etching and atomic force microscopy can be used to measure the index of refraction profiles of femtosecond laser induced structures in silica glass. The technique is simple to use and provides ultra-high spatial resolution (20 nm). The high resolution has been used to reveal new information on the shape and size of the index modifications.

Bibliography

[1] A. P. Joglekar, H. Liu, E. Meyhöfer, G. Mourou, and A. J. Hunt. Optics at critical intensity: Applications to nanomorphing. *Proceedings of the National Academy of Science* (*PNAS*), **101**, 5856 (2004).

[2] K. M. Davis, K. Miura, N. Sugimoto, and K. Hirao. Writing waveguides in glass with a femtosecond laser. *Opt. Lett.* **21**, 1729 (1996).

[3] A. M. Streltsov and N. F. Borrelli. Fabrication and analysis of a directional coupler written in glass by nanojoule femtosecond laser pulses. *Opt. Lett.* **26**, 42 (2001).

[4] E. N. Glezer, M. Miloslavljevic, L. Huang, R. J. Finlay, T.-H. Her, J. P. Callan, and E. Mazur. Three-dimensional optical storage inside transparent materials. *Opt. Lett.* **21**, 2023 (1996).

[5] K. Hirao and K. Miura. Writing waveguides and gratings in silica and related materials by a femtosecond laser. *J. Non-Cryst. Solids* **239**, 91 (1998).

[6] S. J. Mihailov, C. W. Smelser, P. Lu, R. B. Walker, D. Grobnic, H. Ding, and G. Henderson. Fiber Bragg gratings made with a phase mask and 800-nm femtosecond radiation. *Opt. Lett.* **28**, 995 (2003).

[7] R. Osellame, S. Taccheo, G. Cerullo, M. Marangoni, D. Polli, R. Ramponi, P. Laporta, and S. De Silvestri. Optical gain in Er-Yb doped waveguides fabricated by femtosecond laser pulses. *Electron. Lett.* **38**, 964 (2002).

[8] K. Kawamura and M. Hirano; D. Tokamizu, T. Kamiya, and H. Hosono. Femtosecond-laser-encoded distributed-feedback color center laser in lithium fluoride single crystals. *Appl. Phys. Lett.* **84**, 311 (2004).

[9] M. S. Giridhar, K. Seong, A. Schülzgen, P. Khulbe, N. Peyghambarian, and M. Mansuripur. Femtosecond pulsed laser micromachining of glass substrates with application to microfluidic devices. *Appl. Opt.* **43**, 4584 (2004).

[10] L. Shah, J. Tawny, M. Richardson, and K. Richardson. Femtosecond laser deep hole drilling of silicate glasses in air. *Appl. Surf. Sci.* **183**, 151 (2001).

[11] Y. Li; K. Itoh, W. Watanabe, K. Yamada, and D. Kuroda; J. Nishii; Y. Jiang. Three-dimensional hole drilling of silica glass from the rear surface with femtosecond laser pulses. *Opt. Lett.* **26**, 1912 (2001).

[12] K. Sugioka, M. Masuda, T. Hongo, Y. Cheng, K. Shihoyama, and K. Midorikawa. Three-dimensional microfluidic structure embedded in photostructurable glass by femtosecond laser for lab-on-chip applications. *Appl. Phys. A* **79**, 815 (2004).

[13] Marcinkevičius and S. Juodkazis; M. Watanabe, M. Miwa, Sh. Matsuo, and H. Misawa; J. Nishii. Femtosecond laser-assisted three-dimensional microfabrication in silica. *Opt. Lett.* **26**, 277-279 (2001).

[14] A. Manz, H. Becker (eds.): *Microsystem Technology in Chemistry and Life Sciences* (Springer, New York 1998).

[15] L. Sudrie, M. Franco, B. Prade, and A. Mysyrowicz. Study of damage in fused silica induced by ultra-short IR laser pulses. *Opt. Commun.* **191**, 333 (2001).

[16] J. W. Chan, T. Huser, S. Risbud, and D. M. Krol. Structural changes in fused silica after exposure to focused femtosecond laser pulses. *Opt. Lett.* **26**, 1726 (2001).

[17] E. N. Glezer and E. Mazur. Ultrafast-laser driven micro-explosions in transparent materials. *Appl. Phys. Lett.* **71**, 882 (1997).

[18] D. von der Linde, K. Sokolowski-Tinten, J. Bialkowski. Laser-solid interaction in the femtosecond time regime. *Appl. Surf. Sci.* **109/110**, 1 (1997).

[19] R. L. Sutherland. *Handbook of nonlinear optics*. (Marcel Dekker. New York. 2003).

[20] J. –C. Diels and W. Rudolph. *Ultrashort laser pulse phenomena.* (Academic Press. San Diego. 1996).

[21] S. A. Diddams, H. K. Eaton, A. A. Zozulya, and T. S. Clement. Characterizing the nonlinear propagation of femtosecond pulses in bulk media. *IEEE J. Quantum Electron.* **4**, 306 (1998).

[22] R. W. Boyd. *Nonlinear optics*. (Academic Press. San Diego. 1992).

[23] R. R. Alfano, ed. *The supercontinuum laser source*. (Springer. New York. 1989).

[24] G. Fibich and B. Ilan. Vectorial and random effects in self-focusing and in multiple filamentation. *Phys. D* **157**, 112 (2001).

[25] J. H. Marburger. Self-focusing theory. *Prog. Quant. Electron.* **4**, 35 (1975).

[26] A. Brodeur and S. L. Chin. Ultrafast white-light continuum generation and self-focusing in transparent condensed media. *J. Opt. Soc. Am. B* **16**, 637 (1999).

[27] M. J. Soileau, W. F. Williams, N. Mansour, and E. W. Van Stryland. Laser-induced damage and the role of self-focusing. *Opt. Eng.* **28**, 1133 (1989).

[28] J. B. Ashcom. *The role of focusing in the interaction of femtosecond laser pulses with transparent material.* Ph.D. thesis. Harvard university (2003).

[29] N. Bloembergen. *IEEE J. Quantum Electron.* **10**, 375 (1974).

[30] M. Born and E. Wolf. *Principles of optics.* (Pergamon Press. Oxford. 1980).

[31] V. N. Mahajan. Uniform versus Gaussian beams: a comparison of the effects of diffraction, obscuration, and aberrations. *J. Opt. Soc. Am. A* **3**, 470 (1986).

[32] H. Urey. Spot size, depth-of-focus, and diffraction ring intensity formulas for truncated Gaussian beams. *Appl. Opt.* **43**, 620 (2004).

[33] A. E. Siegman. *Lasers.* (University Science Books. Mill Valley. 1986).

[34] C. B. Schaffer, A. Brodeur and E. Mazur. Laser-induced breakdown and damage in bulk transparent materials induced by tightly focused femtosecond laser pulses. *Meas. Sci. Technol.* **12**, 1784 (2001).

[35] G. G. Luther, J. V. Moloney, and A. C. Newell; E. M. Wright. Self-focusing threshold in normally dispersive media. *Opt. Lett.* **19**, 862 (1994).

[36] I. P. Kaminow; B. G. Bagley; C. G. Olson. Measurement of the absorption edge in fused silica. *Appl. Phys. Lett.* **32**, 98 (1978).

[37] K. Saito and A. J. Ikushima. Absorption edge in silica glass. *Phys. Rev. B* **62**, 8584 (2000).

[38] R. P. Gupta. Electronic structure of crystalline and amorphous silicon dioxide. *Phys. Rev. B* **32**, 8278 (1985).

[39] J. Zhang, K. Sugioka, S. Wada, H. Tashiro, K. Toyoda, and Sh. Ruschin. Origin of high-speed modification of refractive index in fused quartz by vacuum ultraviolet laser irradiation. *IEEE J. Sel. Top. Quant. Electron.* **3**, 789 (1997).

[40] H. Misawa, H. –B. Sun, S. Juodkazis, M. Wtanabe, S. Matsuo. Microfabrication by femtosecond laser irradiation. *Proc. SPIE* **3933**, 246 (2000).

[41] N. B. Delone and V. P. Krainov. *Atoms in strong light fields.* (Springer-Verlag. Berlin. 1985).

[42] L. V. Keldysh. *Zh. Eksp. Teor. Fiz.* **47** 1945 (1964) [*Sov. Phys. JETP* **20**, 1307 (1965)].

[43] N. B. Delone. *Basics of interaction of laser radiation with matter.* (Editions Frontières. Gif-sur-Yvette Cedex. 1993).

[44] B. C. Stuart, M. D. Feit, S. Herman, A. M. Rubenchik, B. W. Shore, and M. D. Perry. Nanosecond-to-femtosecond laser-induced breakdown in dielectrics. *Phys. Rev. B* **53**, 1749 (1996).

[45] K. K. Thornber. Applications of scaling to problems in high-field electronic transport. *J. Appl. Phys.* **52**, 279 (1981).

[46] A.-C. Tien, S. Backus, H. Kapteyn, M. Murnane, and G. Mourou. Short-pulse laser damage in transparent materials as a function of pulse duration. *Phys. Rev. Lett.* **82**, 3883 (1999).

[47] L. Sudrie, A. Couairon, M. Franco, B. Lamouroux, B. Prade, S. Tzotzakis, and Mysyrowicz. Femtosecond laser-induced damage and filamentary propagation in fused silica. *Phys. Rev. Lett.* **89**, 186601 (2002).

[48] L. N. Gaier, M. Lein, M. I. Stockman, P. L. Knight, P. B. Corkum, M. Yu. Ivanov, and G. L. Yudin. Ultrafast multiphoton forest fires and fractals in clusters and dielectrics. *J. Phys. B: At. Mol. Phys.* **37**. L57 (2004).

[49] G. L. Yudin, L. N. Gaier, M. Lein, P. L. Knight, P. B. Corkum, and M. Yu. Ivanov. Hole-assisted energy deposition in clusters and dielectrics in multiphoton regime. *Laser Phys.* **14**, 51 (2004).

[50] A. L. Gaeta. Catastrophic collapse of ultrashort pulses. *Phys. Rev. Lett.* **84**, 3582 (2000).

[51] D. M. Rayner, A. Naumov and P. B. Corkum. Ultrashort pulse non-linear optical absorption in transparent media. *Opt. Express* **13**, 3208 (2005).

[52] S. S. Mao, F. Quéré, S. Guizard, X. Mao, R. E. Russo, G. Petite, P. martin. Dynamics of femtosecond laser interactions with dielectrics. *Appl. Phys. A* **79**, 1695 (2004).

[53] M. Bass ed. Handbook of optics. Volume II. Devices measurements and properties. (McGraw-Hill. New York. 1995).

[54] Z. Bor. Distortion of femtosecond laser pulses in lenses and lens systems. *J. Mod. Opt.* **35**, 1907 (1988).

[55] M. Kempe and W. Rudolph. Femtosecond pulses in the focal region of lenses. *Phys. Rev. A* **48**, 4721 (1993).

[56] M. Kempe and W. Rudolph. Impact of chromatic and spherical aberration on the focusing of ultrashort light pulses by lenses. *Opt. Lett.* **18**, 137 (1993).

[57] P. Török, P. Varga, Z. Laczik, and G. R. Booker. Electromagnetic diffraction of light focused through a planar interface between materials of mismatched refractive indices: an integral representation. *J. Opt. Soc. Am. A* **12**, 325 (1995).

[58] P. Török and P. Varga. Electromagnetic diffraction of light focused through a stratified medium. *Appl. Opt.* **36**, 2305 (1997).

[59] J. J. Stammes. *Waves in focal regions. Propagation, diffraction and focusing of light, sound and water waves*. (Adam Hilger. Bristol and Boston. 1986).

[60] S. H. Wiersma, P. Török, T.D. Visser, and P. Varga. Comparison of different theories for focusinf through a plane interface. *J. Opt. Soc. Am. A* **14**, 1482 (1997).

[61] K. M. Romallosa, J. Bantang, and C. Saloma. Three-dimensional distribution near the focus of a tightly focused beam of few-cycle optical pulses. *Phys. Rev. A* **68**, 033812 (2003).

[62] M. Gu, *Advanced Optical Imaging Theory* (Springer. Berlin. 2000).

[63] Q. Zhan and J. R. Leger. High-resolution imaging ellipsometer. *Appl. Opt.* **41**, 4443 (2002).

[64] A. Boivin and E. Wolf. Electromagnetic field in the neighborhood of the focus of a coherent beam. *Phys. Rev.* **138**, B1561 (1965).

[65] S. H. Wiersma, T. D. Visser and P. Török. Annular focusing through a dielectric interface: scanning and confining the intensity. *Pure Appl. Opt.* **7**, 1237 (1998).

[66] K. Yamada and W. Watanabe; J. Nishii; K. Itoh. Anisotropic refractive-index change in silica glass induced by self-trapped filament of linearly polarized femtosecond laser pulses. *J. Appl. Phys.* **93**, 1889 (2003).

[67] M. Kamata, M. Obara. Control of the refractive index change in fused silica glasses induced by a loosely focused femtosecond laser beam. *Appl. Phys. A* **78**, 85 (2004).

[68] Y. Shimotsuma, P. G. Kazansky, J. Qiu, and K. Hirao. Self-organized nanogratings in glass irradiated by ultrashort light pulses. *Phys. Rev. Lett.* **91**, 247405 (2003).

[69] J. D. Mills, P. G. Kazansky, and E. Bricchi; J. J. Baumberg. Embedded anisotropic microreflectors by femtosecond-laser micromachining. *Appl. Phys. Lett.* **81**, 196 (2002).

[70] J. W. Chan, T. R. Huser, S. H. Risbud, D. M. Krol. Modification of the fused silica glass network associated with waveguide fabrication using femtosecond laser pulses. *Appl. Phys. A* **76**, 367 (2003).

[71] A. Agarwal and M. Tomozawa. Correlation of silica glass properties with the infrared spectra. *J Non-Cryst. Solids* **209**, 166 (1997).

[72] C. Fiori and R. A. B. Devine. Evidence for a wide continuum of polymorphs in a-SiO_2. *Phys. Rev. B* **33**, 2972 (1986).

[73] K. Awazu and H. Kawazoe. Strained Si-O-Si bonds in amorphous SiO_2 materials: A family member of active centers in radio, photo, and chemical responses. *J. Appl. Phys.* **94**, 6243 (2003).

[74] H. –B. Sun and S. Juodkazis; M. Watanabe, S. Matsuo, and H. Misawa; J. Nishii. Generation and recombination of defects in vitreous silica induced by irradiation with a near-infrared femtosecond laser. *J. Phys. Chem. B* **104**, 3450 (2000).

[75] O. M. Efimov; K. Gabel; S. V. Garnov; L. B. Glebov, S. Grantham, M. Richardson, and M. J. Soileau. Color-center generation in silicate glasses exposed to infrared femtosecond pulses. *J. Opt. Soc. Am. B* **15**, 193 (1998).

[76] A. M. Streltsov and N. F. Borrelli. Study of femtosecond-laser-written waveguides in glasses. *J. Opt. Soc. Am. B* **19**, 2496 (2002).

[77] R. Schenker, P. Schermerhorn, W. G. Oldham. Deep-ultraviolet damage to fused silica. *J. Vac. Sci. Technol. B* **12**, 3275 (1994).

[78] E. Bricchi, W. Yang, and P. Kazansky. *Robustness of Femtosecond Direct Written Structures in Silica Glass.* Presented at the Conference on Lasers and Electro-Optics, Baltimore, MA, (USA), May 22-27, 2005.

[79] R. P. Pattathil, C. Hnatovsky, E. Simova, R. B. Vedula, R. S. Taylor, D. M. Rayner, P. B. Corkum. Femtosecond laser-induced nanostructures in fused silica. *Proc. SPIE* **5971**, 53 (2005).

[80] F. Y. Génin; A. Salleo and T. V. Pistor; L. L. Chase. Role of light intensification by cracks in optical breakdown on surfaces. *J. Opt. Soc. Am. A* **18**, 2607 (2001).

[81] R. S. Taylor, C. Hnatovsky, and E. Simova; D. M. Rayner, M. Mehandale, V. R. Bhardwaj, and P. B. Corkum. Ultra-high resolution index of refraction profiles of femtosecond laser modified silica structures. *Opt. Express* **11**, 775 (2003).

[82] R. S. Taylor and K. E. Leopold; M. Wendman, G. Gurley, and V. Elings. Scanning probe optical microscopy of evanescent fields. *Rev. Sci. Instrum.* **69**, 2981 (1998).

[83] P. Burgos, Z. Lu, A. Ianoul, C. Hnatovsky, M. –L. Viriot, L. J. Johnston, and R. S. Taylor. Near-field scanning optical microscopy probes: a comparison of pulled and double-etched bent NSOM probes for fluorescence imaging of biological samples. J. Microsc. **211**, 37 (2003).

[84] R. S. Taylor and K. E. Leopold. Combined AFM-NSOM scanning probe microscopy for photonic applications. *Microsc. Analysis* **13**, 15 (1999).

[85] Q. Zhong and D. Innis. Characterization of the lightguiding structure of optical fiber by atomic force microscopy. *J. Lightwave Technol.* **12**, 1517 (1994).

[86] K. W. Raine, J. G. N. Baines, and D. E. Putland. Refractive index profiling – state of the art. *J. Lightwave Technol.* **7**, 1162 (1994).

[87] M. Ikeda, M. Tateda, and H. Yoshikiyo. Refractive index profile of a graded index fiber: Measurement by a reflection method. *Appl. Opt.* **14**, 814 (1975).

[88] H. Wang. Multiple refractive index profiling of optical fibers using the reflection and refracted near-field methods. *Optik* **102**, 36 (1996).

[89] L. Novotny, R. D. Grober, K. Karrai. Reflected image of a strongly focused spot. *Opt. Lett.* **26**, 789 (2001).

[90] L. Holland. *The properties of glass surfaces*. (Chapmann and Hall. London. 1964).

[91] H. Fukuyo, N. Oura, N. Kitajima, and H. Kono. The refractive index distribution normal to the polished surface of fused quartz measured by ellipsometry. *J. Appl. Phys*. **50**, 3653 (1979).

[92] J. Stone and H. E. Earl. Surface effects and reflection refractometry of optical fibers. *Opt. Quant. Electron.* **8**, 459 (1976).

[93] R. E. Betzig. *Non-destructive optical imaging of surfaces with 500 Ångstrom resolution* (Volumes 1 and 2). Ph.D. thesis. Cornell university (1988).

[94] S. K. Rhodes, K. A. Nugent, and A. Roberts. Precision measurement of the electromagnetic fields in the focal region of a high-numerical-aperture lens using a tapered fiber probe. *J. Opt. Soc. Am. A* **19**, 1689 (2002).

[95] R. Juškaitis and T. Wilson. The measurement of the amplitude point spread function of microscope objective lenses. *J. Microsc.* **189**, 8 (1998).

[96] C. Debus, M. A. Lieb, A. Drechsler, and A. J. Meixner. Probing highly confined optical fields in the focal region of a high NA parabolic mirror with subwavelength spatial resolution. *J. Microsc.* **210**, 203 (2003).

[97] Y. Inouye and S. Kawata. Near-field scanning optical microscope with a metallic probe tip. *Opt. Lett.* **19**, 159 (1994).

[98] V. R. Bhardwaj, E. Simova, P. P. Rajeev, C. Hnatovsky, R. S. Taylor, D. M. Rayner, and P. B. Corkum. Optically produced arrays of nano-planes inside fused silica. Accepted for publication in *Phys. Rev. Lett.* (2005).

[99] Y. Shimotsuma and K. Hirao; J. Qiu; P. Kazansky. Nano-modification inside transparent materials by femtosecond laser single beam. *Mod. Phys. Lett.* **19**, 225 (2005).